UNIVERSITY OF CALIFORNIA, SAN DIEGO

A Method for Dynamic Earthquake Rupture Simulation with Applications to a Large Southern San Andreas Scenario

A dissertation submitted in partial satisfaction of the requirements
for the degree Doctor of Philosophy

in

Earth Sciences

by

Geoffrey Palarz Ely

Committee in charge:

Jean-Bernard H. Minster, Chair
Steven M. Day
Yuri A. Fialko
J. Freeman Gilbert
Reagan W. Moore
Larry L. Smarr

2008

The dissertation of Geoffrey Palarz Ely is approved, and it is acceptable in quality and form for publication on microfilm:

_____

_____

_____

_____

_____

_____

Chair

University of California, San Diego

2008

To Kim

TABLE OF CONTENTS

LIST OF FIGURES

LIST OF TABLES

ACKNOWLEDGMENTS

I am grateful to Professor Bernard Minster for his support as the chair of my Doctoral Committee. I have depended on Bernard for inspiration, motivation, and direction throughout my stay at Scripps Institution of Oceanography. I was always given the freedom to follow my own ideas, make my own mistakes, and make my own discoveries. My only job ever was to do good science. I was introduced to Bernard by Professor Steven Day, my advisor during my master's studies at San Diego State University. I came to UCSD to be able to continue working with Steve, and further pursue problems in earthquake rupture dynamics. He has given me careful guidance every step of the way, for which I am immensely thankful. I would also like to thank members of my committee: Professors Freeman Gilbert, Yuri Fialko, Larry Smarr, and Dr. Reagan Moore. The faculty and my fellow graduate students at the Institute for Geophysics and Planetary Physics have taught me a tremendous amount. I have also benefited greatly from my involvement with, and funding from the Southern California Earthquake Center, beginning with my days in its undergraduate intern program.

I could not have gotten this far without the support of my father Richard, my mother Margaret, my brother Benjamin and my sister Catia. Many good friends have made my time in San Diego unforgettable, and I would especially like to mention Ian, Mike and Sean. For the final leg of this journey, I have been blessed to have Kim as my companion and she makes my life better every day. Finally, to the bodyboarder who plucked me out of heavy surf under Scripps pier during an ill-advised swim: I never got your name, but I will always be thankful for your help.

Chapter 2, in full, is a reprint of *A support-operator method for viscoelastic wave modeling in 3D heterogeneous media* as it appears in Geophysical Journal International, volume 172, 2008. Chapter 3, in full, is under review by Geophysical Journal

International for an article titled *A Support-Operator Method for 3D Rupture Dynamics*. Chapter 4, in full, is under review by the Bulletin of the Seismological Society of America for an article titled *Dynamic Rupture Models for the Southern San Andreas Fault*. I am the primary investigator and author of each paper, with Steven Day and Jean-Bernard Minster as my co-authors.

VITA

1996	Bachelor of Science in Geophysics University of California, Santa Barbara
1997-2000	Research Assistant San Diego State University
2000	Master of Science in Geophysics San Diego State University
2000-2007	Research Assistant Scripps Institution of Oceanography University of California, San Diego
2008	Doctor of Philosophy in Earth Sciences University of California, San Diego

ABSTRACT OF THE DISSERTATION

A Method for Dynamic Earthquake Rupture Simulation with Applications to a Large Southern San Andreas Scenario

by

Geoffrey Palarz Ely
Doctor of Philosophy in Earth Sciences
University of California, San Diego, 2008
Professor Jean-Bernard Minster, Chair

Given the scarcity of near-source recordings for large earthquakes, numerical simulations play an important roll in the prediction of possible ground motion from future events. Simulations also give insight to physical processes of fault rupture that are difficult or impossible to empirically measure. In this dissertation I develop a numerical method to simulate spontaneous shear crack propagation within a heterogeneous, three-dimensional, viscoelastic medium. The implementation is highly scalable, enabling large scale, multi-processor calculations. Wave motions are computed on a logically rectangular hexahedral mesh, using the generalized finite difference method of Support Operators. This approach enables the modeling on nonplanar boundaries, as well as nonplanar ruptures. Computations are second-order in space and time. Stiffness and viscous hourglass corrections are employed to suppress suppress

zero-energy grid oscillation modes. Model boundaries may be reflective or absorbing, where absorbing boundaries are handled using the method of perfectly matched layers (PML). Three well known test problems are used to verify various aspects of the numerical method: wave propagation in a layered medium; surface amplification due to a semi-cylindrical canyon; and spontaneous rupture of a rectangular fault. Tests are repeated with varying amounts of simple shear deformation of the mesh. Sufficient accuracy is preserved under high-angle mesh shearing to permit modeling of thrust-earthquake geometries. The method is used to simulate a large (M_w7.6) earthquake scenarios along the southern San Andreas fault, using a piecewise planar fault representation and true topography of the ground surface. The crustal velocity structure is taken from the Southern California Earthquake Center Community Velocity Model (SCEC-CVM), which is currently the most complete three-dimensional model available for the region. Heterogeneous initial traction conditions are derived from an inversion of the M7.3 1992 Landers strong ground motion records. Heterogeneity in the traction model leads to focusing of the rupture front, in many cases producing super-shear rupture velocity in areas of high initial traction (asperities). Focusing sometimes occurs between the asperities, with the notable result that highest peak slip rates occur in areas of low initial traction. The overall distribution of simulated peak ground velocities is consistent with those derived from the current empirical models, with some important deviations associated with basin wave-guide and directivity effects.

Chapter 1

Introduction

Great strides have been made over the last century towards understanding the nature of earthquakes and the motions they produce at the surface of the earth. We are now able to make probabilistic earthquakes forecasts for many faults, and reasonably characterize possible ground motions. The science is being advanced on a number of fronts. Remarkable amounts of information on the structure of the earth and processes of fault rupture have been decoded from recordings of ground motion. Strain meters, GPS and satellite altimeters continuously track the deformation of the earth's crust. Fault surface traces, offsets, and tectonic deformations have been carefully mapped by geologists. Excavations of active faults have identified sequences of earthquake events going back thousands of years. We can even extract information about the intensity of such prehistoric earthquakes through mapping occurrences of precariously balanced rock formations, and measuring their tipping load. Much has been learned about the physics of friction and rupture from laboratory experiments with rock samples and other other materials. In conjunction with observational tools, scientists have developed increasingly sophisticated theoretical models and numerical simulation techniques. Collaboration among these diverse scientists, and the synthesis of their methods and findings, is seen as the most promising way forward. One of

the key objectives of much current research is the better understanding of earthquake sources. The basic obstacles we face are that fault ruptures occur deep under ground, commence without notice, last at most a couple of minutes, and recur on a time scale of centuries. This situation makes it very difficult to make detailed observations of the physical processes that govern fault rupture. One way that this gap has been filled is through numerical simulations.

The promise of numerical methods has grown as the performance of computers has continued to expand. However, the parallel architecture of today's fastest computers adds significant complexity to programming, and hinders full utilization the computational capacity. This raises the bar for any single scientist to perform large numerical simulations. For this reason, it is essential to have scalable, high quality codes, that are freely available as a community resource. Towards this goal, we have developed a new numerical tool for simulating earthquakes called the Support Operator Rupture Dynamics (SORD) code. This dissertation describes the theory and development of the numerical scheme, as well as its applications to real problems. We use SORD to investigate idealized wave propagation and rupture dynamics problems and to simulate potential future earthquakes using realistic fault and basin models.

Chapter 2 develops the method for simulating three dimensional visco-elastic wave propagation based on the generalized finite difference method of Support Operators (SOM). It serves as a framework for rupture dynamics simulations in the following chapters. The discretization used is a partially staggered, logically rectangular hexahedral mesh. This allows for non-planar surfaces to be incorporated into the medium, though it does not provide as much geometrical flexibility as a fully unstructured mesh. A major benefit of the logically rectangular structure over unstructured meshes, however, is that parallelization of the computational algorithm is greatly simplified. In benchmark tests using up to 512 processors, the code performs at 85%

efficiency, and the slope of the efficiency curve is nearly flat, indicating that the code will continue to scale well up to higher number of processors. Through the SOM derivation, spatial derivative operators are constructed that obey a discrete analog of the negative adjoint relation of the gradient and divergence. This property ensures that the spatial derivative operators conserve discrete energy. The derivation also naturally gives rise to a free surface boundary condition that is also conservative. The method is initially developed for arbitrary dimensionality and order of accuracy. I then apply it to the specific case to 3D, second order operators. Second order methods that use the partially staggered hexahedral discretization are susceptible to zero-energy grid oscillation modes that can be problematic for applications incorporating non-linear physics, such as rupture dynamics modeling. Zero-energy modes are suppressed with both stiffness and viscous 'hourglass' corrections. Artificial domain boundaries are made to absorb nearly all incident waves using the method of perfectly matched layers (PML). A slight reformulation of previous PML implementations is presented that reduces computations and memory storage. To verify the accuracy of the numerical scheme we use a set of two test problems, designed to assess most of the important capabilities. The first test is a layered model with a buried double-couple source. A simple shearing is applied to the mesh to assess any bias introduced from mesh deformation. The problem can be independently computed with the frequency wavenumber method. Velocity time histories at the free surface match frequency wavenumber solutions (with up to 1% error in amplitude and timing) when the waves are sampled with at least 10 grid points per wavelength. The second test imposes a vertically incident P-wave onto a semi-cylindrical canyon at the free surface. The problem has been studied by multiple authors using boundary integral methods. SOM solutions give a close match to surface amplifications when the resolution is at least 20 points per wavelength.

Chapter 3 lays out the theory and numerical scheme for solving spontaneous rupture dynamics problems with SOM. The fault is modeled with pairs of co-located mesh nodes along the fault surface that are coupled by a traction boundary condition. The method is verified against boundary integral solutions with a slip-weakening friction law. The accuracy of the method is established on meshes sheared by up to 70 degrees (i.e., sufficient to model rupture in shallow-angle thrust earthquakes). We go on to investigate the effects of kinked and curved fault geometry.

In Chapter 4 the SOM method is applied to simulating M_w7.6 earthquake scenarios on the southern San Andreas fault. The models follow closely the TeraShake2.2 calculation by *Olsen et al.* (2008). The primary difference is that the geometric flexibility of the SOM scheme allows for computing non-planar rupture dynamics, as well as surface topography effects, whereas TeraShake2.2 was confined to a rectangular grid. A planar and segmented fault geometry is used, and the initial tractions on the fault are derived from the inversion of strong ground motion recordings of the M_w7.3 Landers earthquake by *Peyrat et al.* (2001). Strong rupture focusing effects are observed in the dynamic rupture solutions. Waves are propagated through the Southern California Earthquake Center Community Velocity Model (SCEC-CVM), currently the most complete three-dimensional velocity model available for southern California (*Magistrale et al.*, 2000; *Kohler et al.*, 2003; *Magistrale*, 2005). We compare models using version 3.0 and version 4.0 of the SCEC-CVM, as well as models with and without the inclusion of Earth topography at the free surface. Ground motions predicted by the simulations are in general agreement to the recent empirical model by *Campbell and Bozorgnia* (2007), although three-dimensional basin effects cause some deviations. The models are computationally expensive, and provided a further benchmark of code performance, attaining 85% efficiency using 1920 processors.

The conclusions chapter (5) summarizes our findings and proposes possible future

research directions in rupture physics and strong ground motions modeling. Chapter 6 provides documentation for the SORD code and includes annotated input files used to produce the various simulations.

References

Campbell, K. W., and Y. Bozorgnia (2007), Campbell-Bozorgnia NGA ground motion relations for the geometric mean horizontal component of peak and spectral ground motion parameters, *Tech. Rep. PEER 2007/02*, Pacific Earthquake Engineering Research Center.

Kohler, M. D., H. Magistrale, and R. W. Clayton (2003), Mantle heterogeneities and the SCEC reference three-dimensional seismic velocity model version 3, *Bull. Seism. Soc. Am.*, *93*(2), 757–774, doi:10.1785/0120020017.

Magistrale, H. (2005), Version 4 of the CVM, 2005 SCEC Annual Meeting, Palm Springs, CA.

Magistrale, H., S. M. Day, R. W. Clayton, and R. W. Graves (2000), The SCEC southern California reference three-dimensional seismic velocity model version 2, *Bull. Seism. Soc. Am.*, *90*(6B), S65–76, doi:10.1785/0120000510.

Olsen, K. B., S. M. Day, J.-B. Minster, Y. Cui, A. Chourasia, D. Okaya, P. Maechling, and T. Jordan (2008), TeraShake2: spontaneous rupture simulations of M_w7.7 earthquakes on the southern San Andreas fault, *Bull. Seism. Soc. Am.*, in press.

Peyrat, S., K. B. Olsen, and R. Madariaga (2001), Dynamic modeling of the 1992 Landers earthquake, *J. Geophys. Res.*, *106*(B11), 26,467, doi:10.1029/2001JB000205.

Chapter 2

A Support-Operator Method for Viscoelastic Wave Modeling in 3D Heterogeneous Media

Abstract

We apply the method of Support Operators (SOM) to solve the three dimensional, viscoelastic equations of motion for use in earthquake simulations. SOM is a generalized finite-difference method that can utilize meshes of arbitrary structure and incorporate irregular geometry. Our implementation uses a 3D, logically-rectangular, hexahedral mesh. Calculations are second-order in space and time. A correction term is employed for suppression of spurious zero-energy modes (hourglass oscillations). We develop a free surface boundary condition, and an absorbing boundary condition using the method of Perfectly Matched Layers (PML). Numerical tests using a layered material model in a highly deformed mesh show good agreement with the frequency-wavenumber method, for resolutions greater than 10 nodes per wave-

length. We also test a vertically incident P wave on a semi-circular canyon, for which results match boundary integral solutions at resolutions greater that 20 nodes per wavelength. We also demonstrate excellent parallel scalability of our code.

2.1 Introduction

The finite-difference method (FDM) has been extensively used for modeling three-dimensional seismic wave propagation and rupture-dynamics problems. The fourth-order staggered-grid scheme, nicely summarized by *Graves* (1996), is particularly well suited for large-scale, high-resolution problems because it is accurate, efficient, and readily parallelized for multiprocessor execution. Recent applications include basin wave propagation by *Olsen et al.* (2006) and rupture dynamics by *Dalguer and Day* (2007).

Many such FDM implementations, however, are restricted to rectilinear discretizations of the problem domain, which in some cases leads to a poor approximation of problem geometry. Surface topography, for example, may be neglected. *Ma et al.* (2007) show with finite-element simulations that the topography of the San Bernardino Mountains may disrupt surface waves generated on the adjacent San Andreas Fault, effectively shielding Los Angeles. The restriction to rectilinear meshes also represents a severe constraint on dynamic rupture simulations, usually restricting consideration to planar, vertical faults that coincide with grid planes. This constraint can be relaxed, as in *Cruz-Atienza* (2006), for example, but at a substantial sacrifice of accuracy. Alternatively, a coordinate mapping can be introduced to conform the FDM grid to a non-planar fault geometry, as in *Kase and Day* (2006), for example.

A variety of approaches have been taken to enable non-rectangular geometry in earthquake simulations. To cite a few examples, *Aagaard* (1999) used the finite element method (FEM) on tetrahedral meshes; *Oglesby* (1999), and *Oglesby et al.* (2000)

employed FEM on hexahedral meshes; *Komatitsch and Tromp* (1999) used the spectral element method; and *Dumbser and Kašer* (2006) used a high-order discontinuous Galerkin method.

We apply the method of Support-Operators (SOM) developed by *Samarskii et al.* (1981, 1982) and *Shashkov* (1996). SOM is a general scheme for discretizing the differential form of partial differential equations. Many simple FDMs and FEMs are special cases of SOM. The approach constructs discrete analogs of continuum derivative operators that satisfy important integral identities, such as the adjoint relation between gradient and divergence. SOM brings to an FDM-type formulation the FEM advantage that energy is conserved in the semi-discrete equations (i.e., spatially discrete but before time discretization), as an immediate consequence of the adjoint relations. Likewise, the adjoint relations ensure that seismic reciprocity is satisfied by the fully discrete equations.

SOM may employ structured or unstructured meshes, and be extended to high order of accuracy. We develop the theory for arbitrary order on structured meshes, and implement the second order case for our numerical algorithm. *Rojas et al.* (2008) use a related finite difference formulation to model earthquake rupture dynamics in 2D. They implement a fourth-order scheme, but restrict it to Cartesian meshes. Their approach is similar to ours, in that they form the difference operators using the adjoint relations, but differs from our SOM formulation in the nature of the mesh employed (they use a staggered mesh of the form used in, e.g., *Levander* (1988)).

This paper begins with a derivation of 3D SOM spatial difference operators, followed by a comparison to the related method of one-point quadrature. A full listing of both types of operators is located in the appendix. We then lay-out the numerical algorithm for solving wave equations with hourglass corrections, and Perfectly Matched Layer (PML) absorbing boundaries. Presented next are numerical tests us-

ing a layered model, that is verified against wavenumber integration solutions, and a semi-circular canyon model that is verified against boundary integral solutions. Finally, we examine the parallel processing capability of our algorithm. In the concluding discussion, we look at potential enhancements to, and applications of our method.

2.2 The Support Operator Method

The linearized equations of motion for isotropic viscoelastic motion are

$$g_{ij} = \partial_j(u_i + \gamma v_i) \ , \tag{2.1}$$

$$\sigma_{ij} = \lambda \, \delta_{ij} \, g_{kk} + \mu(g_{ij} + g_{ji}) \ , \tag{2.2}$$

$$a_i = \frac{1}{\rho} \, \partial_j \sigma_{ij} \ , \tag{2.3}$$

$$\dot{v}_i = a_i \ , \tag{2.4}$$

$$\dot{u}_i = v_i \ , \tag{2.5}$$

where $\boldsymbol{\sigma}$ is the stress tensor, $\mathbf{u}$ and $\mathbf{v}$ are displacement and velocity vectors, ρ is density, λ and μ are elastic moduli, and γ is viscosity. The Kelvin-Voigt model of viscosity used here is not of a realistic form for seismological problems, but is included in the formulation in anticipation of future applications to nonlinear problems (e.g., rupture dynamics) where viscous losses may be needed for numerical regularization. Realistic attenuation can be readily added by the memory-variable technique introduced by *Day and Minster* (1984) and since refined by various authors (*Moczo et al.*, 2006, provide a comprehensive review). All variables are functions of position $\mathbf{x}$, while $\boldsymbol{\sigma}$, $\mathbf{u}$, and $\mathbf{v}$ are time dependent as well. It is generally not possible to find analytical

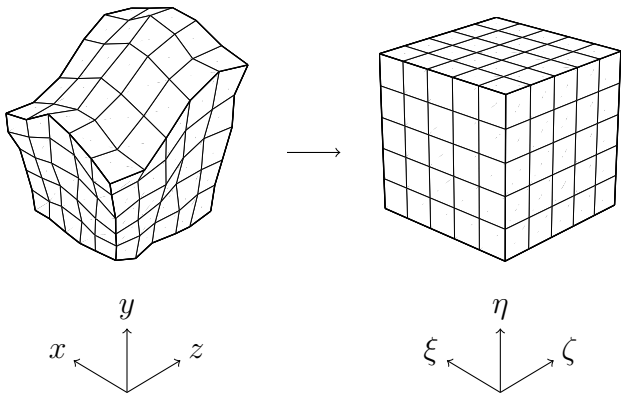

Figure 2.1: Map of Cartesian space to logical space

solutions to this system of equations, so we must rely on numerical methods to find approximate solutions.

We first discretize the field variables and material constants onto a hexahedral mesh that has a logically rectangular structure. We adapt the general formalism of *Shashkov* (1996) to the equations of 3D elastodynamics. Following that general formalism, we define two types of spatial discretizations on the mesh. Nodal functions are defined at the node points. We denote the space of nodal functions by H^N. Cell functions represent average function values over element volumes. We denote the space of cell functions by H^C. Mesh node points are located in the 3D logical structure by their indices j, k and l, and each interior node is shared by exactly eight elements. For the structured mesh there is a mapping from Cartesian space to logical space, $\mathbf{x} \rightarrow \boldsymbol{\xi}$ (Fig. 2.1), and the nodal coordinates $\mathbf{X}_{jkl} \in H^N$ map to the logical coordinates $\boldsymbol{\Xi}_{jkl}$.

We will need two types of discrete difference operators, one that operates on nodal functions and one that operates on cell functions. We begin with the derivation of the first one: an operator that computes the derivative of a nodal function with a cell function result. Consider the nodal discretization of an unknown function: $F_{jkl} \in H^N$. Polynomial interpolation of the discrete function F_{jkl} can be used to construct a

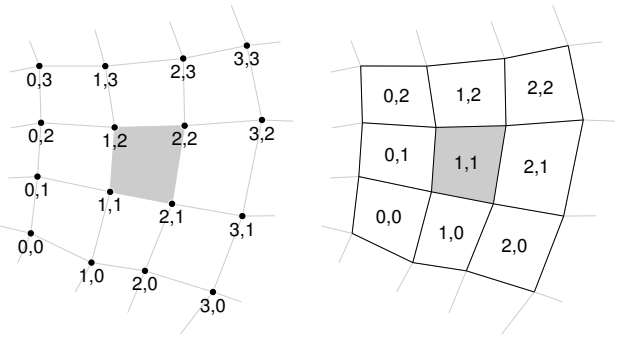

Figure 2.2: Stencil node and cell indexing for cubic ($n = 3$) interpolation in the shaded cell (1,1). For simplicity only two dimensions are shown instead of three.

continuous function $f(\boldsymbol{\xi})$ that is an approximation to the original unknown function. Provided the original function is smooth and well behaved, the error of approximation depends on the polynomial degree n.

We restrict the interpolation scheme such that, for a particular cell, $f(\boldsymbol{\xi})$ depends only on the nodes in the immediate vicinity. This group of nodes is called the stencil, and is diagrammed in Fig. 2.2. The stencil nodes have the indices $j, k, l = 0, \ldots, n$ and the stencil cells have the indices $j, k, l = 0, \ldots, n-1$. The value of n must be odd to insure logical symmetry about the central cell. The index of the central cell is (m, m, m) where $m = (n-1)/2$.

The interpolation function is given by

$$f(\boldsymbol{\xi}) = \sum_{j,k,l=0}^{n} N_{jkl}(\boldsymbol{\xi}) F_{jkl} \ , \tag{2.6}$$

where the shape functions $N_{jkl}(\boldsymbol{\xi})$ are formed from Lagrange interpolation polynomials

$$N_{jkl}(\boldsymbol{\xi}) = \ell_j^n(\xi)\ell_k^n(\eta)\ell_l^n(\zeta) \ , \tag{2.7}$$

and the Lagrange polynomials of degree n are given by

$$\ell_j^n(\xi) = \prod_{\substack{i=0 \\ i \neq j}}^{n} \frac{\xi - \Xi_i}{\Xi_j - \Xi_i} \ . \tag{2.8}$$

Evaluating the shape functions at the nodes gives

$$N_{jkl}(\boldsymbol{\Xi}_{pqr}) = \delta_{jp}\delta_{kq}\delta_{lr} \ , \tag{2.9}$$

so evaluating the interpolation function at the mesh nodes returns exactly the discrete function values

$$f(\boldsymbol{\Xi}_{jkl}) = F_{jkl} \ . \tag{2.10}$$

Repeating the interpolation procedure for the nodal coordinates $\mathbf{X}_{jkl}$ results in a mapping from logical coordinates to Cartesian coordinates,

$$\mathbf{x}(\boldsymbol{\xi}) = \sum_{j,k,l=0}^{n} N_{jkl}(\boldsymbol{\xi})\mathbf{X}_{jkl} \ . \tag{2.11}$$

We can use this mapping to find the gradient of f by solving the system of equations

$$\begin{aligned} \frac{\partial f}{\partial \boldsymbol{\xi}} &= (\nabla f) \cdot \frac{\partial \mathbf{x}}{\partial \boldsymbol{\xi}} \ , \\ \begin{bmatrix} \dfrac{\partial f}{\partial \xi} & \dfrac{\partial f}{\partial \eta} & \dfrac{\partial f}{\partial \zeta} \end{bmatrix} &= \begin{bmatrix} \dfrac{\partial f}{\partial x} & \dfrac{\partial f}{\partial y} & \dfrac{\partial f}{\partial z} \end{bmatrix} \begin{bmatrix} \dfrac{\partial x}{\partial \xi} & \dfrac{\partial x}{\partial \eta} & \dfrac{\partial x}{\partial \zeta} \\ \dfrac{\partial y}{\partial \xi} & \dfrac{\partial y}{\partial \eta} & \dfrac{\partial y}{\partial \zeta} \\ \dfrac{\partial z}{\partial \xi} & \dfrac{\partial z}{\partial \eta} & \dfrac{\partial z}{\partial \zeta} \end{bmatrix} . \end{aligned} \tag{2.12}$$

The matrix $\mathbf{J} = \partial \mathbf{x}/\partial \boldsymbol{\xi}$ is known as the Jacobian of the mapping. Columns of $\mathbf{J}$ are tangent vectors to the logical coordinate system. The determinant of the Jacobian

$J = |\mathbf{J}|$ relates volume elements between the logical and Cartesian coordinate systems

$$dx\,dy\,dz = J\,d\xi\,d\eta\,d\zeta\ . \tag{2.13}$$

The inverse of the Jacobian matrix is

$$\mathbf{J}^{-1} = \frac{\partial \boldsymbol{\xi}}{\partial \mathbf{x}} = \frac{1}{J}\begin{bmatrix} \begin{vmatrix} \frac{\partial y}{\partial \eta} & \frac{\partial z}{\partial \eta} \\ \frac{\partial y}{\partial \zeta} & \frac{\partial z}{\partial \zeta} \end{vmatrix} & \begin{vmatrix} \frac{\partial z}{\partial \eta} & \frac{\partial x}{\partial \eta} \\ \frac{\partial z}{\partial \zeta} & \frac{\partial x}{\partial \zeta} \end{vmatrix} & \begin{vmatrix} \frac{\partial x}{\partial \eta} & \frac{\partial y}{\partial \eta} \\ \frac{\partial x}{\partial \zeta} & \frac{\partial y}{\partial \zeta} \end{vmatrix} \\ \begin{vmatrix} \frac{\partial y}{\partial \zeta} & \frac{\partial z}{\partial \zeta} \\ \frac{\partial y}{\partial \xi} & \frac{\partial z}{\partial \xi} \end{vmatrix} & \begin{vmatrix} \frac{\partial z}{\partial \zeta} & \frac{\partial x}{\partial \zeta} \\ \frac{\partial z}{\partial \xi} & \frac{\partial x}{\partial \xi} \end{vmatrix} & \begin{vmatrix} \frac{\partial x}{\partial \zeta} & \frac{\partial y}{\partial \zeta} \\ \frac{\partial x}{\partial \xi} & \frac{\partial y}{\partial \xi} \end{vmatrix} \\ \begin{vmatrix} \frac{\partial y}{\partial \xi} & \frac{\partial z}{\partial \xi} \\ \frac{\partial y}{\partial \eta} & \frac{\partial z}{\partial \eta} \end{vmatrix} & \begin{vmatrix} \frac{\partial z}{\partial \xi} & \frac{\partial x}{\partial \xi} \\ \frac{\partial z}{\partial \eta} & \frac{\partial x}{\partial \eta} \end{vmatrix} & \begin{vmatrix} \frac{\partial x}{\partial \xi} & \frac{\partial y}{\partial \xi} \\ \frac{\partial x}{\partial \eta} & \frac{\partial y}{\partial \eta} \end{vmatrix} \end{bmatrix}\ . \tag{2.14}$$

Rows of $J\mathbf{J}^{-1}$ are surface area vectors $d\mathbf{S}$ for surfaces of constant ξ, η or ζ, and are formed by cross products of the tangent vectors. Solving (2.12) gives the gradient of f:

$$\nabla f = \frac{\partial f}{\partial \boldsymbol{\xi}} \cdot \mathbf{J}^{-1}\ . \tag{2.15}$$

Because we seek the average gradient over the element volume, we will use the approximation

$$\nabla f \approx \frac{1}{V}\int_V \nabla f\,dV\ , \tag{2.16}$$

and define discrete operators D_x, D_y and D_z:

$$D_i F \equiv \int_{V^C} \frac{\partial f}{\partial x_i}\,dV\ , \tag{2.17}$$

$$D_i : H^N \rightarrow H^C\ , \tag{2.18}$$

where V^C is the volume of the central cell enclosed by the logical coordinates

$$\begin{aligned} \xi_m < \xi < \xi_{m+1} \ , \\ \eta_m < \eta < \eta_{m+1} \ , \\ \zeta_m < \zeta < \zeta_{m+1} \ . \end{aligned} \tag{2.19}$$

Substituting (2.13), (2.15) and (2.19) into (2.17) gives

$$\hat{\mathbf{x}} D_x F + \hat{\mathbf{y}} D_y F + \hat{\mathbf{z}} D_z F = \int_{\zeta} \int_{\eta} \int_{\xi} \frac{\partial f}{\partial \boldsymbol{\xi}} \cdot \mathbf{J}^{-1} J \, d\xi \, d\eta \, d\zeta \ . \tag{2.20}$$

A computer algebra system is helpful for solving this integral. The remainder of this paper is concerned with the 3D, linear case ($n = 1$). The resulting expressions for D_i are rather complex and are not available elsewhere, so we tabulate them in the Appendix. If elements are restricted in shape to rectangular parallelepipeds, the operators simplify to

$$\begin{aligned} (D_x F)_{000} = \tfrac{1}{4}(Z_1 - Z_0)(Y_1 - Y_0) \\ (F_{111} + F_{100} - F_{010} - F_{001} \\ -F_{000} - F_{011} + F_{101} + F_{110}) \ , \end{aligned} \tag{2.21}$$

$$\begin{aligned} (D_y F)_{000} = \tfrac{1}{4}(X_1 - X_0)(Z_1 - Z_0) \\ (F_{111} - F_{100} + F_{010} - F_{001} \\ -F_{000} + F_{011} - F_{101} + F_{110}) \ , \end{aligned} \tag{2.22}$$

and

$$(D_z F)_{000} = \tfrac{1}{4}(Y_1 - Y_0)(X_1 - X_0) \\ (F_{111} - F_{100} - F_{010} + F_{001} \\ -F_{000} + F_{011} + F_{101} - F_{110}) \ , \tag{2.23}$$

each of which is recognizable as the average of four separate finite-difference operations along the cell edges.

Now that we have the difference operator D_i that operates on the nodal functions, the next task is to build a complementary difference operator that operates on a cell function and returns a nodal function:

$$\mathcal{D}_i : H^C \rightarrow H^N \ . \tag{2.24}$$

We will rely on the previously derived operators D_i and the adjoint relation between gradient and divergence. The goal is to ensure global conservation of the numerical scheme. This is the guiding principle of SOM and other mimetic methods. They attempt to 'mimic' fundamental conservation laws of the continuum. In this case D_i is called the natural operator and $\mathcal{D}_i$ is called the support operator.

Applying the divergence theorem to the product $f\mathbf{w}$ gives

$$\int_V (\nabla f) \cdot \mathbf{w} \, dV + \int_V f(\nabla \cdot \mathbf{w}) \, dV = \int_S f\mathbf{w} \cdot \mathbf{dS} \ . \tag{2.25}$$

When the normal component of $\mathbf{w}$ at the boundary surface is 0,

$$\int_V f \nabla \cdot \mathbf{w} \, dV = - \int_V (\nabla f) \cdot \mathbf{w} \, dV \ , \tag{2.26}$$

which expresses the fact that gradient and divergence are adjoint operators. The

adjoint relationship has the discrete analog

$$\sum_{i,j,k,l=0}^{3,p-1,q-1,r-1} (D_i F)_{jkl}(W_i)_{jkl} = -\sum_{i,j,k,l=0}^{3,p,q,r} F_{jkl}(\mathcal{D}_i W_i)_{jkl} \ , \tag{2.27}$$

where $\mathbf{W}_{jkl} \in H^C$ is a cell-valued vector function. Until this point we have considered only the local vicinity of the difference operator. Here we broaden the scope to the global problem domain, where the mesh size is $p \times q \times r$.

Inserting $D_i F$ into the left hand side of (2.27) results in a summation factored in terms of common $\mathbf{W}_{jkl}$ values. We can re-factor this summation in terms of common F_{jkl}. Equating this result to the right hand side of (2.27), we can write the expressions for $\mathcal{D}_i$ as listed in the Appendix. On a rectangular mesh the equations simplify to

$$\begin{aligned}(\mathcal{D}_x \mathbf{W})_{111} = \tfrac{1}{4}(Z_2 - Z_1)\Big[&(Y_2 - Y_1)(\mathbf{W}_{111} - \mathbf{W}_{011}) \\ &+(Y_1 - Y_0)(\mathbf{W}_{101} - \mathbf{W}_{001})\Big] \\ +\tfrac{1}{4}(Z_1 - Z_0)\Big[&(Y_2 - Y_1)(\mathbf{W}_{110} - \mathbf{W}_{010}) \\ &+(Y_1 - Y_0)(\mathbf{W}_{100} - \mathbf{W}_{000})\Big],\end{aligned} \tag{2.28}$$

$$\begin{aligned}(\mathcal{D}_y \mathbf{W})_{111} = \tfrac{1}{4}(X_2 - X_1)\Big[&(Z_2 - Z_1)(\mathbf{W}_{111} - \mathbf{W}_{101}) \\ &+(Z_1 - Z_0)(\mathbf{W}_{110} - \mathbf{W}_{100})\Big] \\ +\tfrac{1}{4}(X_1 - X_0)\Big[&(Z_2 - Z_1)(\mathbf{W}_{011} - \mathbf{W}_{001}) \\ &+(Z_1 - Z_0)(\mathbf{W}_{010} - \mathbf{W}_{000})\Big],\end{aligned} \tag{2.29}$$

$$\begin{aligned}(\mathcal{D}_z \mathbf{W})_{111} = \tfrac{1}{4}(Y_2 - Y_1)\Big[&(X_2 - X_1)(\mathbf{W}_{111} - \mathbf{W}_{110}) \\ &+(X_1 - X_0)(\mathbf{W}_{011} - \mathbf{W}_{010})\Big] \\ +\tfrac{1}{4}(Y_1 - Y_0)\Big[&(X_2 - X_1)(\mathbf{W}_{101} - \mathbf{W}_{100}) \\ &+(X_1 - X_0)(\mathbf{W}_{001} - \mathbf{W}_{000})\Big].\end{aligned} \tag{2.30}$$

At the boundaries, certain terms in $\mathcal{D}_i$ drop out. For example at the boundary $j = 0$, (2.28), (2.29) and (2.30) reduce to

$$\begin{aligned}(\mathcal{D}_x\mathbf{W})_{011} = \tfrac{1}{4}(Z_2 - Z_1)\Big[&(Y_2 - Y_1)\mathbf{W}_{011} \\ &+(Y_1 - Y_0)\mathbf{W}_{001}\Big] \\ +\tfrac{1}{4}(Z_1 - Z_0)\Big[&(Y_2 - Y_1)\mathbf{W}_{010} \\ &+(Y_1 - Y_0)\mathbf{W}_{000}\Big],\end{aligned} \tag{2.31}$$

$$\begin{aligned}(\mathcal{D}_y\mathbf{W})_{011} = \tfrac{1}{4}(X_2 - X_1)\Big[&(Z_2 - Z_1)(\mathbf{W}_{011} - \mathbf{W}_{001}) \\ &+(Z_1 - Z_0)(\mathbf{W}_{010} - \mathbf{W}_{000})\Big],\end{aligned} \tag{2.32}$$

and

$$\begin{aligned}(\mathcal{D}_z\mathbf{W})_{011} = \tfrac{1}{4}(X_2 - X_1)\Big[&(Y_2 - Y_1)(\mathbf{W}_{011} - \mathbf{W}_{010}) \\ &+(Y_1 - Y_0)(\mathbf{W}_{001} - \mathbf{W}_{000})\Big].\end{aligned} \tag{2.33}$$

Accounting for each face, edge and corner of the mesh, there exist 48 different boundary operators for $\mathcal{D}_i$. The application of the boundary operators is simplified in practice by using a ghost cell technique. We extend the mesh outside of the boundaries with 'ghost' cells, and in those cells $\mathbf{W}_{jkl}$ is always zero. Applying the interior operators (2.28), (2.29) and (2.30) to the expanded mesh reproduces the boundary operators appropriately.

We can now approximate the partial derivative of F with

$$\frac{(D_iF)_{jkl}}{V^C_{jkl}}\ , \tag{2.34}$$

and approximate the partial derivative of $\mathbf{W}$ with

$$\frac{(\mathcal{D}_i \mathbf{W})_{jkl}}{V^N_{jkl}} \ , \tag{2.35}$$

where V^C_{jkl} is the cell volume and V^N_{jkl} is the nodal volume. The cell volume can be found by noting that

$$\int_V \frac{\partial x_i}{\partial x_i} dV = V \ , \tag{2.36}$$

and differencing any one of the nodal coordinates

$$V^C_{jkl} = (D_x X)_{jkl} = (D_y Y)_{jkl} = (D_z Z)_{jkl} \ . \tag{2.37}$$

The nodal volume is then found by averaging the surrounding eight cell volumes

$$\begin{aligned} V^N_{000} = \tfrac{1}{8}\Big(& V^C_{000} + V^C_{011} + V^C_{101} + V^C_{110} \\ & + V^C_{111} + V^C_{100} + V^C_{010} + V^C_{001} \Big) \ . \end{aligned} \tag{2.38}$$

2.3 One-point Quadrature

The gradient operator D_i is defined in equation (2.17) by exactly integrating the integral (2.16). An alternative method is to approximate the integral with numerical quadrature. For one-point quadrature we simply evaluate equation (2.15) at the center of the stencil

$$D_i F \equiv \left. \frac{\partial f}{\partial x_i} \right|_{\boldsymbol{\xi} = (\boldsymbol{\xi}_m + \boldsymbol{\xi}_{m+1})/2} \ . \tag{2.39}$$

The resulting operators, equations (2.98) through (2.103) listed in the Appendix, offer some computational savings. One-point quadrature has been frequently applied to seismic problems (see e.g., *Day et al.*, 2005; *Ma and Liu*, 2006). The operator D_i is often called the 'B matrix' in FEM literature. *Goudreau and Hallquist* (1982) found that

for their applications, exactly integrated elements perform no better than one-point quadrature, and therefore the extra computational expense is not justified. However, this may not be true for all applications. With non-parallelepiped elements, one-point quadrature fails the patch test. One consequence of this is that rigid body motion can lead to non-zero stress. To illustrate, from equations (2.98) through (2.102), the one-point quadrature gradient $D_i F$ clearly evaluates to zero when F is uniform. However, the divergence $\mathcal{D}_i \mathbf{W}$, listed in equations (2.99) through (2.103), does not in general evaluate to zero when $\mathbf{W}$ is uniform. The non-physical consequence is that energy can enter the system due simply to the shape of the mesh. Conversely, the exactly integrated operators, equations (2.92) through (2.97) always evaluate to zero for uniform fields F and $\mathbf{W}$. We have not established whether, in practice, this is an important issue for seismic wave simulations, but violation of conservation of energy is clearly undesirable and should be avoided if possible.

The exactly integrated elements require roughly twice as many floating point operations to compute. However, the difference can be negated, and additional computational efficiency achieved, by holding the operators in memory rather than calculating them on-the-fly. One can store D_i in a memory array, and $\mathcal{D}_i$ can be had directly from D_i via the adjoint relation. Storage of D_i requires 24 memory variables per element, while storage of $\mathbf{X}$ for on-the-fly operators requires three variables per element. The 21 variable increase roughly doubles the amount of storage needed overall, while the number of floating point operations is reduced by a factor of six for the complete algorithm.

Tests of our code (summarized in Table 2.1), under ideal conditions with no parallel processing or file output, show a 25% reduction in runtime for one-point quadrature, and a factor of 3 reduction for precomputed operators. This is only half of the speedup expected considering only floating point operations. However, memory

Table 2.1: Resource usage per node per time time step for different operators. Numbers are for the complete wave simulation algorithm.

Operator type	Floating pt. ops.	Memory variables	Normalized run-time
Exactly integrated	3380	23	3.56
One-point quadrature	1688	23	2.67
Stored operators	518	44	1.27
Rectangular	446	20	1.00

access speed can be an equally important factor on architectures with fast CPUs. Parallel processing overhead and file access reduce even further the relative speed gains. Due to the modest performance penalty, and the potential for removing that penalty altogether by precomputed operators, we prefer the exactly integrated elements.

2.4 Numerical Algorithm

We can now build an explicit time-stepping scheme by discretizing equations (2.1) through (2.5). The continuous field variables are replaced with discrete variables of the same name. On the nodes we have $(\mathbf{u}, \mathbf{v}, \mathbf{a}, \rho, \gamma, \mathbf{g}) \in H^N$, and on the cells we have $(\boldsymbol{\sigma}, \lambda, \mu) \in H^C$. Time is discretized with constant spacing Δt. Spatial derivative are approximated with the operators (2.34) and (2.35) and time derivatives are approximated with with second-order centered differences. The time index is indicated by a superscript, and for clarity, spatial indices are omitted in the discrete equations

$$g_{ij} = D_j(u_i^n + \gamma v_i^{n-1/2}) \ , \tag{2.40}$$

$$\sigma_{ij} = \Lambda \, \delta_{ij} g_{kk} + M(g_{ij} + g_{ji}) \ , \tag{2.41}$$

$$a_i = R\,\mathcal{D}_j\,\sigma_{ij}\ , \tag{2.42}$$

$$v_i^{n+1/2} = v_i^{n-1/2} + \Delta t\, a_i\ , \tag{2.43}$$

$$u_i^{n+1} = u_i^n + \Delta t\, v_i^{n+1/2}\ . \tag{2.44}$$

The material variables incorporate the cell and node volumes

$$R = \frac{1}{\rho V^N}\ , \tag{2.45}$$

$$\Lambda = \frac{\lambda}{V^C}\ , \tag{2.46}$$

$$M = \frac{\mu}{V^C}\ . \tag{2.47}$$

If material contrasts are to be aligned with the cell boundaries, it is most convenient to begin with an initial cell valued density function $\rho^C \in H^C$. Care must be taken to conserve global mass, and correctly align the material boundary when finding the nodal densities. This is achieved by weighting cell density by cell volume prior to averaging,

$$\begin{aligned} R_{000} = 8\Big(&V^C_{000}\rho^C_{000} + V^C_{011}\rho^C_{011} + V^C_{101}\rho^C_{101} + V^C_{110}\rho^C_{110} \\ &+V^C_{111}\rho^C_{111} + V^C_{100}\rho^C_{100} + V^C_{010}\rho^C_{010} + V^C_{001}\rho^C_{001}\Big)^{-1}. \end{aligned} \tag{2.48}$$

By the same principle, when material contrasts are to bisect the cells, it is most convenient to begin with initial nodal elastic moduli $(\lambda^N, \mu^N) \in H^N$, and compute the cell values by weighted harmonic averaging,

$$\begin{aligned} \Lambda_{111} = 8\Bigg(&\frac{V^N_{000}}{\lambda^N_{000}} + \frac{V^N_{011}}{\lambda^N_{011}} + \frac{V^N_{101}}{\lambda^N_{101}} + \frac{V^N_{110}}{\lambda^N_{110}} \\ &+\frac{V^N_{111}}{\lambda^N_{111}} + \frac{V^N_{100}}{\lambda^N_{100}} + \frac{V^N_{010}}{\lambda^N_{010}} + \frac{V^N_{001}}{\lambda^N_{001}}\Bigg)^{-1}, \end{aligned} \tag{2.49}$$

$$M_{111} = 8\left(\frac{V^N_{000}}{\mu^N_{000}} + \frac{V^N_{011}}{\mu^N_{011}} + \frac{V^N_{101}}{\mu^N_{101}} + \frac{V^N_{110}}{\mu^N_{110}} + \frac{V^N_{111}}{\mu^N_{111}} + \frac{V^N_{100}}{\mu^N_{100}} + \frac{V^N_{010}}{\mu^N_{010}} + \frac{V^N_{001}}{\mu^N_{001}}\right)^{-1} . \tag{2.50}$$

Stability of the explicit scheme requires that Δt be less than the shortest time for waves to traverse a cell. The condition

$$1 < \frac{\Delta t}{\Delta x}\sqrt{\frac{3(\lambda + 2\mu)}{\rho}} \tag{2.51}$$

is necessary to ensure stability for a rectangular mesh of constant spacing Δx, and can be used as an approximate guide for selecting stable time steps for non-rectangular meshes as well.

The 24 degrees of freedom for displacement on the eight node hexahedral element can be decomposed into three rigid body, nine uniform, and 12 non-uniform strain modes. The non-uniform modes are alternatively referred to as hourglass, keystone or bending modes. Hourglass modes are orthogonal to and transparent to single-point derivative operators such as we have derived. Unchecked they may grow to dominate the solution, so they must be independently controlled. We use a modified form of the hourglass control scheme described by *Flanagan and Belytschko* (1981) and more recently by *Day et al.* (2005) and *Ma and Liu* (2006). We define the hourglass operators

$$Q_i : H^N \rightarrow H^C \ , \tag{2.52}$$

$$(Q_1 F)_{000} = F_{000} + F_{011} - F_{101} - F_{110} + F_{111} + F_{100} - F_{010} - F_{001} \ , \tag{2.53}$$

$$(Q_2 F)_{000} = F_{000} + F_{101} - F_{110} - F_{011} + F_{111} + F_{010} - F_{001} - F_{100} \ , \tag{2.54}$$

$$\begin{aligned}(Q_3F)_{000} =& F_{000} + F_{110} - F_{011} - F_{101} \\ &+ F_{111} + F_{001} - F_{100} - F_{010} \ ,\end{aligned} \tag{2.55}$$

$$\begin{aligned}(Q_4F)_{000} =& F_{000} + F_{011} + F_{101} + F_{110} \\ &- F_{111} - F_{100} - F_{010} - F_{001} \ ,\end{aligned} \tag{2.56}$$

and

$$\mathcal{Q}_i : H^C \rightarrow H^N \ , \tag{2.57}$$

$$\begin{aligned}(\mathcal{Q}_1\mathbf{W})_{111} =& \mathbf{W}_{111} + \mathbf{W}_{100} - \mathbf{W}_{010} - \mathbf{W}_{001} \\ &+ \mathbf{W}_{000} + \mathbf{W}_{011} - \mathbf{W}_{101} - \mathbf{W}_{110} \ ,\end{aligned} \tag{2.58}$$

$$\begin{aligned}(\mathcal{Q}_2\mathbf{W})_{111} =& \mathbf{W}_{111} + \mathbf{W}_{010} - \mathbf{W}_{001} - \mathbf{W}_{100} \\ &+ \mathbf{W}_{000} + \mathbf{W}_{101} - \mathbf{W}_{110} - \mathbf{W}_{011} \ ,\end{aligned} \tag{2.59}$$

$$\begin{aligned}(\mathcal{Q}_3\mathbf{W})_{111} =& \mathbf{W}_{111} + \mathbf{W}_{001} - \mathbf{W}_{100} - \mathbf{W}_{010} \\ &+ \mathbf{W}_{000} + \mathbf{W}_{110} - \mathbf{W}_{011} - \mathbf{W}_{101} \ ,\end{aligned} \tag{2.60}$$

$$\begin{aligned}(\mathcal{Q}_4\mathbf{W})_{111} =& \mathbf{W}_{111} + \mathbf{W}_{100} + \mathbf{W}_{010} + \mathbf{W}_{001} \\ &- \mathbf{W}_{000} - \mathbf{W}_{011} - \mathbf{W}_{101} - \mathbf{W}_{110} \ .\end{aligned} \tag{2.61}$$

Viscous as well as stiffness hourglass control may be used, for which we define the viscosity β, and stiffness

$$\mathcal{Y} = \frac{\mu(\lambda + \mu)}{6(\lambda + 2\mu)} \ . \tag{2.62}$$

The correction is applied by modifying the acceleration equation (2.42), and the discrete equations now become:

$$g_{ij} = D_j(u_i^n + \gamma v_i^{n-1/2}) \ , \tag{2.63}$$

$$\sigma_{ij} = \Lambda \, \delta_{ij} g_{kk} + M(g_{ij} + g_{ji}) \ , \tag{2.64}$$

$$a_i = R\,\mathcal{D}_j\,\sigma_{ij} - \mathcal{Q}_k\,\mathcal{Y}\,Q_k(u_i^n + \beta v_i^{n-1/2}) \ , \tag{2.65}$$

$$v_i^{n+1/2} = v_i^{n-1/2} + \Delta t\, a_i \ , \tag{2.66}$$

$$u_i^{n+1} = u_i^n + \Delta t\, v_i^{n+1/2} \ . \tag{2.67}$$

The form we choose for hourglass stiffness $\mathcal{Y}$ is based on the approximate analysis of *Kosloff and Frazier* (1978). They found that the growth of the hourglass modes in 2D grids was effectively resisted with a stiffness of this form, and numerical experiments (*Day et al.*, 2005; *Ma and Liu*, 2006, e.g.) demonstrate that the same stiffness works well to suppress growth of the corresponding 3D modes, especially in combination with a damping β of order 1 (and results are not very sensitive to values of $\mathcal{Y}$ and β, once they are large enough to suppress mode growth).

2.5 Perfectly Matched Layer

Modeling waves in a boundless material requires artificial truncation of the computational domain. Various types of absorbing boundaries have been used to suppress artificial reflections at the boundaries. One of the most effective is the method of Perfectly Matched Layers (PML). First introduced for electromagnetic waves by *Berenger* (1994, 1996), PML sets up an absorbing layer where waves are exponentially attenuated and the reflection coefficient at the layer interface is nearly zero for all angles of incidence. *Marcinkovich and Olsen* (2003) present a PML absorbing boundary condition for the velocity-stress formulation of elastodynamics. We modify their given system of equations to find an equivalent formulation that offers a compact notation and that is more optimized numerically. The modification is a reordering of operations that results in damping of the spatial derivatives of velocity and stress rather than velocity and stress themselves. The change reduces the addi-

tional required storage from nine to six variables per damping direction, and reduces the number of multiplication operations. The modified formulation is

$$\dot{g}_{ij} + d(x_j) g_{ij} = \partial_j v_i \ , \tag{2.68}$$

$$\dot{\sigma}_{ij} = \lambda \, \delta_{ij} \sum_k \dot{g}_{kk} + \mu(\dot{g}_{ij} + \dot{g}_{ji}) \ , \tag{2.69}$$

$$\dot{p}_{ij} + d(x_j) p_{ij} = \partial_j \sigma_{ij} \ , \tag{2.70}$$

$$\dot{v}_i = \frac{1}{\rho} \sum_j \dot{p}_{ij} \ , \tag{2.71}$$

where $d(x_j)$ is the damping profile, and x_j is the distance measured from the node or cell location to the PML interface along the x, y, or z direction. Note that repeated indices do not imply summation here. In this formulation, the PML interface plane must be normal to one of the Cartesian directions. Where PML zones overlap, such as at the corners of the model, damping occurs in more than one direction. For the interior of the model, not in the PML, $d(x_i) = 0$, and the equations reduce to the elastic wave equations. This formulation is suitable for numerical schemes that store the elastic state as velocity and *stress*. In this paper, however, we have developed a scheme that stores velocity and *displacement*, so the system must be modified slightly to

$$\dot{g}_{ij} + d(x_j) g_{ij} = \partial_j v_i \ , \tag{2.72}$$

$$\sigma_{ij} = \lambda \, \delta_{ij} \sum_k g_{kk} + \mu(g_{ij} + g_{ji}) \ , \tag{2.73}$$

$$\dot{p}_{ij} + d(x_j) p_{ij} = \partial_j \sigma_{ij} \ , \tag{2.74}$$

$$a_i = \frac{1}{\rho} \sum_j \dot{p}_{ij} \ , \tag{2.75}$$

$$\dot{v}_i = a_i \ , \tag{2.76}$$

$$\dot{u}_i = v_i \ . \tag{2.77}$$

Discretizing equations (2.72) and (2.74) gives

$$\frac{g_{ij}^n - g_{ij}^{n-1}}{\Delta t} + d(x_i)\frac{g_{ij}^n + g_{ij}^{n-1}}{2} = D_j v_i^{n-1/2} \tag{2.78}$$

and

$$\frac{p_{ij}^{n+1/2} - p_{ij}^{n-1/2}}{\Delta t} + d(x_i)\frac{p_{ij}^{n+1/2} + p_{ij}^{n-1/2}}{2} = \mathcal{D}_j \sigma_{ij} \ , \tag{2.79}$$

from which we can build an explicit time stepping scheme for the PML similar to that for the viscoelastic solid in equations (2.63–2.67):

$$g_{ij}^n = \frac{2\Delta t}{2 + d(x_j)\Delta t} D_j v_i^{n-1/2} + \frac{2 - d(x_j)\Delta t}{2 + d(x_j)\Delta t} g_{ij}^{n-1} \ , \tag{2.80}$$

$$\sigma_{ij} = \Lambda \delta_{ij} \sum_k g_{kk}^n + M(g_{ij}^n + g_{ji}^n) \ , \tag{2.81}$$

$$\dot{p}_{ij} = \frac{2}{2 + d(x_i)\Delta t}\mathcal{D}_j \sigma_{ij} - \frac{2d(x_i)}{2 + d(x_i)\Delta t} p_{ij}^{n-1/2} \ , \tag{2.82}$$

$$a_i = R \sum_j \dot{p}_{ij} - \mathcal{Q}_k \, \mathcal{Y} \, Q_k(\beta v_i^{n-1/2}) \ , \tag{2.83}$$

$$p_{ij}^{n+1/2} = p_{ij}^{n-1/2} + \Delta t \, \dot{p}_{ij} \ , \tag{2.84}$$

$$v_i^{n+1/2} = v_i^{n-1/2} + \Delta t \, a_i \ , \tag{2.85}$$

$$u_i^{n+1} = u_i^n + \Delta t \, v_i^{n+1/2} \ . \tag{2.86}$$

For each direction of damping, six extra memory arrays are required for the storage of g_{1j}, g_{2j}, g_{3j}, p_{1j}, p_{2j}, and p_{3j}. The non-damped components of g_{ij} and p_{ij} need not be stored because, when $d(x_j) = 0$, equation (2.80) can be replaced by

$$g_{ij} = D_j u_i^n \ , \tag{2.87}$$

and equation (2.82) reduces to

$$\dot{p}_{ij} = \mathcal{D}_j \sigma_{ij}^n \ . \tag{2.88}$$

Ma and Liu (2006) have found that stiffness hourglass control can cause instability in the PML. Therefore, only viscous hourglass control is used in equation (2.83).

Following *Marcinkovich and Olsen*, the damping profile within the PML zone is given by

$$d(x) = \frac{3.5 V_s}{w} \left(\frac{x}{w} \right)^2 \left(\frac{8}{15} n - \frac{3}{100} n^2 + \frac{1}{1500} n^3 \right) \ , \tag{2.89}$$

where w is the PML thickness, n is the number of mesh nodes in the PML, and V_s is the harmonic mean of the minimum and maximum S-wave velocities present in the material model.

2.6 Layered Model Test

For numerical verification of the support-operator method, we reproduce the double-couple point source test LOH.1 from *Day and Bradley* (2001). The model, diagrammed in Fig. 2.3, consists of a 1 km layer over a uniform half-space. In the layer $V_s = 2{,}000\,\mathrm{m/s}$, $V_p = 4{,}000\,\mathrm{m/s}$, and density $\rho = 2600\,\mathrm{kg/m^3}$, and in the underlying half-space $V_s = 3{,}464\,\mathrm{m/s}$, $V_p = 6{,}000\,\mathrm{m/s}$, and $\rho = 2700\,\mathrm{kg/m^3}$. The model is purely elastic, so viscosity $\gamma = 0$, but we use a relatively high hourglass viscosity $\beta = \Delta t$. The time step length $\Delta t = 0.004\,\mathrm{s}$.

We do two calculations, one with a rectangular mesh of node spacing $\Delta x = 50\,\mathrm{m}$, and another with a mesh highly distorted by shearing. The sheared mesh is con-

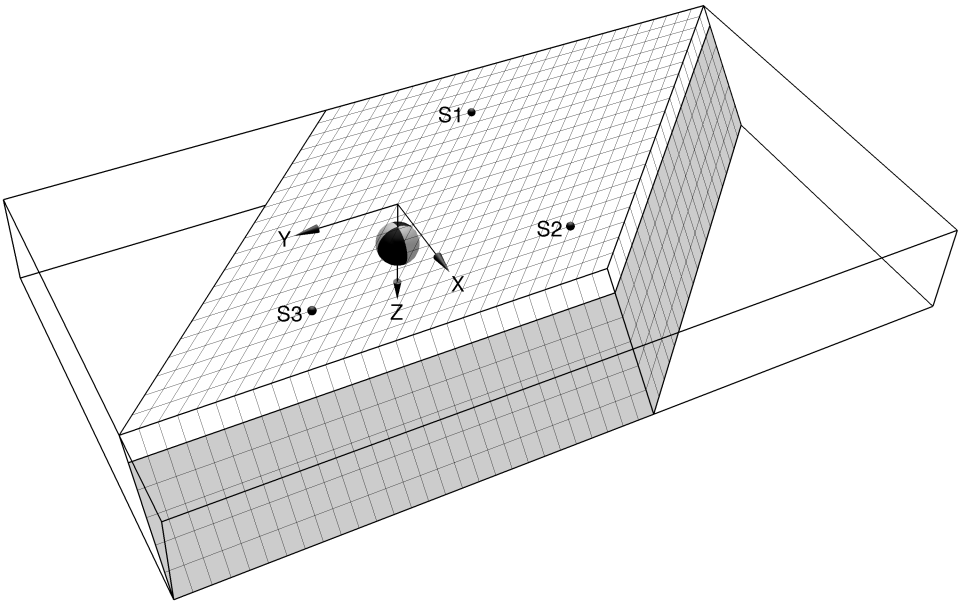

Figure 2.3: Perspective view of the layer over half-space model on a sheared mesh. The layer is 1 km thick. The source is located at 2 km depth, beneath the origin. Observation points are marked S1, S2 and S3.

structed from the rectangular mesh by applying the coordinate mapping

$$\begin{bmatrix} X'_{jkl} \\ Y'_{jkl} \\ Z'_{jkl} \end{bmatrix} = \begin{bmatrix} 1 & 0 & 1 \\ 1 & 1 & 0 \\ 0 & 0 & 1 \end{bmatrix} \begin{bmatrix} X_{jkl} \\ Y_{jkl} \\ Z_{jkl} \end{bmatrix}, \tag{2.90}$$

where (X, Y, Z) are coordinates of the rectangular mesh and (X', Y', Z') are coordinates of the sheared mesh. The mapping is a superposition of two 45° simple shears with a maximum shear angle of $\tan^{-1}(\sqrt{2}) = 54.7°$. This mesh is by no means a test for all types of possible mesh distortion. It does not, for example, address the case of non-parallelepiped elements or element volume variability. But, sheared meshes are useful for a number of types of earthquake problems, and are readily compatible with the layered model. A PML absorbing boundary is used for the bottom and side surfaces of the rectangular mesh and the bottom surface of the sheared mesh.

Since our PML implementation is limited to boundary surfaces that are normal to the Cartesian directions, it cannot be used on the sides of the sheared mesh. One way around this is to gradually reduce the shear of the mesh to zero at the boundary. We have taken an alternative approach by simply extending the mesh far enough that artificial reflections to not return during the simulation time.

A double-couple point source is located at the coordinates $(0, 0, 2\,\mathrm{km})$. The non-zero components of the moment tensor are

$$M_{xy} = M_{yx} = \frac{M_0 H(t)}{\sqrt{2\pi} S} e^{-0.5(t-4S)^2/S^2} \ , \tag{2.91}$$

where $M_0 = 10^{18}\,\mathrm{Nm}$, $S = 0.09\,\mathrm{s}$, and $H(t)$ is a step function. The half-width of the Gaussian source spectrum is 2.08 Hertz, corresponding to a Rayleigh wavelength of 17 grid points, and the source spectrum falls to 10% of its maximum at 3.8 Hz, or about 9 points per Rayleigh wavelength. The source is inserted into the wave simulation by normalizing the moment tensor by cell volume and adding it to the stress tensor after equation (2.64).

Particle velocity is recorded at three receiver locations at the surface: S1 $(-6\,\mathrm{km}, -8\,\mathrm{km}, 0)$, S2 $(6\,\mathrm{km}, -8\,\mathrm{km}, 0)$, and S3 $(6\,\mathrm{km}, 8\,\mathrm{km}, 0)$. At 2.08 Hertz, the source-receiver distance is approximately equal to 12 Rayleigh wavelengths in the layer, and 3.5 P wavelengths in the half-space, and at 3.8 Hertz, the distance is 21 Rayleigh wavelengths, and 6.3 P wavelengths. Due to symmetry, the analytical solutions for S1 and S3 are the same in cylindrical coordinates (with z axis through the source point). Receiver S2 is also the same with a sign change. For the numerical solution, though, the path from the source to each receiver has a different axis of propagation through the geometry of the sheared elements. The ray path to S1 is aligned with the long axis of the elements, while the path to S2 is aligned with the short axis. Receiver S3 has an intermediate alignment. In this way, anisotropy of

wave propagation due to element distortion can be tested.

Fig. 2.4 compares velocity time histories from both the rectangular- and sheared-mesh calculations against a reference solution computed by the frequency-wavenumber (FK) method of *Apsel and Luco* (1983). The reference solution can be viewed as semi-analytical, in that the FK method first forms the doubly Fourier transformed (from time and radial coordinate to frequency and wavenumber) solution analytically, then inverts the transformed solution to space-time coordinates by numerical quadrature. The radial and vertical components show good agreement for early arriving P-waves and late arriving Rayleigh waves, with amplitude misfits up to 1% of peak velocity, and arrival time misfits up to 0.01s. Multiply reflected P waves have greater misfits of up to 10% of peak velocity, and up to 0.04s in time. All of the SOM curves have roughly the same level of misfit to the FK solution, and a high level of agreement with each other. This indicates that mesh shearing is not the main source of error for P-waves and Rayleigh waves. Given the source bandwidth noted above, the level of waveform agreement achieved is consistent with expectations for a second-order accurate method, for which points-per-wavelength requirements in the range 10-15 are typically cited. The numerical errors take the form of non-physical dispersion, leading to phase velocity errors that (for second-order methods) increase monotonically with frequency (e.g., *Virieux*, 1986) so of course the actual points-per-wavelength requirement depends upon how much tolerance for phase errors one has in a given application.

The effects of mesh anisotropy are most apparent for S-wave arrivals in the transverse component. Interestingly, the sheared mesh curves consistently match FK better than does the rectangular mesh curve. For each arrival, S1 is the closest match, followed by S3, then S2, and finally the rectangular case. We have observed that the differences between the stations increases with hourglass viscosity β, and we attribute

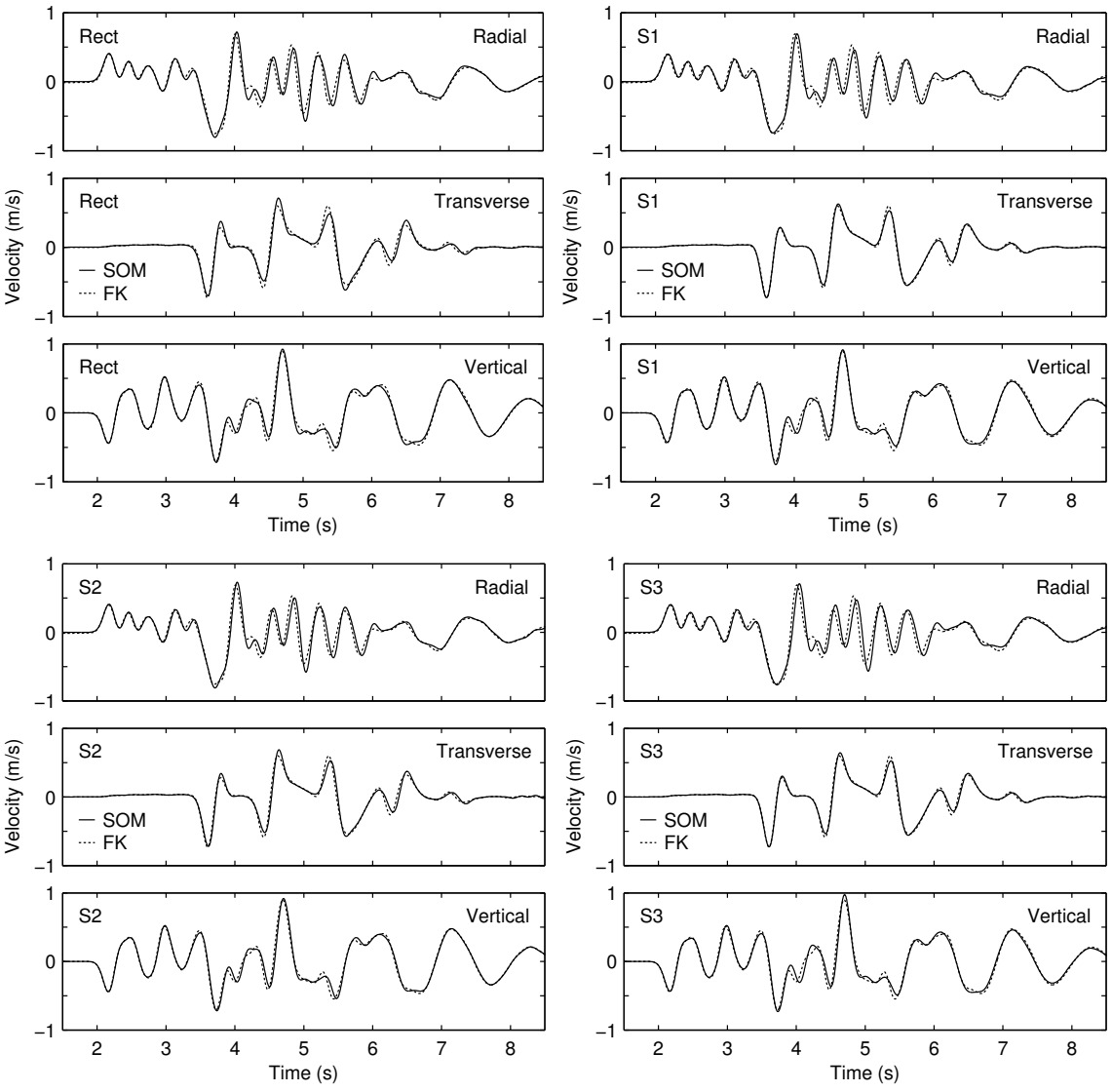

Figure 2.4: Simulated ground velocity compared to the reference solution calculated by frequency-wavenumber integration (FK). For comparison purposes, the polarity of S2 has been inverted to match stations S1 and S3.

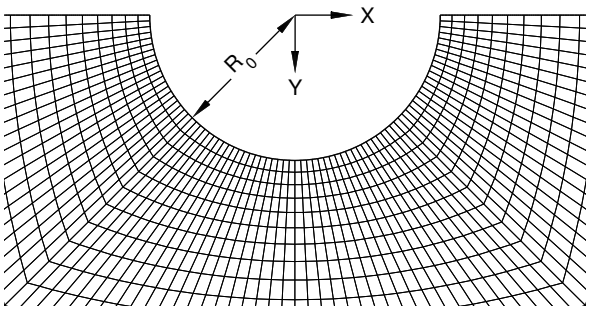

Figure 2.5: Close-in view of the mesh for a semi-circular canyon. The mesh extends outward to rectangular boundaries at $x = \pm 11R_0$ and $y = 11R_0$.

the higher mismatch for the rectangular mesh to hourglass oscillations, and imperfect removal of them by the hourglass correction scheme. Rectangular meshes are more susceptible to hourglass errors due to stronger coherence of the grid oscillation modes. Conversely, a greater diversity of nodal spacing and relative position lead to reduced hourglass mode coherence in the sheared mesh.

2.7 Semi-circular Canyon Test

Our second numerical test aims to verify the free surface boundary condition in the presence of topographic features. A vertically incident P wave on a semi-circular canyon presents a challenging test for numerical methods, as significant energy is converted to SV and Rayleigh waves, and relative amplification is highly variable in and around the canyon. The problem has been thoroughly studied using various types of boundary integral methods that we may use to verify the results of our present method.

The problem is set up with dimensionless parameters $\rho = 1$, $V_p = 2$, $V_s = 1$, $\gamma = 0$, and a semi-circular cavity of radius $R_0 = 1$ at the surface of a half space (Fig. 2.5). We accommodate the 2D geometry by constructing a mesh with a thickness

of one element in the z direction, and restricting motion to the $x - y$ plane. To facilitate planar boundary conditions, the outer boundaries are made rectangular. The dimensions of the mesh are $22R_0 \times 11R_0$. Elements gradually increase in size from $0.005R_0$ at the canyon to $0.07R_0$ at the boundaries. Computational savings are realized by calculating solutions for only the positive x half of the mesh, and enforcing a symmetry boundary condition along the y-axis. The symmetry boundary condition is also applied to the $x = 11R_0$ boundary, which is placed far enough from the canyon, that no horizontal motion is received during the simulation time. The vertically incident P wave is introduced as a boundary condition on displacement at the $y = 11R_0$ boundary. We mention that the time function of the source is a Ricker wavelet of $f_0 = 0.5$, though the exact form is not crucial for the method of analysis using spectral ratios. The computation is run for 6000 iterations with a time step of $\Delta t = 0.002$.

Analysis is preformed in terms of normalized frequency $f_0 = \omega R_0/2\pi V_s$. We consider the displacement amplitude at the surface for two frequencies: $f_0 = 0.25$, and $f_0 = 1.0$. The low frequency case, studied by *Wong* (1982), *Sánchez-Sesma et al.* (1985), and *Mossessian and Dravinski* (1987), corresponds to a P wavelength of four times the canyon width, and an S wavelength of twice the canyon width. The high frequency case, also studied by *Wong*, as well as *Kawase* (1988), and *Sánchez-Sesma and Campillo* (1991), corresponds to a P wavelength equal to the canyon width, and an S wavelength equal to half of the canyon width. Our results agree particularly well with the more recent studies (Fig. 2.6). For the high frequency case, the limiting factor for satisfactory agreement, is the spatial resolution of the P wave at the bottom bottom boundary where elements are largest. For $f_0 = 1.0$, the resolution is 28 points per wavelength at the bottom. We have seen noticeable differences in the surface response, when the resolution goes below 20 points per wavelength for the P wave

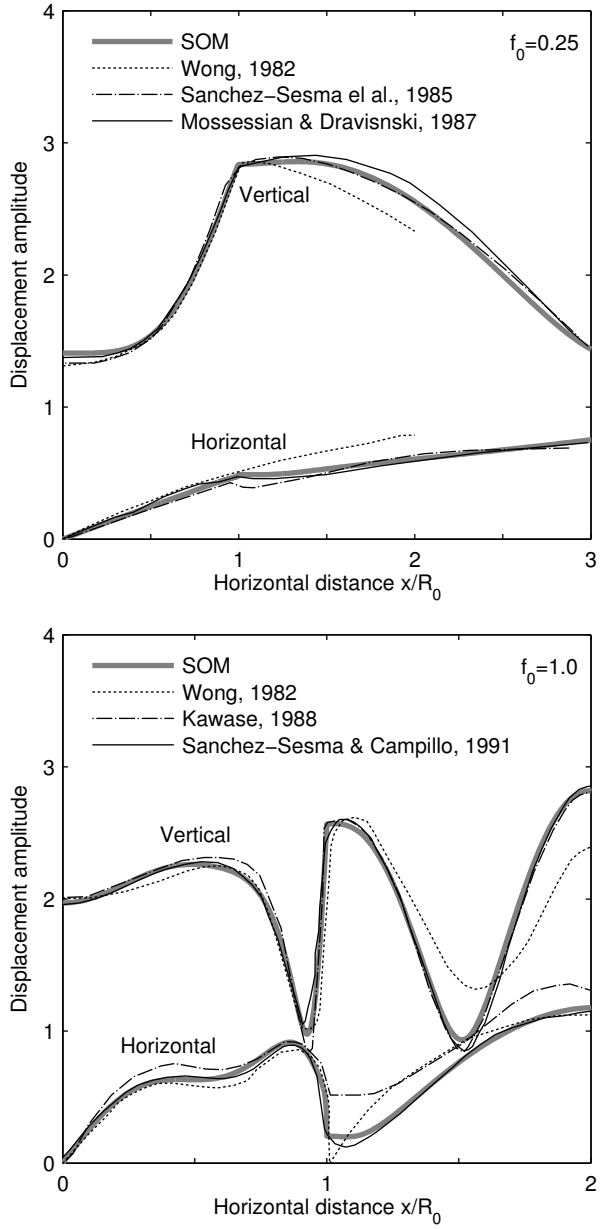

Figure 2.6: Surface displacement amplitude, at frequencies $f_0 = 0.25$ (top) and $f_0 = 1.0$ (bottom), as function of horizontal distance from the center of the canyon. Amplitudes are relative to the vertically incident P wave source. Results digitized from previous studies are shown for comparison.

source. The $f = 0.25$ signal is more than adequately resolved in the discretization, with at least 50 points per wavelength for all types of waves.

2.8 Parallelization

For large computational tasks, code parallelization is required for maximal utilization of modern computer hardware. A significant benefit of the structured mesh approach we have taken is that apportioning work among multiple processors is straightforward. We have implemented domain decomposition, where the mesh is subdivided and distributed across processors. During each time step, between equations (2.65) and (2.66) in the computational cycle, the nodal acceleration field at each sub-domain edges is transmitted to the neighboring sub-domain. In this way, the sub-domains are connected to form a single global computational domain.

To test parallel performance, we benchmarked our code on the TeraGrid IA64 cluster at the San Diego Supercomputer Center. A traditional strong scaling test measures runtime speedup for a fixed size problem as the number of processors increases. However, due to the distributed memory architecture of the cluster, it is impossible for a fixed size problem to fit in a single processor's memory and at the same time be a representative test for the communication and memory access patterns of a typical real-world, large-scale problem. For this reason, we prefer a weak scaling test in which the problem size is increased proportionally to the number of processors. Our weak scaling benchmark consists of a problem size of $128 \times 128 \times 128$ nodes per processor, run for 10 time steps. Timing begins after code initialization, since, though insignificant for a long run, initialization time might well influence a short-running benchmark test. The tests take about 30 seconds to run on TeraGrid. Ideal weak scaling occurs when runtime stays the same as the number of processors (and problem size) increases. The code achieves 84% efficiency on 512 processors.

Table 2.2: Weak scaling benchmark for the SDSC TeraGrid IA64 Cluster.

Processors	Normalized run-time	Efficiency
1	1.000	100%
8	1.176	85.1%
64	1.182	84.6%
512	1.188	84.2%

And, as shown in Table 2.2, the falloff in efficiency between 8 and 512 processors is very gradual, indicating the code likely will continue to scale well to higher numbers of processors.

2.9 Discussion and Conclusions

We have described a three-dimensional, arbitrary-order, support-operator method for viscoelastic wave simulation, and implemented it for the second order case. We have also implemented hourglass corrections, a free surface boundary condition, and a PML absorbing boundary condition. Our method addresses the problem of adding topography and non-planar boundaries to earthquake simulations. It has been tested against frequency-wavenumber solutions for wave propagation in a layer over half-space model (LOH.1), on a rectangular mesh as well as a mesh deformed by 54.7° simple shear. For wavelengths long enough to be propagated without significant numerical dispersion (e.g., represented by more than 10 points per wavelength) in the rectangular mesh, shearing the mesh introduces no measurable anisotropy. The points-per-wavelength requirement found here is typical of second-order methods. The use of a structured mesh permits very efficient parallel execution, and we have

been able to demonstrate scalability of the algorithm at greater than 80% efficiency on up to 512 processors.

The choice of using a logically rectangular mesh rather than an unstructured mesh has trade-offs. Unstructured meshes, used by some of the other methods cited in the introduction, are more adaptable to arbitrary problem geometry. They also allow for a high degree of local mesh refinement, which is particularly useful for modeling basins with a large range of material velocities, or for resolving small-scale detail of fault rupture dynamics. On the other hand, structured meshes, though significantly more restrictive, are more computationally efficient. If the differentiation operators are saved in memory, floating-point operations are reduced by a factor of six, nearly to the level of rectangular finite differences. This reduces actual run times by a factor of three. Structured meshes also greatly simplify the tasks of parallelization, mesh generation, and visualization of results. When the ratio of maximum to minimum wavespeed over the problem domain is not extreme, and the problem geometry can be adequately handled, structured meshes are quite advantageous. As an example, we have run wave propagation problems of 1.8 billion nodes, using 1920 processors and 250 GBytes of memory, that achieved a computation rate of 370 Gflop/s. That example used the SCEC Community Velocity Model (*Magistrale et al.*, 2000), with a ratio of maximum to minimum wavespeed of roughly 20.

Our method can be easily adapted to split nodes and nonlinear boundary conditions to simulate rupture. We presented rupture dynamics simulations on sheared meshes in *Ely et al.* (2005) that achieved accuracy comparable to rectangular mesh rupture dynamics methods. This will facilitate research on the dynamics of faults with realistic morphology, which, among other things, may produce strong nonlinear coupling between shear and normal stress perturbations. It also facilitates research on dynamics of dipping faults.

Because the method works explicitly with stress components (rather than a stiffness matrix, for example), it is easily generalized to calculate stresses from inelastic constitutive models (e.g. Coulomb plasticity, damage rheology, etc.), at the cost of saving the stress tensor components globally. This capability would be important in the study earthquake rupture dynamics, for example, as rupture-induced off-fault nonlinear deformation may be a significant contributor to the energy budget of earthquakes, and may also influence strong motion amplitudes.

We have formulated the SOM method for arbitrary order of accuracy, leaving the potential for developing a higher order algorithm. At higher than order two, however, it may not be possible to solve integral (2.20) algebraically. Instead, numerical quadrature would be required to calculate the operator weights. Either method of calculating the weights will be computationally costly, and the optimal scheme may be to store the weights rather that recalculate them on-the-fly. In a stored scheme, fourth-order operators, with a $4 \times 4 \times 4$ stencil, are eight times more costly than second-order operators in terms of storage and computations per time-step required to compute the spatial derivatives. When the entire numerical algorithm is considered, this translates to a five-fold increase in storage and computations for going to fourth order. The increased accuracy, though, reduces the points-per-wavelength requirement, permitting spatial and temporal resolution to be reduced. If the points-per-wavelength requirement can be reduced enough to surpass the break-even point in the cost trade-off, then the fourth-order method will be beneficial. Given that the memory usage goes like the third power of spatial resolution, and computational cost goes like the fourth power, we would need a factor of $\sqrt[3]{5}$ points-per-wavelength gain to break even on storage, and a factor of $\sqrt[4]{5}$ gain to break even on computations.

Acknowledgments

We are indebted to Prof. José Castillo for introducing us to the support operator method as well as providing valuable discussions. The quality of this manuscript had been greatly enhanced from careful reviews by David Oglesby and an anonymous reviewer. This work was supported by the National Science Foundation under grants ATM-0325033 and EAR-0122464, and by the Southern California Earthquake Center. SCEC is funded by NSF Cooperative Agreement EAR-0106924 and USGS Cooperative Agreement 02HQAG0008. The SCEC contribution number for this paper is 1089. This chapter, in full, is a reprint of the material as it appears in Geophysical Journal International, 2008, volume 172. The dissertation author is the primary investigator and author of this paper, with Steven Day and Jean-Bernard Minster as co-authors.

References

Aagaard, B. T. (1999), Finite-element simulations of earthquakes, *Technical Report EERL-99-03*, California Institute of Technology, Earthquake Engineering Research Laboratory, Pasadena, CA.

Apsel, R. J., and J. E. Luco (1983), On the Green's functions for a layered half-space. part II, *Bull. Seism. Soc. Am.*, *73*(4), 931–951.

Berenger, J.-P. (1994), A perfectly matched layer for the absorption of electromagnetic waves, *J. Comput. Phys.*, *114*(2), 185–200, doi:10.1006/jcph.1994.1159.

Berenger, J.-P. (1996), Three-dimensional perfectly matched layer for the absorption of electromagnetic waves, *J. Comput. Phys.*, *127*(2), 363–379, doi:doi:10.1006/jcph.1996.0181.

Cruz-Atienza, V. M. (2006), Rupture dynamique des failles non-planaires en différences finies, Ph.D. thesis, Université de Nice Sophia Antipolis.

Dalguer, L. A., and S. M. Day (2007), Staggered-grid split-node method for spontaneous rupture simulation, *J. Geophys. Res.*, *112*(B02302), doi:10.1029/2006JB004467.

Day, S. M., and C. R. Bradley (2001), Memory-efficient simulation of anelastic wave propagation, *Bull. Seism. Soc. Am.*, *91*(3), 520–531, doi:10.1785/0120000103.

Day, S. M., and J.-B. Minster (1984), Numerical simulation of attenuated wavefields using a Padé approximant method, *Geophys. J. Int.*, *78*(1), 105–118, doi:10.1111/j.1365-246X.1984.tb06474.x.

Day, S. M., L. A. Dalguer, N. Lapusta, and Y. Liu (2005), Comparison of finite difference and boundary integral solutions to three-dimensional spontaneous rupture, *J. Geophys. Res.*, *110*(B12307), doi:10.1029/2005JB003813.

Dumbser, M., and M. Kaŝer (2006), An arbitrary high-order discontinuous Galerkin method for elastic waves on unstructured meshes - ii. the three-dimensional isotropic case, *Geophys. J. Int.*, *167*(1), 319–336, doi:10.1111/j.1365-246X.2006.03120.x.

Ely, G. P., J.-B. Minster, and S. M. Day (2005), SORD: A new rupture dynamics modeling code, *Eos Trans. AGU*, *86*(52), Fall Meet. Suppl., Abstract S43A–1067.

Flanagan, D. P., and T. Belytschko (1981), A uniform strain hexahedron and quadrilateral with orthogonal hourglass control (in one-point integration of isoparametric finite element analysis), *Internat. J. Numer. Meths. Engrg.*, *17*(5), 679–706, doi:10.1002/nme.1620170504.

Goudreau, G. L., and J. O. Hallquist (1982), Recent developments in large-scale finite element lagrangian hydrocode technology, *Comput. Method. Appl. M.*, *33*(1-3), 725, doi:10.1016/0045-7825(82)90129-3.

Graves, R. W. (1996), Simulating seismic wave propagation in 3D elastic media using staggered-grid finite differences, *Bull. Seism. Soc. Am.*, *86*(4), 1091–1106.

Kase, Y., and S. M. Day (2006), Spontaneous rupture processes on a bending fault, *Geophys. Res. Lett.*, *33*(L10302), doi:10.1029/2006GL025870.

Kawase, H. (1988), Time-domain response of a semi-circular canyon for incident SV, P, and Rayleigh waves calculated by the discrete wavenumber boundary element method, *Bull. Seism. Soc. Am.*, *78*(4), 1415–1437.

Komatitsch, D., and J. Tromp (1999), Introduction to the spectral element method for three-dimensional seismic wave propagation, *Geophys. J. Int.*, *139*(3), 806–822, doi:10.1046/j.1365-246x.1999.00967.x.

Kosloff, D., and G. A. Frazier (1978), Treatment of hourglass patterns in low order finite element codes, *International Journal for Numerical and Analytical Methods in Geomechanics*, *2*(1), 57–72, doi:10.1002/nag.1610020105.

Levander, A. R. (1988), Fourth-order finite-difference P-SV seismograms, *Geophysics*, *53*(11), 1425–1436, doi:10.1190/1.1442422.

Ma, S., and P. Liu (2006), Modeling of the perfectly matched layer absorbing boundaries and intrinsic attenuation in explicit finite-element methods, *Bull. Seism. Soc. Am.*, *96*(5), 1779–1794, doi:10.1785/0120050219.

Ma, S., R. J. Archuleta, and M. T. Page (2007), Effects of large-scale surface topography on ground motions, as demonstrated by a study of the San Gabriel mountains, Los Angeles, California, *Bull. Seism. Soc. Am.*, *97*(6), 2066–2079, doi:10.1785/0120070040.

Magistrale, H., S. M. Day, R. W. Clayton, and R. W. Graves (2000), The SCEC southern California reference three-dimensional seismic velocity model version 2, *Bull. Seism. Soc. Am.*, *90*(6B), S65–76, doi:10.1785/0120000510.

Marcinkovich, C., and K. Olsen (2003), On the implementation of perfectly matched layers in a three-dimensional fourth-order velocity-stress finite difference scheme, *J. Geophys. Res.*, *108*(B5), 2276, doi:10.1029/2002JB002235.

Moczo, P., J. Robertson, and L. Eisner (2006), The finite-difference time-domain method for modeling of seismic wave propagation, in *Advances in Wave Propagation in Heterogeneous Earth*, *Advances in Geophysics*, vol. 48, edited by R.-S. Wu, V. Maupin, and R. Dmowska, pp. 421–516, Elsevier, Amsterdam, doi:10.1016/S0065-2687(06)48008-0.

Mossessian, T. K., and M. Dravinski (1987), Application of a hybrid method for scattering of P, SV, and Rayleigh waves by near-surface irregularities, *Bull. Seism. Soc. Am.*, *77*(5), 1784–1803.

Oglesby, D. D. (1999), Earthquake dynamics on dip-slip faults, Ph.D. thesis, University of California, Santa Barbara.

Oglesby, D. D., R. J. Archuleta, and S. B. Nielsen (2000), The three-dimensional dynamics of dipping faults, *Bull. Seism. Soc. Am.*, *90*(3), 616–628, doi:10.1785/0119990113.

Olsen, K. B., S. M. Day, J.-B. Minster, Y. Cui, A. Chourasia, M. Faerman, R. Moore, P. Maechling, and T. Jordan (2006), Strong shaking in Los Angeles expected from southern San Andreas earthquake, *Geophys. Res. Lett.*, *33*(L07305), doi:10.1029/2005GL025472.

Rojas, O., S. M. Day, J. E. Castillo, and L. A. Dalguer (2008), Modeling of rupture propagation using high-order mimetic finite differences, *Geophys. J. Int.*, *172*(2), 631–650, doi:10.1111/j.1365-246X.2007.03651.x.

Samarskii, A., V. Tishkin, A. Favorskii, and M. Shashkov (1981), Operational finite-difference schemes, *Diff. Eqns.*, *17*, 854–862.

Samarskii, A., V. Tishkin, A. Favorskii, and M. Shashkov (1982), Employment of the reference-operator method in the construction of finite difference analogs of tensor operations, *Diff. Eqns.*, *18*, 881–885.

Sánchez-Sesma, F. J., and M. Campillo (1991), Diffraction of P, SV, and rayleigh waves by topographic features: A boundary integral formulation, *Bull. Seism. Soc. Am.*, *81*(6), 2234–2253.

Sánchez-Sesma, F. J., M. A. Bravo, and I. Herrera (1985), Surface motion of topographical irregularities for incident P, SV, and Rayleigh waves, *Bull. Seism. Soc. Am.*, *75*(1), 263–269.

Shashkov, M. (1996), *Conservative Finite-Difference Methods on General Grids*, CRC Press, Boca Raton, FL.

Virieux, J. (1986), P-SV wave propagation in heterogeneous media: Velocity-stress finite-difference method, *Geophysics*, *51*(4), 889–901, doi:10.1190/1.1442147.

Wong, H. L. (1982), Effect of surface topography on the diffraction of P, SV, and Rayleigh waves, *Bull. Seism. Soc. Am.*, *72*(4), 1167–1183.

Appendix: Spatial Difference Operators

These are the 3D, second-order difference operators for gradient and divergence. Equations (2.92) through (2.97) are the exactly integrated versions, and equations (2.99) through (2.103) are the one-point quadrature versions.

Exactly integrated gradient, x component:

$$
\begin{aligned}
(D_xF)_{000} = \tfrac{1}{12}\Big\{ & \\
& F_{111}\Big[(Y_{100}-Y_{011})(Z_{110}-Z_{101})+Y_{011}(Z_{001}-Z_{010}) \\
& \quad +(Y_{010}-Y_{101})(Z_{011}-Z_{110})+Y_{101}(Z_{100}-Z_{001}) \\
& \quad +(Y_{001}-Y_{110})(Z_{101}-Z_{011})+Y_{110}(Z_{010}-Z_{100})\Big] \\
& +F_{100}\Big[(Y_{111}-Y_{000})(Z_{101}-Z_{110})+Y_{000}(Z_{010}-Z_{001}) \\
& \quad +(Y_{010}-Y_{101})(Z_{110}-Z_{000})+Y_{101}(Z_{001}-Z_{111}) \\
& \quad +(Y_{001}-Y_{110})(Z_{000}-Z_{101})+Y_{110}(Z_{111}-Z_{010})\Big] \\
& +F_{010}\Big[(Y_{111}-Y_{000})(Z_{110}-Z_{011})+Y_{000}(Z_{001}-Z_{100}) \\
& \quad +(Y_{100}-Y_{011})(Z_{000}-Z_{110})+Y_{011}(Z_{111}-Z_{001}) \\
& \quad +(Y_{001}-Y_{110})(Z_{011}-Z_{000})+Y_{110}(Z_{100}-Z_{111})\Big] \\
& +F_{001}\Big[(Y_{111}-Y_{000})(Z_{011}-Z_{101})+Y_{000}(Z_{100}-Z_{010}) \\
& \quad +(Y_{100}-Y_{011})(Z_{101}-Z_{000})+Y_{011}(Z_{010}-Z_{111}) \\
& \quad +(Y_{010}-Y_{101})(Z_{000}-Z_{011})+Y_{101}(Z_{111}-Z_{100})\Big] \\
& +F_{000}\Big[(Y_{011}-Y_{100})(Z_{010}-Z_{001})+Y_{100}(Z_{101}-Z_{110}) \\
& \quad +(Y_{101}-Y_{010})(Z_{001}-Z_{100})+Y_{010}(Z_{110}-Z_{011}) \\
& \quad +(Y_{110}-Y_{001})(Z_{100}-Z_{010})+Y_{001}(Z_{011}-Z_{101})\Big] \\
& +F_{011}\Big[(Y_{000}-Y_{111})(Z_{001}-Z_{010})+Y_{111}(Z_{110}-Z_{101}) \\
& \quad +(Y_{101}-Y_{010})(Z_{111}-Z_{001})+Y_{010}(Z_{000}-Z_{110}) \\
& \quad +(Y_{110}-Y_{001})(Z_{010}-Z_{111})+Y_{001}(Z_{101}-Z_{000})\Big] \\
& +F_{101}\Big[(Y_{000}-Y_{111})(Z_{100}-Z_{001})+Y_{111}(Z_{011}-Z_{110}) \\
& \quad +(Y_{011}-Y_{100})(Z_{001}-Z_{111})+Y_{100}(Z_{110}-Z_{000}) \\
& \quad +(Y_{110}-Y_{001})(Z_{111}-Z_{100})+Y_{001}(Z_{000}-Z_{011})\Big] \\
& +F_{110}\Big[(Y_{000}-Y_{111})(Z_{010}-Z_{100})+Y_{111}(Z_{101}-Z_{011}) \\
& \quad +(Y_{011}-Y_{100})(Z_{111}-Z_{010})+Y_{100}(Z_{000}-Z_{101}) \\
& \quad +(Y_{101}-Y_{010})(Z_{100}-Z_{111})+Y_{010}(Z_{011}-Z_{000})\Big]\Big\}
\end{aligned}
\tag{2.92}
$$

Exactly integrated divergence, x component:

$$
\begin{aligned}
(\mathcal{D}_x\mathbf{W})_{111} = \tfrac{1}{12}\Big\{ & \\
\mathbf{W}_{111}\Big[&(Y_{211}-Y_{122})(Z_{121}-Z_{112})+Y_{211}(Z_{221}-Z_{212}) \\
&+(Y_{121}-Y_{212})(Z_{112}-Z_{211})+Y_{121}(Z_{122}-Z_{221}) \\
&+(Y_{112}-Y_{221})(Z_{211}-Z_{121})+Y_{112}(Z_{212}-Z_{122})\Big] \\
+\mathbf{W}_{100}\Big[&(Y_{211}-Y_{100})(Z_{101}-Z_{110})+Y_{211}(Z_{201}-Z_{210}) \\
&+(Y_{101}-Y_{210})(Z_{110}-Z_{211})+Y_{101}(Z_{100}-Z_{201}) \\
&+(Y_{110}-Y_{201})(Z_{211}-Z_{101})+Y_{110}(Z_{210}-Z_{100})\Big] \\
+\mathbf{W}_{010}\Big[&(Y_{121}-Y_{010})(Z_{110}-Z_{011})+Y_{121}(Z_{120}-Z_{021}) \\
&+(Y_{110}-Y_{021})(Z_{011}-Z_{121})+Y_{110}(Z_{010}-Z_{120}) \\
&+(Y_{011}-Y_{120})(Z_{121}-Z_{110})+Y_{011}(Z_{021}-Z_{010})\Big] \\
+\mathbf{W}_{001}\Big[&(Y_{112}-Y_{001})(Z_{011}-Z_{101})+Y_{112}(Z_{012}-Z_{102}) \\
&+(Y_{011}-Y_{102})(Z_{101}-Z_{112})+Y_{011}(Z_{001}-Z_{012}) \\
&+(Y_{101}-Y_{012})(Z_{112}-Z_{011})+Y_{101}(Z_{102}-Z_{001})\Big] \\
+\mathbf{W}_{000}\Big[&(Y_{011}-Y_{100})(Z_{110}-Z_{101})+Y_{011}(Z_{010}-Z_{001}) \\
&+(Y_{101}-Y_{010})(Z_{011}-Z_{110})+Y_{101}(Z_{001}-Z_{100}) \\
&+(Y_{110}-Y_{001})(Z_{101}-Z_{011})+Y_{110}(Z_{100}-Z_{010})\Big] \\
+\mathbf{W}_{011}\Big[&(Y_{011}-Y_{122})(Z_{112}-Z_{121})+Y_{011}(Z_{012}-Z_{021}) \\
&+(Y_{121}-Y_{012})(Z_{011}-Z_{112})+Y_{121}(Z_{021}-Z_{122}) \\
&+(Y_{112}-Y_{021})(Z_{121}-Z_{011})+Y_{112}(Z_{122}-Z_{012})\Big] \\
+\mathbf{W}_{101}\Big[&(Y_{101}-Y_{212})(Z_{211}-Z_{112})+Y_{101}(Z_{201}-Z_{102}) \\
&+(Y_{112}-Y_{201})(Z_{101}-Z_{211})+Y_{112}(Z_{102}-Z_{212}) \\
&+(Y_{211}-Y_{102})(Z_{112}-Z_{101})+Y_{211}(Z_{212}-Z_{201})\Big] \\
+\mathbf{W}_{110}\Big[&(Y_{110}-Y_{221})(Z_{121}-Z_{211})+Y_{110}(Z_{120}-Z_{210}) \\
&+(Y_{211}-Y_{120})(Z_{110}-Z_{121})+Y_{211}(Z_{210}-Z_{221}) \\
&+(Y_{121}-Y_{210})(Z_{211}-Z_{110})+Y_{121}(Z_{221}-Z_{120})\Big]\Big\}
\end{aligned}
\tag{2.93}
$$

Exactly integrated gradient, y component:

$$
\begin{aligned}
(D_yF)_{000} = \tfrac{1}{12}\Big\{ & \\
& F_{111}\Big[(Z_{100}-Z_{011})(X_{110}-X_{101})+Z_{011}(X_{001}-X_{010}) \\
& \quad +(Z_{010}-Z_{101})(X_{011}-X_{110})+Z_{101}(X_{100}-X_{001}) \\
& \quad +(Z_{001}-Z_{110})(X_{101}-X_{011})+Z_{110}(X_{010}-X_{100})\Big] \\
& +F_{100}\Big[(Z_{111}-Z_{000})(X_{101}-X_{110})+Z_{000}(X_{010}-X_{001}) \\
& \quad +(Z_{010}-Z_{101})(X_{110}-X_{000})+Z_{101}(X_{001}-X_{111}) \\
& \quad +(Z_{001}-Z_{110})(X_{000}-X_{101})+Z_{110}(X_{111}-X_{010})\Big] \\
& +F_{010}\Big[(Z_{111}-Z_{000})(X_{110}-X_{011})+Z_{000}(X_{001}-X_{100}) \\
& \quad +(Z_{100}-Z_{011})(X_{000}-X_{110})+Z_{011}(X_{111}-X_{001}) \\
& \quad +(Z_{001}-Z_{110})(X_{011}-X_{000})+Z_{110}(X_{100}-X_{111})\Big] \\
& +F_{001}\Big[(Z_{111}-Z_{000})(X_{011}-X_{101})+Z_{000}(X_{100}-X_{010}) \\
& \quad +(Z_{100}-Z_{011})(X_{101}-X_{000})+Z_{011}(X_{010}-X_{111}) \\
& \quad +(Z_{010}-Z_{101})(X_{000}-X_{011})+Z_{101}(X_{111}-X_{100})\Big] \\
& +F_{000}\Big[(Z_{011}-Z_{100})(X_{010}-X_{001})+Z_{100}(X_{101}-X_{110}) \\
& \quad +(Z_{101}-Z_{010})(X_{001}-X_{100})+Z_{010}(X_{110}-X_{011}) \\
& \quad +(Z_{110}-Z_{001})(X_{100}-X_{010})+Z_{001}(X_{011}-X_{101})\Big] \\
& +F_{011}\Big[(Z_{000}-Z_{111})(X_{001}-X_{010})+Z_{111}(X_{110}-X_{101}) \\
& \quad +(Z_{101}-Z_{010})(X_{111}-X_{001})+Z_{010}(X_{000}-X_{110}) \\
& \quad +(Z_{110}-Z_{001})(X_{010}-X_{111})+Z_{001}(X_{101}-X_{000})\Big] \\
& +F_{101}\Big[(Z_{000}-Z_{111})(X_{100}-X_{001})+Z_{111}(X_{011}-X_{110}) \\
& \quad +(Z_{011}-Z_{100})(X_{001}-X_{111})+Z_{100}(X_{110}-X_{000}) \\
& \quad +(Z_{110}-Z_{001})(X_{111}-X_{100})+Z_{001}(X_{000}-X_{011})\Big] \\
& +F_{110}\Big[(Z_{000}-Z_{111})(X_{010}-X_{100})+Z_{111}(X_{101}-X_{011}) \\
& \quad +(Z_{011}-Z_{100})(X_{111}-X_{010})+Z_{100}(X_{000}-X_{101}) \\
& \quad +(Z_{101}-Z_{010})(X_{100}-X_{111})+Z_{010}(X_{011}-X_{000})\Big]\Big\}
\end{aligned}
\tag{2.94}
$$

Exactly integrated divergence, y component:

$$
\begin{aligned}
(\mathcal{D}_y\mathbf{W})_{111} = \tfrac{1}{12}\Big\{ & \\
& \mathbf{W}_{111}\Big[(Z_{211}-Z_{122})(X_{121}-X_{112})+Z_{211}(X_{221}-X_{212}) \\
& \quad +(Z_{121}-Z_{212})(X_{112}-X_{211})+Z_{121}(X_{122}-X_{221}) \\
& \quad +(Z_{112}-Z_{221})(X_{211}-X_{121})+Z_{112}(X_{212}-X_{122})\Big] \\
& +\mathbf{W}_{100}\Big[(Z_{211}-Z_{100})(X_{101}-X_{110})+Z_{211}(X_{201}-X_{210}) \\
& \quad +(Z_{101}-Z_{210})(X_{110}-X_{211})+Z_{101}(X_{100}-X_{201}) \\
& \quad +(Z_{110}-Z_{201})(X_{211}-X_{101})+Z_{110}(X_{210}-X_{100})\Big] \\
& +\mathbf{W}_{010}\Big[(Z_{121}-Z_{010})(X_{110}-X_{011})+Z_{121}(X_{120}-X_{021}) \\
& \quad +(Z_{110}-Z_{021})(X_{011}-X_{121})+Z_{110}(X_{010}-X_{120}) \\
& \quad +(Z_{011}-Z_{120})(X_{121}-X_{110})+Z_{011}(X_{021}-X_{010})\Big] \\
& +\mathbf{W}_{001}\Big[(Z_{112}-Z_{001})(X_{011}-X_{101})+Z_{112}(X_{012}-X_{102}) \\
& \quad +(Z_{011}-Z_{102})(X_{101}-X_{112})+Z_{011}(X_{001}-X_{012}) \\
& \quad +(Z_{101}-Z_{012})(X_{112}-X_{011})+Z_{101}(X_{102}-X_{001})\Big] \\
& +\mathbf{W}_{000}\Big[(Z_{011}-Z_{100})(X_{110}-X_{101})+Z_{011}(X_{010}-X_{001}) \\
& \quad +(Z_{101}-Z_{010})(X_{011}-X_{110})+Z_{101}(X_{001}-X_{100}) \\
& \quad +(Z_{110}-Z_{001})(X_{101}-X_{011})+Z_{110}(X_{100}-X_{010})\Big] \\
& +\mathbf{W}_{011}\Big[(Z_{011}-Z_{122})(X_{112}-X_{121})+Z_{011}(X_{012}-X_{021}) \\
& \quad +(Z_{121}-Z_{012})(X_{011}-X_{112})+Z_{121}(X_{021}-X_{122}) \\
& \quad +(Z_{112}-Z_{021})(X_{121}-X_{011})+Z_{112}(X_{122}-X_{012})\Big] \\
& +\mathbf{W}_{101}\Big[(Z_{101}-Z_{212})(X_{211}-X_{112})+Z_{101}(X_{201}-X_{102}) \\
& \quad +(Z_{112}-Z_{201})(X_{101}-X_{211})+Z_{112}(X_{102}-X_{212}) \\
& \quad +(Z_{211}-Z_{102})(X_{112}-X_{101})+Z_{211}(X_{212}-X_{201})\Big] \\
& +\mathbf{W}_{110}\Big[(Z_{110}-Z_{221})(X_{121}-X_{211})+Z_{110}(X_{120}-X_{210}) \\
& \quad +(Z_{211}-Z_{120})(X_{110}-X_{121})+Z_{211}(X_{210}-X_{221}) \\
& \quad +(Z_{121}-Z_{210})(X_{211}-X_{110})+Z_{121}(X_{221}-X_{120})\Big]\Big\}
\end{aligned}
\tag{2.95}
$$

Exactly integrated gradient, z component:

$$
\begin{aligned}
(D_zF)_{000} = \tfrac{1}{12}\Big\{ & \\
& F_{111}\Big[(X_{100}-X_{011})(Y_{110}-Y_{101})+X_{011}(Y_{001}-Y_{010}) \\
& \quad +(X_{010}-X_{101})(Y_{011}-Y_{110})+X_{101}(Y_{100}-Y_{001}) \\
& \quad +(X_{001}-X_{110})(Y_{101}-Y_{011})+X_{110}(Y_{010}-Y_{100})\Big] \\
& +F_{100}\Big[(X_{111}-X_{000})(Y_{101}-Y_{110})+X_{000}(Y_{010}-Y_{001}) \\
& \quad +(X_{010}-X_{101})(Y_{110}-Y_{000})+X_{101}(Y_{001}-Y_{111}) \\
& \quad +(X_{001}-X_{110})(Y_{000}-Y_{101})+X_{110}(Y_{111}-Y_{010})\Big] \\
& +F_{010}\Big[(X_{111}-X_{000})(Y_{110}-Y_{011})+X_{000}(Y_{001}-Y_{100}) \\
& \quad +(X_{100}-X_{011})(Y_{000}-Y_{110})+X_{011}(Y_{111}-Y_{001}) \\
& \quad +(X_{001}-X_{110})(Y_{011}-Y_{000})+X_{110}(Y_{100}-Y_{111})\Big] \\
& +F_{001}\Big[(X_{111}-X_{000})(Y_{011}-Y_{101})+X_{000}(Y_{100}-Y_{010}) \\
& \quad +(X_{100}-X_{011})(Y_{101}-Y_{000})+X_{011}(Y_{010}-Y_{111}) \\
& \quad +(X_{010}-X_{101})(Y_{000}-Y_{011})+X_{101}(Y_{111}-Y_{100})\Big] \\
& +F_{000}\Big[(X_{011}-X_{100})(Y_{010}-Y_{001})+X_{100}(Y_{101}-Y_{110}) \\
& \quad +(X_{101}-X_{010})(Y_{001}-Y_{100})+X_{010}(Y_{110}-Y_{011}) \\
& \quad +(X_{110}-X_{001})(Y_{100}-Y_{010})+X_{001}(Y_{011}-Y_{101})\Big] \\
& +F_{011}\Big[(X_{000}-X_{111})(Y_{001}-Y_{010})+X_{111}(Y_{110}-Y_{101}) \\
& \quad +(X_{101}-X_{010})(Y_{111}-Y_{001})+X_{010}(Y_{000}-Y_{110}) \\
& \quad +(X_{110}-X_{001})(Y_{010}-Y_{111})+X_{001}(Y_{101}-Y_{000})\Big] \\
& +F_{101}\Big[(X_{000}-X_{111})(Y_{100}-Y_{001})+X_{111}(Y_{011}-Y_{110}) \\
& \quad +(X_{011}-X_{100})(Y_{001}-Y_{111})+X_{100}(Y_{110}-Y_{000}) \\
& \quad +(X_{110}-X_{001})(Y_{111}-Y_{100})+X_{001}(Y_{000}-Y_{011})\Big] \\
& +F_{110}\Big[(X_{000}-X_{111})(Y_{010}-Y_{100})+X_{111}(Y_{101}-Y_{011}) \\
& \quad +(X_{011}-X_{100})(Y_{111}-Y_{010})+X_{100}(Y_{000}-Y_{101}) \\
& \quad +(X_{101}-X_{010})(Y_{100}-Y_{111})+X_{010}(Y_{011}-Y_{000})\Big]\Big\}
\end{aligned}
\tag{2.96}
$$

Exactly integrated divergence, z component:

$$
\begin{aligned}
(\mathcal{D}_z\mathbf{W})_{111} = \tfrac{1}{12}\Big\{ & \\
&\mathbf{W}_{111}\Big[(X_{211}-X_{122})(Y_{121}-Y_{112})+X_{211}(Y_{221}-Y_{212}) \\
&\quad +(X_{121}-X_{212})(Y_{112}-Y_{211})+X_{121}(Y_{122}-Y_{221}) \\
&\quad +(X_{112}-X_{221})(Y_{211}-Y_{121})+X_{112}(Y_{212}-Y_{122})\Big] \\
&+\mathbf{W}_{100}\Big[(X_{211}-X_{100})(Y_{101}-Y_{110})+X_{211}(Y_{201}-Y_{210}) \\
&\quad +(X_{101}-X_{210})(Y_{110}-Y_{211})+X_{101}(Y_{100}-Y_{201}) \\
&\quad +(X_{110}-X_{201})(Y_{211}-Y_{101})+X_{110}(Y_{210}-Y_{100})\Big] \\
&+\mathbf{W}_{010}\Big[(X_{121}-X_{010})(Y_{110}-Y_{011})+X_{121}(Y_{120}-Y_{021}) \\
&\quad +(X_{110}-X_{021})(Y_{011}-Y_{121})+X_{110}(Y_{010}-Y_{120}) \\
&\quad +(X_{011}-X_{120})(Y_{121}-Y_{110})+X_{011}(Y_{021}-Y_{010})\Big] \\
&+\mathbf{W}_{001}\Big[(X_{112}-X_{001})(Y_{011}-Y_{101})+X_{112}(Y_{012}-Y_{102}) \\
&\quad +(X_{011}-X_{102})(Y_{101}-Y_{112})+X_{011}(Y_{001}-Y_{012}) \\
&\quad +(X_{101}-X_{012})(Y_{112}-Y_{011})+X_{101}(Y_{102}-Y_{001})\Big] \\
&+\mathbf{W}_{000}\Big[(X_{011}-X_{100})(Y_{110}-Y_{101})+X_{011}(Y_{010}-Y_{001}) \\
&\quad +(X_{101}-X_{010})(Y_{011}-Y_{110})+X_{101}(Y_{001}-Y_{100}) \\
&\quad +(X_{110}-X_{001})(Y_{101}-Y_{011})+X_{110}(Y_{100}-Y_{010})\Big] \\
&+\mathbf{W}_{011}\Big[(X_{011}-X_{122})(Y_{112}-Y_{121})+X_{011}(Y_{012}-Y_{021}) \\
&\quad +(X_{121}-X_{012})(Y_{011}-Y_{112})+X_{121}(Y_{021}-Y_{122}) \\
&\quad +(X_{112}-X_{021})(Y_{121}-Y_{011})+X_{112}(Y_{122}-Y_{012})\Big] \\
&+\mathbf{W}_{101}\Big[(X_{101}-X_{212})(Y_{211}-Y_{112})+X_{101}(Y_{201}-Y_{102}) \\
&\quad +(X_{112}-X_{201})(Y_{101}-Y_{211})+X_{112}(Y_{102}-Y_{212}) \\
&\quad +(X_{211}-X_{102})(Y_{112}-Y_{101})+X_{211}(Y_{212}-Y_{201})\Big] \\
&+\mathbf{W}_{110}\Big[(X_{110}-X_{221})(Y_{121}-Y_{211})+X_{110}(Y_{120}-Y_{210}) \\
&\quad +(X_{211}-X_{120})(Y_{110}-Y_{121})+X_{211}(Y_{210}-Y_{221}) \\
&\quad +(X_{121}-X_{210})(Y_{211}-Y_{110})+X_{121}(Y_{221}-Y_{120})\Big]\Big\}
\end{aligned}
\tag{2.97}
$$

One-point quadrature gradient, x component:

$$
\begin{aligned}
(D_xF)_{000} = \tfrac{1}{16}\Big\{ & \\
& (F_{111}-F_{000})\Big[(Y_{100}-Y_{011})(Z_{010}-Z_{101}-Z_{001}+Z_{110}) \\
& \qquad +(Y_{010}-Y_{101})(Z_{001}-Z_{110}-Z_{100}+Z_{011}) \\
& \qquad +(Y_{001}-Y_{110})(Z_{100}-Z_{011}-Z_{010}+Z_{101})\Big] \\
& +(F_{100}-F_{011})\Big[(Y_{111}-Y_{000})(Z_{001}-Z_{110}-Z_{010}+Z_{101}) \\
& \qquad +(Y_{010}-Y_{101})(Z_{111}-Z_{000}-Z_{001}+Z_{110}) \\
& \qquad +(Y_{001}-Y_{110})(Z_{010}-Z_{101}-Z_{111}+Z_{000})\Big] \\
& +(F_{010}-F_{101})\Big[(Y_{111}-Y_{000})(Z_{100}-Z_{011}-Z_{001}+Z_{110}) \\
& \qquad +(Y_{001}-Y_{110})(Z_{111}-Z_{000}-Z_{100}+Z_{011}) \\
& \qquad +(Y_{100}-Y_{011})(Z_{001}-Z_{110}-Z_{111}+Z_{000})\Big] \\
& +(F_{001}-F_{110})\Big[(Y_{111}-Y_{000})(Z_{010}-Z_{101}-Z_{100}+Z_{011}) \\
& \qquad +(Y_{100}-Y_{011})(Z_{111}-Z_{000}-Z_{010}+Z_{101}) \\
& \qquad +(Y_{010}-Y_{101})(Z_{100}-Z_{011}-Z_{111}+Z_{000})\Big]\Big\}
\end{aligned}
\tag{2.98}
$$

One-point quadrature divergence, x component:

$$
\begin{aligned}
(\mathcal{D}_x\mathbf{W})_{111} = \tfrac{1}{16}\Big\{ & \\
& \mathbf{W}_{111}\Big[(Y_{211}-Y_{122})(Z_{121}-Z_{212}-Z_{112}+Z_{221}) \\
& \quad +(Y_{121}-Y_{212})(Z_{112}-Z_{221}-Z_{211}+Z_{122}) \\
& \quad +(Y_{112}-Y_{221})(Z_{211}-Z_{122}-Z_{121}+Z_{212})\Big] \\
& +\mathbf{W}_{100}\Big[(Y_{211}-Y_{100})(Z_{101}-Z_{210}-Z_{110}+Z_{201}) \\
& \quad +(Y_{101}-Y_{210})(Z_{110}-Z_{201}-Z_{211}+Z_{100}) \\
& \quad +(Y_{110}-Y_{201})(Z_{211}-Z_{100}-Z_{101}+Z_{210})\Big] \\
& +\mathbf{W}_{010}\Big[(Y_{121}-Y_{010})(Z_{110}-Z_{021}-Z_{011}+Z_{120}) \\
& \quad +(Y_{110}-Y_{021})(Z_{011}-Z_{120}-Z_{121}+Z_{010}) \\
& \quad +(Y_{011}-Y_{120})(Z_{121}-Z_{010}-Z_{110}+Z_{021})\Big] \\
& +\mathbf{W}_{001}\Big[(Y_{112}-Y_{001})(Z_{011}-Z_{102}-Z_{101}+Z_{012}) \\
& \quad +(Y_{011}-Y_{102})(Z_{101}-Z_{012}-Z_{112}+Z_{001}) \\
& \quad +(Y_{101}-Y_{012})(Z_{112}-Z_{001}-Z_{011}+Z_{102})\Big] \\
& +\mathbf{W}_{000}\Big[(Y_{011}-Y_{100})(Z_{010}-Z_{101}-Z_{001}+Z_{110}) \\
& \quad +(Y_{101}-Y_{010})(Z_{001}-Z_{110}-Z_{100}+Z_{011}) \\
& \quad +(Y_{110}-Y_{001})(Z_{100}-Z_{011}-Z_{010}+Z_{101})\Big] \\
& +\mathbf{W}_{011}\Big[(Y_{011}-Y_{122})(Z_{012}-Z_{121}-Z_{021}+Z_{112}) \\
& \quad +(Y_{121}-Y_{012})(Z_{021}-Z_{112}-Z_{122}+Z_{011}) \\
& \quad +(Y_{112}-Y_{021})(Z_{122}-Z_{011}-Z_{012}+Z_{121})\Big] \\
& +\mathbf{W}_{101}\Big[(Y_{101}-Y_{212})(Z_{201}-Z_{112}-Z_{102}+Z_{211}) \\
& \quad +(Y_{112}-Y_{201})(Z_{102}-Z_{211}-Z_{212}+Z_{101}) \\
& \quad +(Y_{211}-Y_{102})(Z_{212}-Z_{101}-Z_{201}+Z_{112})\Big] \\
& +\mathbf{W}_{110}\Big[(Y_{110}-Y_{221})(Z_{120}-Z_{211}-Z_{210}+Z_{121}) \\
& \quad +(Y_{211}-Y_{120})(Z_{210}-Z_{121}-Z_{221}+Z_{110}) \\
& \quad +(Y_{121}-Y_{210})(Z_{221}-Z_{110}-Z_{120}+Z_{211})\Big]\Big\}
\end{aligned}
\tag{2.99}
$$

One-point quadrature gradient, y component:

$$
\begin{aligned}
(D_yF)_{000} = \tfrac{1}{16}\Big\{ & \\
&(F_{111}-F_{000})\Big[(Z_{100}-Z_{011})(X_{010}-X_{101}-X_{001}+X_{110}) \\
&\qquad +(Z_{010}-Z_{101})(X_{001}-X_{110}-X_{100}+X_{011}) \\
&\qquad +(Z_{001}-Z_{110})(X_{100}-X_{011}-X_{010}+X_{101})\Big] \\
&+(F_{100}-F_{011})\Big[(Z_{111}-Z_{000})(X_{001}-X_{110}-X_{010}+X_{101}) \\
&\qquad +(Z_{010}-Z_{101})(X_{111}-X_{000}-X_{001}+X_{110}) \\
&\qquad +(Z_{001}-Z_{110})(X_{010}-X_{101}-X_{111}+X_{000})\Big] \\
&+(F_{010}-F_{101})\Big[(Z_{111}-Z_{000})(X_{100}-X_{011}-X_{001}+X_{110}) \\
&\qquad +(Z_{001}-Z_{110})(X_{111}-X_{000}-X_{100}+X_{011}) \\
&\qquad +(Z_{100}-Z_{011})(X_{001}-X_{110}-X_{111}+X_{000})\Big] \\
&+(F_{001}-F_{110})\Big[(Z_{111}-Z_{000})(X_{010}-X_{101}-X_{100}+X_{011}) \\
&\qquad +(Z_{100}-Z_{011})(X_{111}-X_{000}-X_{010}+X_{101}) \\
&\qquad +(Z_{010}-Z_{101})(X_{100}-X_{011}-X_{111}+X_{000})\Big]\Big\}
\end{aligned}
\tag{2.100}
$$

One-point quadrature divergence, y component:

$$
\begin{aligned}
(\mathcal{D}_y\mathbf{W})_{111} = \tfrac{1}{16}\Big\{ & \\
& \mathbf{W}_{111}\Big[(Z_{211}-Z_{122})(X_{121}-X_{212}-X_{112}+X_{221}) \\
& \quad +(Z_{121}-Z_{212})(X_{112}-X_{221}-X_{211}+X_{122}) \\
& \quad +(Z_{112}-Z_{221})(X_{211}-X_{122}-X_{121}+X_{212})\Big] \\
& +\mathbf{W}_{100}\Big[(Z_{211}-Z_{100})(X_{101}-X_{210}-X_{110}+X_{201}) \\
& \quad +(Z_{101}-Z_{210})(X_{110}-X_{201}-X_{211}+X_{100}) \\
& \quad +(Z_{110}-Z_{201})(X_{211}-X_{100}-X_{101}+X_{210})\Big] \\
& +\mathbf{W}_{010}\Big[(Z_{121}-Z_{010})(X_{110}-X_{021}-X_{011}+X_{120}) \\
& \quad +(Z_{110}-Z_{021})(X_{011}-X_{120}-X_{121}+X_{010}) \\
& \quad +(Z_{011}-Z_{120})(X_{121}-X_{010}-X_{110}+X_{021})\Big] \\
& +\mathbf{W}_{001}\Big[(Z_{112}-Z_{001})(X_{011}-X_{102}-X_{101}+X_{012}) \\
& \quad +(Z_{011}-Z_{102})(X_{101}-X_{012}-X_{112}+X_{001}) \\
& \quad +(Z_{101}-Z_{012})(X_{112}-X_{001}-X_{011}+X_{102})\Big] \\
& +\mathbf{W}_{000}\Big[(Z_{011}-Z_{100})(X_{010}-X_{101}-X_{001}+X_{110}) \\
& \quad +(Z_{101}-Z_{010})(X_{001}-X_{110}-X_{100}+X_{011}) \\
& \quad +(Z_{110}-Z_{001})(X_{100}-X_{011}-X_{010}+X_{101})\Big] \\
& +\mathbf{W}_{011}\Big[(Z_{011}-Z_{122})(X_{012}-X_{121}-X_{021}+X_{112}) \\
& \quad +(Z_{121}-Z_{012})(X_{021}-X_{112}-X_{122}+X_{011}) \\
& \quad +(Z_{112}-Z_{021})(X_{122}-X_{011}-X_{012}+X_{121})\Big] \\
& +\mathbf{W}_{101}\Big[(Z_{101}-Z_{212})(X_{201}-X_{112}-X_{102}+X_{211}) \\
& \quad +(Z_{112}-Z_{201})(X_{102}-X_{211}-X_{212}+X_{101}) \\
& \quad +(Z_{211}-Z_{102})(X_{212}-X_{101}-X_{201}+X_{112})\Big] \\
& +\mathbf{W}_{110}\Big[(Z_{110}-Z_{221})(X_{120}-X_{211}-X_{210}+X_{121}) \\
& \quad +(Z_{211}-Z_{120})(X_{210}-X_{121}-X_{221}+X_{110}) \\
& \quad +(Z_{121}-Z_{210})(X_{221}-X_{110}-X_{120}+X_{211})\Big]\Big\}
\end{aligned}
\tag{2.101}
$$

One-point quadrature gradient, z component:

$$
\begin{aligned}
(D_z F)_{000} = \tfrac{1}{16}\Big\{ & \\
& (F_{111} - F_{000})\Big[(X_{100} - X_{011})(Y_{010} - Y_{101} - Y_{001} + Y_{110}) \\
& \qquad +(X_{010} - X_{101})(Y_{001} - Y_{110} - Y_{100} + Y_{011}) \\
& \qquad +(X_{001} - X_{110})(Y_{100} - Y_{011} - Y_{010} + Y_{101})\Big] \\
& +(F_{100} - F_{011})\Big[(X_{111} - X_{000})(Y_{001} - Y_{110} - Y_{010} + Y_{101}) \\
& \qquad +(X_{010} - X_{101})(Y_{111} - Y_{000} - Y_{001} + Y_{110}) \\
& \qquad +(X_{001} - X_{110})(Y_{010} - Y_{101} - Y_{111} + Y_{000})\Big] \\
& +(F_{010} - F_{101})\Big[(X_{111} - X_{000})(Y_{100} - Y_{011} - Y_{001} + Y_{110}) \\
& \qquad +(X_{001} - X_{110})(Y_{111} - Y_{000} - Y_{100} + Y_{011}) \\
& \qquad +(X_{100} - X_{011})(Y_{001} - Y_{110} - Y_{111} + Y_{000})\Big] \\
& +(F_{001} - F_{110})\Big[(X_{111} - X_{000})(Y_{010} - Y_{101} - Y_{100} + Y_{011}) \\
& \qquad +(X_{100} - X_{011})(Y_{111} - Y_{000} - Y_{010} + Y_{101}) \\
& \qquad +(X_{010} - X_{101})(Y_{100} - Y_{011} - Y_{111} + Y_{000})\Big]\Big\}
\end{aligned}
\tag{2.102}
$$

One-point quadrature divergence, z component:

$$
\begin{aligned}
(\mathcal{D}_z\mathbf{W})_{111} = \tfrac{1}{16}\Big\{ & \\
& \mathbf{W}_{111}\Big[(X_{211}-X_{122})(Y_{121}-Y_{212}-Y_{112}+Y_{221}) \\
& \quad +(X_{121}-X_{212})(Y_{112}-Y_{221}-Y_{211}+Y_{122}) \\
& \quad +(X_{112}-X_{221})(Y_{211}-Y_{122}-Y_{121}+Y_{212})\Big] \\
& +\mathbf{W}_{100}\Big[(X_{211}-X_{100})(Y_{101}-Y_{210}-Y_{110}+Y_{201}) \\
& \quad +(X_{101}-X_{210})(Y_{110}-Y_{201}-Y_{211}+Y_{100}) \\
& \quad +(X_{110}-X_{201})(Y_{211}-Y_{100}-Y_{101}+Y_{210})\Big] \\
& +\mathbf{W}_{010}\Big[(X_{121}-X_{010})(Y_{110}-Y_{021}-Y_{011}+Y_{120}) \\
& \quad +(X_{110}-X_{021})(Y_{011}-Y_{120}-Y_{121}+Y_{010}) \\
& \quad +(X_{011}-X_{120})(Y_{121}-Y_{010}-Y_{110}+Y_{021})\Big] \\
& +\mathbf{W}_{001}\Big[(X_{112}-X_{001})(Y_{011}-Y_{102}-Y_{101}+Y_{012}) \\
& \quad +(X_{011}-X_{102})(Y_{101}-Y_{012}-Y_{112}+Y_{001}) \\
& \quad +(X_{101}-X_{012})(Y_{112}-Y_{001}-Y_{011}+Y_{102})\Big] \\
& +\mathbf{W}_{000}\Big[(X_{011}-X_{100})(Y_{010}-Y_{101}-Y_{001}+Y_{110}) \\
& \quad +(X_{101}-X_{010})(Y_{001}-Y_{110}-Y_{100}+Y_{011}) \\
& \quad +(X_{110}-X_{001})(Y_{100}-Y_{011}-Y_{010}+Y_{101})\Big] \\
& +\mathbf{W}_{011}\Big[(X_{011}-X_{122})(Y_{012}-Y_{121}-Y_{021}+Y_{112}) \\
& \quad +(X_{121}-X_{012})(Y_{021}-Y_{112}-Y_{122}+Y_{011}) \\
& \quad +(X_{112}-X_{021})(Y_{122}-Y_{011}-Y_{012}+Y_{121})\Big] \\
& +\mathbf{W}_{101}\Big[(X_{101}-X_{212})(Y_{201}-Y_{112}-Y_{102}+Y_{211}) \\
& \quad +(X_{112}-X_{201})(Y_{102}-Y_{211}-Y_{212}+Y_{101}) \\
& \quad +(X_{211}-X_{102})(Y_{212}-Y_{101}-Y_{201}+Y_{112})\Big] \\
& +\mathbf{W}_{110}\Big[(X_{110}-X_{221})(Y_{120}-Y_{211}-Y_{210}+Y_{121}) \\
& \quad +(X_{211}-X_{120})(Y_{210}-Y_{121}-Y_{221}+Y_{110}) \\
& \quad +(X_{121}-X_{210})(Y_{221}-Y_{110}-Y_{120}+Y_{211})\Big]\Big\}
\end{aligned}
\tag{2.103}
$$

Chapter 3

A Support-Operator Method for 3D Rupture Dynamics

Abstract

We present a numerical method to simulate spontaneous shear crack propagation within a heterogeneous, three-dimensional, viscoelastic medium. Wave motions are computed on a logically rectangular hexahedral mesh, using the generalized finite difference method of Support Operators (SOM). This approach enables modeling of non-planar surfaces and non-planar ruptures. Our implementation, the Support Operator Rupture Dynamics code (SORD), is highly scalable, enabling large scale, multi-processors calculations. The fault surface is modeled by coupled double nodes, where rupture occurs as dictated by the local stress conditions and a frictional failure law. The method successfully performs test problems developed for the Southern California Earthquake Center (SCEC)/U.S. Geological Survey (USGS) dynamic earthquake rupture code validation exercise, showing good agreement with semi-analytical boundary integral method results. We undertake further dynamic rupture tests to quantify numerical errors introduced by shear deformations to the hexahedral mesh.

We generate a family of meshes distorted by simple shearing, in the along-strike direction, up to a maximum of 73-degrees. For SCEC/USGS validation problem number 3, grid-induced errors increase with mesh shear angle, with the logarithm of error approximately proportional to angle over the range tested. At 73-degrees, RMS misfits are about 10% for peak slip rate, and 0.5% for both rupture time and total slip, indicating that the method (which up to now we have applied mainly to near-vertical strike-slip faulting) is also capable of handling geometries appropriate to low-angle surface-rupturing thrust earthquakes. Additionally, we demonstrate non-planar rupture effects, by modifying the test geometry to include, respectively, cylindrical curvature and sharp kinks.

3.1 Introduction

The simulation of earthquake rupture dynamics on non-planar faults embedded in a three dimensional, heterogeneous medium has been addressed by a number of methods. *Aagaard* (1999) and *Oglesby et al.* (2000) used finite element methods; *Festa* (2004) and *Vilotte et al.* (2005) used spectral element methods; *Zhang et al.* (2006), *Kase and Day* (2006) and *Cruz-Atienza et al.* (2007) used modified finite difference schemes; and *Benjemaa et al.* (2007) used a finite volume technique. The high spatial sampling necessary to adequately resolve the rupture process presents a substantial computational challenge to most methods. Unstructured meshes with adaptive local refinement is a strategy employed by some. The limitations of adaptive meshing are that grid generation is more cumbersome, and algorithms may be less efficient and more difficult to adapt for parallel computation. A more 'brute force' approach is to densely sample the model everywhere with a mesh of regular structure, and to exploit that structure to create highly efficient and parallelizable algorithms. We have adopted the latter approach, using the method of Support Operators, a

generalized finite difference method introduced by *Samarskii et al.* (1981, 1982) and *Shashkov* (1996). The Support Operator method was applied to three-dimentional elastic wave propagation by *Ely et al.* (2008), and we extend that application here to including modeling of spontaneous rupture.

This paper begins by first reviewing the formulation for the wave propagation equations and the spontaneous rupture boundary condition. We then lay out the discretization scheme and algorithm for computing numerical solutions. Next, we verify the method against semi-analytical solutions computed with the boundary integral method. We then quantify errors induced due to deformation of the mesh by simple shearing. Finally, we study the effects of curved and kinked fault geometry on spontaneous rupture.

3.2 Theoretical Formulation

The faulting model is embedded within a three-dimensional, heterogeneous, viscoelastic solid. The linearized equations of motion for the medium are

$$g_{ij} = \partial_j(u_i + \gamma v_i) \ , \tag{3.1}$$

$$\sigma_{ij} = \lambda \, \delta_{ij} \, g_{kk} + \mu(g_{ij} + g_{ji}) \ , \tag{3.2}$$

$$a_i = \frac{1}{\rho} \, \partial_j \sigma_{ij} \ , \tag{3.3}$$

$$\dot{v}_i = a_i \ , \tag{3.4}$$

$$\dot{u}_i = v_i \ , \tag{3.5}$$

where $\boldsymbol{\sigma}$ is the stress tensor, $\mathbf{u}$ and $\mathbf{v}$ are displacement and velocity vectors, ρ is density, λ and μ are elastic moduli, and γ is viscosity. All variables are functions of

position $\mathbf{x}$, while $\boldsymbol{\sigma}$, $\mathbf{u}$, and $\mathbf{v}$ are time dependent as well.

Two types of boundary condition are employed over the external surface of the model: a free surface condition, where the normal component of stress is zero ($\boldsymbol{\sigma} \cdot \hat{\mathbf{n}} = 0$), and a non-reflective absorbing boundary. The absorbing boundary condition is a variation of the Perfectly Matched Layer (PML) method, introduced by *Berenger* (1994, 1996), and adapted to support operators by *Ely et al.* (2008).

Following *Day et al.* (2005), faulting is modeled as an internal surface Σ across which discontinuity of displacement may occur. The unit normal $\hat{\mathbf{n}}(\mathbf{x})$ points from the Σ^- side to the Σ^+ side of the surface Σ. The limiting values of displacement $\mathbf{u}^-$ and $\mathbf{u}^+$, at the surface Σ are

$$\mathbf{u}^{\pm}(\mathbf{x}, t) = \lim_{\epsilon \to 0} \mathbf{u}(\mathbf{x} \pm \epsilon \hat{\mathbf{n}}(\mathbf{x}), t) \ . \tag{3.6}$$

The two sides are permitted to separate, but not to interpenetrate, so the relative normal displacement must be positive,

$$\hat{\mathbf{n}} \cdot (\mathbf{u}^+ - \mathbf{u}^-) \geq 0 \ . \tag{3.7}$$

The tangential discontinuity of displacement is denoted 'slip' and given by

$$\mathbf{s} = (\mathbf{I} - \hat{\mathbf{n}}\hat{\mathbf{n}}) \cdot (\mathbf{u}^+ - \mathbf{u}^-) \ . \tag{3.8}$$

Stress is continuous across Σ, and when dotted with the unit normal, is resolved onto Σ to give traction

$$\boldsymbol{\tau} = \boldsymbol{\sigma} \cdot \hat{\mathbf{n}} \ . \tag{3.9}$$

Traction is the surface density of force acting on Σ^- due to Σ^+. The shear component

of traction is

$$\boldsymbol{\tau}_s = (\mathbf{I} - \hat{\mathbf{n}}\hat{\mathbf{n}}) \cdot \boldsymbol{\tau} \ . \tag{3.10}$$

The rupture boundary condition is formulated by specifying a frictional strength τ_c that is a bound on the magnitude of shear traction

$$|\boldsymbol{\tau}_s| \leq \tau_c \ . \tag{3.11}$$

When shear traction is less than the frictional strength, slip does not occur and Σ is invisible to elastic waves. Slip only occurs when shear traction reaches the level of the frictional strength. Slip velocity opposes the direction of the shear traction according to the relation

$$\tau_c \dot{\mathbf{s}} = |\dot{\mathbf{s}}| \boldsymbol{\tau}_s \ . \tag{3.12}$$

This specifies that direction of slip velocity is antiparallel to traction, since the relative slip velocity of Σ^- has the opposite sign of $\dot{\mathbf{s}}$.

For the friction law, we use the slip-weakening model, that evolves as a function of the slip path length. The path length is found by the integral

$$\ell = \int_0^t |\dot{\mathbf{s}}| dt \ . \tag{3.13}$$

The frictional strength is equal to the product of the normal traction and a coefficient of friction,

$$\tau_c = -\tau_n \mu_f(\ell) \ . \tag{3.14}$$

$$\tau_n = \hat{\mathbf{n}} \cdot \boldsymbol{\sigma} \cdot \hat{\mathbf{n}} \ , \tag{3.15}$$

and the coefficient of friction is a function of the slip path length,

$$\mu_f(\ell) = \begin{cases} \mu_s - (\mu_s - \mu_d)\ell/d_0 & \ell \leq d_0 \\ \mu_d & \ell > d_0 \ , \end{cases} \tag{3.16}$$

where μ_s and μ_d are coefficients of static and dynamic friction, and d_0 is the critical slip-weakening distance. Fault opening ensures that normal stress is always negative (never tensional), and therefor the sign of τ_c in (3.14) is always positive. This model accounts for potentially repeated episodes of rupture initiation, and subsequent arrest of sliding, a well as repeated episodes of fault opening, and subsequent fault closing. The methodology can also accommodate more complex friction laws (such as those based on rate- and state-dependent formulations) where there is stationary contact only at zero shear traction, in which case inequality (3.11) becomes an equality and the distinction between τ and τ_c disappears.

Traction is referenced to an initial state $\boldsymbol{\tau}_0$. This can either be resolved from an initial stress field $\boldsymbol{\sigma}_0$, or specified directly in terms of a local coordinate system on the fault, such as the strike and dip coordinate system traditionally used for earthquake problems (Fig. 3.1). The former is useful for specifying tractions that result, for example, from a regional tectonic load. The latter is most natural when initial traction is determined by local frictional conditions on the fault. In general they can be combined as

$$\boldsymbol{\tau}_0 = \boldsymbol{\sigma}_0 \cdot \hat{\mathbf{n}} + \tau_n \hat{\mathbf{n}} + \tau_{s_1} \hat{\mathbf{s}}_1 + \tau_{s_2} \hat{\mathbf{s}}_2 \ , \tag{3.17}$$

where $\hat{\mathbf{s}}_1$ is the strike unit normal, and $\hat{\mathbf{s}}_2$ is the dip unit normal. The strike and dip normals can be defined in terms of a downward pointing unit normal $\hat{\mathbf{d}}$,

$$\hat{\mathbf{s}}_1 = \hat{\mathbf{n}} \times \hat{\mathbf{d}} \ , \tag{3.18}$$

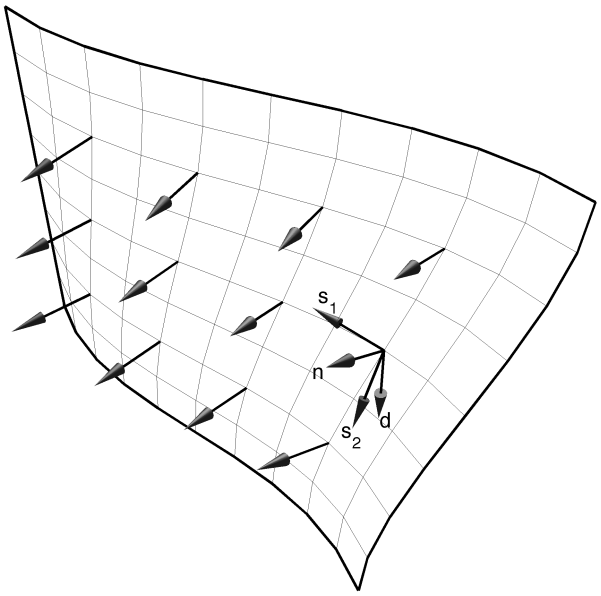

Figure 3.1: Non-planar fault with surface unit normals. Surface unit normal $\hat{\mathbf{n}}$ and downward unit vector $\hat{\mathbf{d}}$ define the local strike and dip coordinate system $(\hat{\mathbf{s}}_1, \hat{\mathbf{s}}_2, \hat{\mathbf{n}})$.

$$\hat{\mathbf{s}}_2 = \hat{\mathbf{s}}_1 \times \hat{\mathbf{n}} \ . \tag{3.19}$$

3.3 Numerical Method

Aside from a narrow selection of problems for which analytical solutions have been found, numerical approximations are needed to solve the equations of motion and fault boundary conditions outlined above. Our numerical algorithm discretizes the wave propagation problem using the Support Operators method (SOM) developed by *Ely et al.* (2008). The scheme is explicit in time, and uses a hexahedral, logically rectangular mesh. On the mesh we define the space of nodal functions H^N consisting of the hexahedra vertices, and the space of cell functions H^C consisting of the hexahedra volumes. Discrete variables are defined on the mesh with the same names as their corresponding continuous variables. On the nodes we have $(\rho, \gamma, \beta, \mathbf{x}, \mathbf{u}, \mathbf{v}, \mathbf{a}, \mathbf{g}) \in H^N$, and on the cells we have $(\lambda, \mu, \mathcal{Y}, \boldsymbol{\sigma}) \in H^C$. Hourglass viscosity β and hourglass

stiffness $\mathcal{Y}$, used for numerical stabilization, are explained below. Time is discretize with constant spacing Δt. Spatial derivatives are approximated with the discrete difference operators

$$D_i : H^N \rightarrow H^C \quad \text{and} \quad \mathcal{D}_i : H^C \rightarrow H^N \ . \tag{3.20}$$

Time derivatives are approximated with with second-order centered differences. The time index is indicated by a superscript, and for clarity, spatial indices are omitted in the discretized system of equations:

$$g_{ij} = D_j(u_i^n + \gamma v_i^{n-1/2}) \ , \tag{3.21}$$

$$\sigma_{ij} = \Lambda \, \delta_{ij} g_{kk} + M(g_{ij} + g_{ji}) \ , \tag{3.22}$$

$$a_i = R \, \mathcal{D}_j \, \sigma_{ij} - \mathcal{Q}_k \, \mathcal{Y} \, Q_k(u_i^n + \beta v_i^{n-1/2}) \ , \tag{3.23}$$

$$v_i^{n+1/2} = v_i^{n-1/2} + \Delta t \, a_i \ , \tag{3.24}$$

$$u_i^{n+1} = u_i^n + \Delta t \, v_i^{n+1/2} \ . \tag{3.25}$$

The material variables incorporate the cell volumes V^C and the node volumes V^N:

$$\Lambda = \frac{\lambda}{V^C} \ , \tag{3.26}$$

$$M = \frac{\mu}{V^C} \ , \tag{3.27}$$

$$R = \frac{1}{\rho V^N} \ . \tag{3.28}$$

Instabilities in the numerical method due to non-uniform stress modes are corrected for by hourglass operators

$$Q_k : H^N \rightarrow H^C \quad \text{and} \quad \mathcal{Q}_k : H^C \rightarrow H^N \ . \tag{3.29}$$

with hourglass viscosity β, and hourglass stiffness $\mathcal{Y}$. Detailed derivations of difference operators, hourglass corrections, and surface boundary conditions are provided in *Ely et al.* (2008).

For the fault boundary condition, we use a split node technique described by *Andrews* (1999) and *Day et al.* (2005). Here the method is generalized for non-planar surfaces, and it is also modified to allow for fault opening. The double nodes are constructed by inserting a layer of zero-thickness cells along the fault surface in which all of the cell valued functions $(\Lambda, M, \mathcal{Y}, \boldsymbol{\sigma})$ are zero. This has the effect of dividing the problem domain into two uncoupled regions, and for the nodal functions, places two sets of co-located values at each fault surface point. Equation (3.23) then gives the acceleration for a frictionless free surface at the double nodes. Coupling of the double nodes takes place by applying traction to the frictionless acceleration, to find modified acceleration

$$\tilde{a}_i^{\pm} = a_i^{\pm} \pm A(\tau_i - \tau_i^0)R^{\pm} \ , \tag{3.30}$$

where A is the portion of the fault surface area associated with each node. The nodal areas are found from the magnitude of the surface area normal vectors as detailed in Appendix A. Traction is constructed according to the fault boundary condition equations (3.7), (3.11), (3.12), and (3.14). We first find a trial traction, that is the value of traction required for zero relative velocity between the double nodes at the next time step,

$$\tilde{\tau}_i = \tau_i^0 + \frac{(v_i^+ - v_i^-) + \Delta t(a_i^+ - a_i^-)}{\Delta t A(R^+ + R^-)} \ . \tag{3.31}$$

The trial traction, if applied, would lock the current relative locations of the nodes. The tangential contribution to the trial traction is

$$\tilde{\tau}_i^s = \tilde{\tau}_i - \hat{n}_i \sum_{j=1}^{3} \hat{n}_j \, \tilde{\tau}_j \ , \tag{3.32}$$

that has the magnitude

$$|\tilde{\tau}^s| = \sqrt{(\tilde{\tau}_1^s)^2 + (\tilde{\tau}_2^s)^2 + (\tilde{\tau}_3^s)^2} \ . \tag{3.33}$$

We also calculate a trial value of normal traction required for zero relative normal displacement,

$$\tilde{\tau}^n = \sum_{i=1}^{3} \hat{n}_i \left[\tilde{\tau}_i + \frac{(u_i^+ - u_i^-)}{\Delta t^2 A (R^+ + R^-)} \right] \ . \tag{3.34}$$

This traction, if applied, would ensure zero separation of the split nodes, in the fault normal direction. We then apply the condition that normal traction cannot be tensional,

$$\tau^n = \begin{cases} 0 \ , & \tilde{\tau}^n \geq 0 \\ \tilde{\tau}^n, & \tilde{\tau}^n < 0 \ , \end{cases} \tag{3.35}$$

and the condition that shear traction is bound by the frictional strength,

$$\tau^s = \begin{cases} \tau_c \ , & |\tilde{\tau}^s| \geq \tau_c \\ |\tilde{\tau}^s| \ , & |\tilde{\tau}^s| < \tau_c \ . \end{cases} \tag{3.36}$$

Finally, the total traction on the fault can be assembled,

$$\tau_i = \tau^n \, \hat{n}_i + \tau^s \frac{\tilde{\tau}_i^s}{|\tilde{\tau}^s|} \ , \tag{3.37}$$

and then the modified nodal accelerations (3.30) are used to update the nodal velocities by equation (3.24).

3.4 Numerical Tests

To verify the numerical accuracy of our method we use one of a series of test problems developed for the dynamic earthquake rupture code validation exercise organized by the Southern California Earthquake Center (SCEC) and the U.S. Geological Survey (USGS) (*Harris and Archuleta*, 2004; *Harris et al.*, 2008). For test problem number 3 (TPV3), *Day et al.* (2005) computed both boundary integral (BI) and finite difference (FD) solutions to help establish mutual verification of the two methods. We preform a similar analysis here and use the BI solutions from *Day et al.* as a basis to compare TPV3 solutions computed with our SOM method.

TPV3 consists of a finite planar fault within an infinite elastic isotropic medium. The material and fault parameters for TPV3 are given in Table 3.1. Rupture occurs on a 30×15 km fault (diagrammed in Fig. 3.2) that is stressed parallel to the x axis. Rupture is nucleated by a 1.5×1.5 km patch in which shear traction is higher than the initial static frictional strength $\tau_c(\ell = 0)$. Rupture spreads spontaneously out from the nucleation patch, producing a mixed-mode rupture that reduces to pure mode II along the x axis and pure mode III along the y axis.

Accurate numerical solutions for rupture dynamics problems require sufficient resolution of the cohesive zone. For slip-weakening friction, the cohesive zone is the portion of the fault that has begun slipping, but not yet reached its dynamic friction level. *Day et al.* found that with a mesh resolution of 50 m (which we use for the SOM models) the cohesive zone is sampled with a least 6.5 nodes for TPV3, and that this is sufficient for accurate solutions (e.g., less than 1% error in rupture time). The resolution requirement for BI is lower, so we are able to use the coarser 100 m grid BI solution from *Day et al.*.

We preform three SOM calculations, one with a rectangular mesh of node spacing $\Delta x = 50$ m, and two more with meshes distorted by simple shearing. The first sheared

Table 3.1: TPV3 Model Parameters

Material Parameters		
ρ	Density	2670 kg/m^3
V_p	P-wave speed	6000 m/s
V_s	S-wave speed	3464 m/s
γ	Viscosity	0.02
$\mathcal{Y}$	Hourglass stiffness	1.0
β	Hourglass viscosity	2.0

Fault Parameters		Nucleation	Elsewhere
τ_n	Initial normal traction	-120 MPa	-120 MPa
τ_{s_1}	Initial shear traction	81.6 MPa	70.0 MPa
μ_s	Coefficient of static friction	0.677	0.677
μ_d	Coefficient of dynamic friction	0.525	0.525
d_0	Critical slip distance	0.4 m	0.4 m

mesh, pictured in Fig. 3.2, is constructed from the rectangular mesh by applying the coordinate mapping

$$\begin{bmatrix} X'_{jkl} \\ Y'_{jkl} \\ Z'_{jkl} \end{bmatrix} = \begin{bmatrix} X_{jkl} \\ Y_{jkl} \\ Z_{jkl} \end{bmatrix} + \begin{bmatrix} 0 & 1 & 1 \\ 0 & 0 & 0 \\ 0 & 0 & 0 \end{bmatrix} \begin{bmatrix} X_{jkl} \\ Y_{jkl} \\ -|Z_{jkl}| \end{bmatrix}, \tag{3.38}$$

where (X, Y, Z) are coordinates of the rectangular mesh and (X', Y', Z') are coordinates of the sheared mesh. We call this mesh 'S23'. The name is derived from positions of the non-zero coefficient in the transformation matrix (second and third positions, where elements are ordered with column index most rapidly varying). The

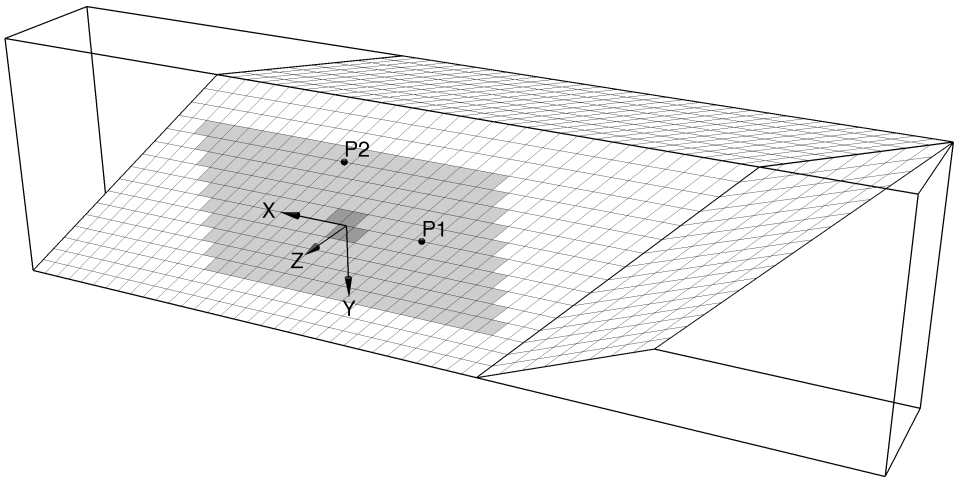

Figure 3.2: Schematic diagram of the model configuration for sheared mesh S23. The near fault block (a mirror image of the far block) is removed to allow viewing of the fault surface. Fault surface elements lying within the 30 × 15 km slipping portion of the fault are shaded gray. Elements in the 3 × 3 km nucleation patch are shaded dark gray. Slip is right-lateral, with mode II rupture along the x axis, and mode III rupture along the y axis. Observation points are located at P1 and P2.

second sheared mesh, named 'S26', is constructed from the mapping

$$\begin{bmatrix} X'_{jkl} \\ Y'_{jkl} \\ Z'_{jkl} \end{bmatrix} = \begin{bmatrix} X_{jkl} \\ Y_{jkl} \\ Z_{jkl} \end{bmatrix} + \begin{bmatrix} 0 & 1 & 0 \\ 0 & 0 & 1 \\ 0 & 0 & 0 \end{bmatrix} \begin{bmatrix} X_{jkl} \\ Y_{jkl} \\ -|Z_{jkl}| \end{bmatrix} . \tag{3.39}$$

Both mappings produce mirror symmetry across the fault plane, 45° shearing of the fault surface, and a maximum of 54.7° of shearing in the volume. However, the shapes of the elements are quite different between the two meshes.

To assess the level of agreement between BI and SOM solutions we first compare the rupture arrival time (defined as the time when slip velocity surpasses 1 mm/s) over the fault plane. During the early stages of rupture, the rupture arrival times agree closely among BI and SOM solutions (Fig. 3.3). At later times, the rectangular

SOM solution falls behind BI by as much as .022 s. The RMS difference (averaged over the fault plane) is .009 s, or about 0.24% of the average rupture time of 3.56 s. Rupture velocities on the sheared meshes are faster in the direction corresponding to the long axis of the sheared elements, matching BI for S26 and slightly exceeding BI for mesh S23. In the direction of the short axis of the elements, rupture velocities are similar to the rectangular case–slightly slower than BI. The maximum and RMS difference are .034 s and .010 s for mesh S23, and .021 s and .006 s for mesh S26.

Fig. 3.4 compares unfiltered times histories of shear traction, slip rate and slip at a point P1, 7.5 km from the origin in the mode II direction. All important features are closely matched, including: waveform shape and amplitude; time of initial rupture at 2.95 s; time of reflected arrival at 6.2 s; time of rupture arrest at 7 s; and the time of short rupture reactivation at 8 s. The largest misfit is due to small oscillations in the slip rate. At frequencies lower than the oscillations, the fit is nearly perfect. Fig. 3.5 shows a similar comparison for point P2, 6 km from the origin in the mode III direction.

Perhaps the most useful mesh deformation for earthquake rupture simulations is shearing in the plane defined by the fault surface normal and the slip vector. Shearing of this orientation does not effect the fault surface elements, and they remain rectangular. Volume element are defected towards or away from the slip vector. This geometry accommodates the case of dip-slip rupture on a dipping fault intersecting the free surface, as well as the case of a vertical strike-slip fault with variable strike. Low-angle thrust faults, in particular, may require drastic element deformations of this type, so it is important to understand the numerical affects of such deformations.

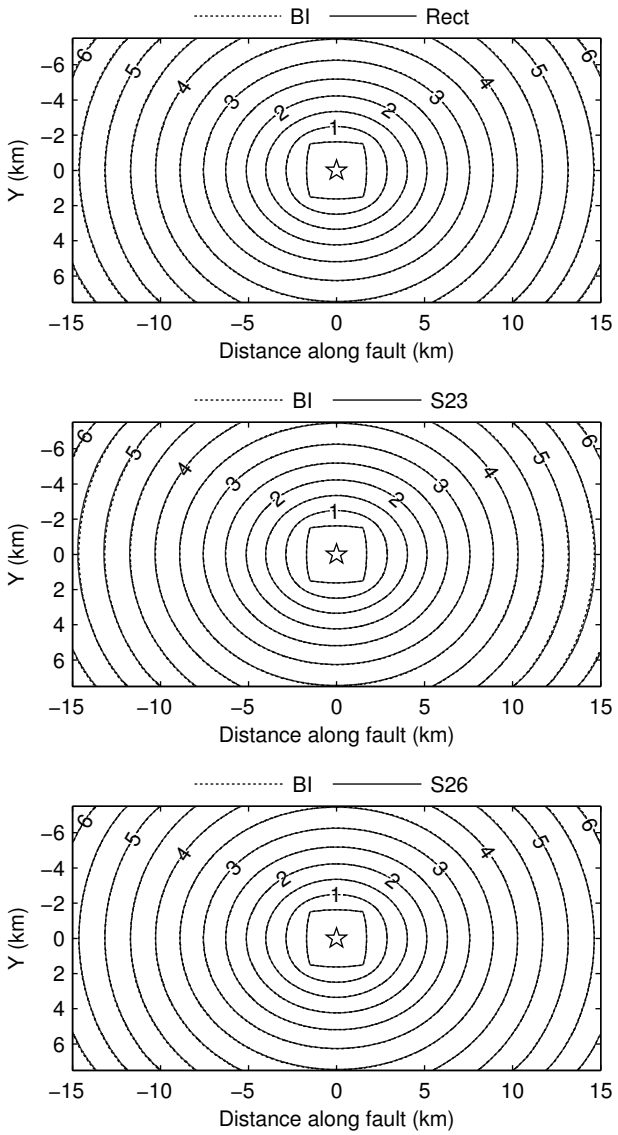

Figure 3.3: Rupture arrival time contours (s) comparing boundary integral solutions (BI) to SOM solutions for a rectangular mesh and for sheared meshes S23 and S26.

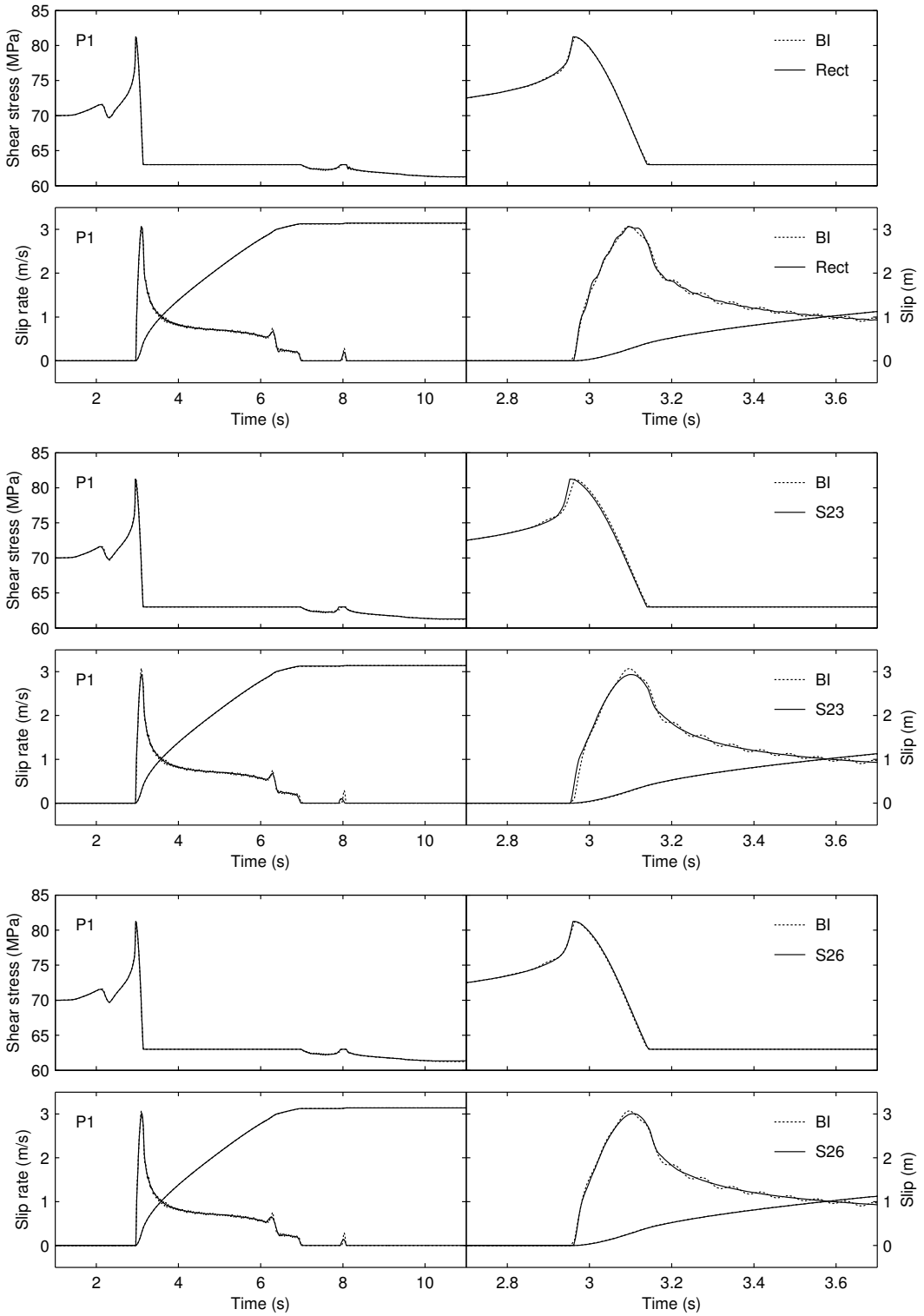

Figure 3.4: Time histories of shear stress, slip, and slip rate for the mode II, in-plane point P1. The right hand panels are magnified in time to show detail of the rupture arrival.

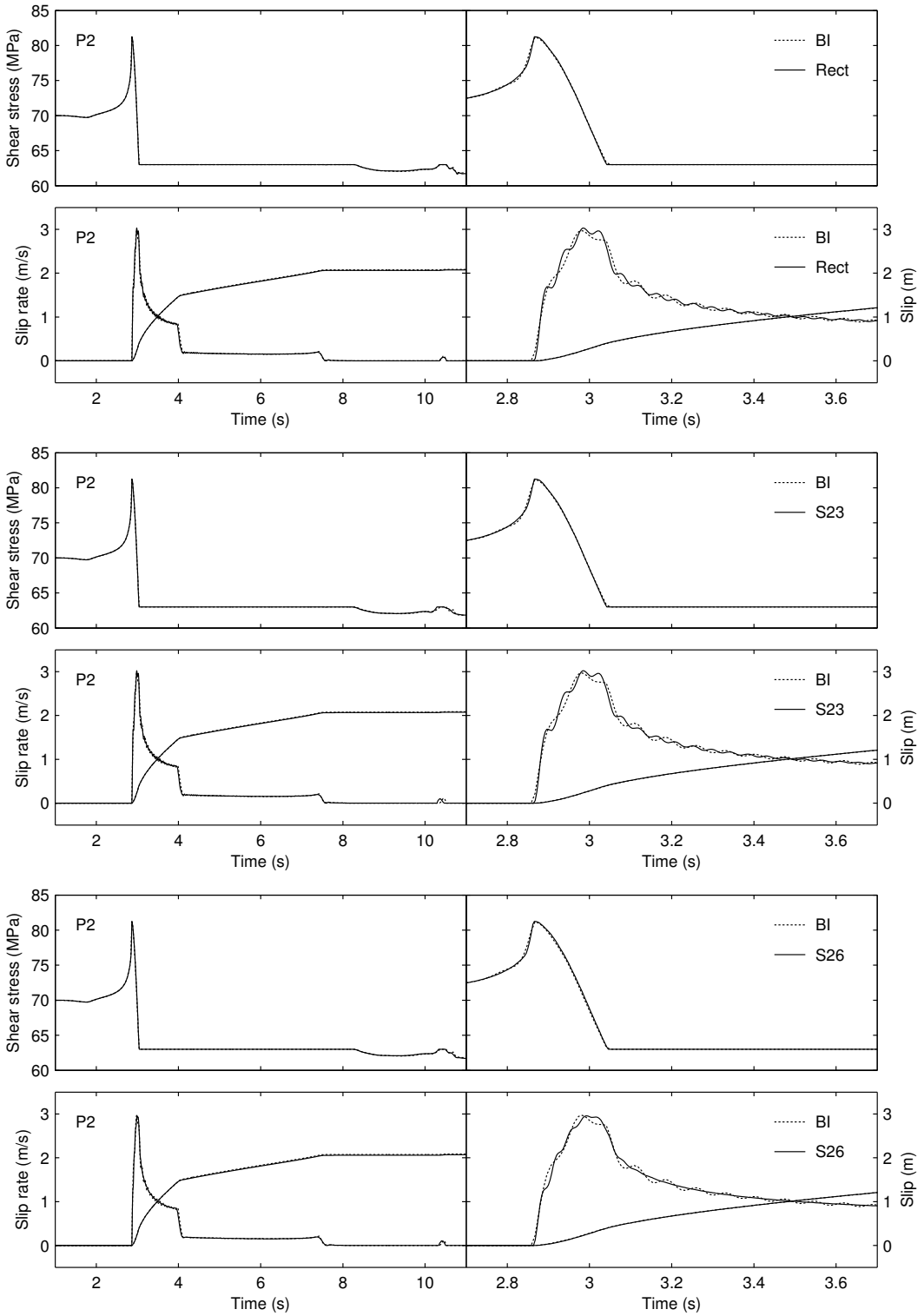

Figure 3.5: Time histories of shear stress, slip, and slip rate for the mode III, anti-plane point P2. The right hand panels are magnified in time to show detail of the rupture arrival.

To that end we ran a series of tests with the mapping

$$\begin{bmatrix} X'_{jkl} \\ Y'_{jkl} \\ Z'_{jkl} \end{bmatrix} = \begin{bmatrix} X_{jkl} \\ Y_{jkl} \\ Z_{jkl} \end{bmatrix} + \begin{bmatrix} 0 & 0 & e_{xz} \\ 0 & 0 & 0 \\ 0 & 0 & 0 \end{bmatrix} \begin{bmatrix} X_{jkl} \\ Y_{jkl} \\ -|Z_{jkl}| \end{bmatrix}, \tag{3.40}$$

where e_{xz} is a variable amount of mesh strain. In our naming scheme this mesh is called 'S3'. Mesh strain was increase to a maximum of 3, in increments of 0.5, resulting in a maximum shear angle of 72.6°.

Numerical errors are assessed by comparing each sheared mesh model to the reference rectangular mesh model. RMS differences in rupture arrival time, slip, and peak slip rate are computed for the entire 30×15 km slipping portion of the fault. The RMS differences increase logarithmically by roughly an order of magnitude over the 26.6° to 72.6° range of shearing (Fig. 3.6). At maximum shear the difference is 0.5% for rupture time, 0.6% for slip, and 10.3% for peak slip rate. These results indicate the method remains highly accurate for applications with modest shearing such as 60° dipping normal faults (30° shear) or vertical strike-slip faults with small changes in strike. Even for low-angle trust faults, with high amounts mesh shear, accuracy is likely acceptable for many applications.

3.5 Non-Planar Faults

Changes in fault direction can play an important role in the nucleation, termination, and radiated energy of earthquakes. Non-planar geometry provides a mechanism by which dynamic changes in normal stress (and therefor friction) can occur. Detailed study of non-planar rupture, using a variety of analysis and numerical methods, include work by *Andrews* (1989), *Tada and Yamashita* (1996), *Aochi et al.* (2000),

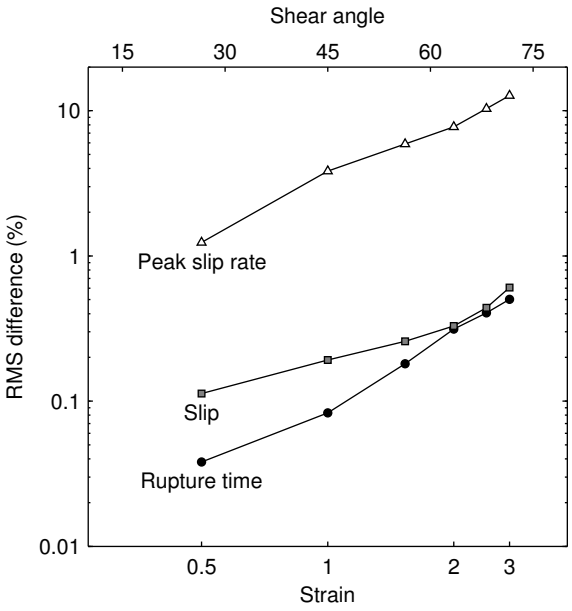

Figure 3.6: Difference in rupture time, slip, and peak slip rate as a function of shear strain applied to the mesh. Values are RMS averages over the fault plane, referenced to the rectangular case.

Poliakov et al. (2002), *Kase and Day* (2006), *Cruz-Atienza et al.* (2007), *Benjemaa et al.* (2007), and *Adda-Bedia and Madariaga* (2008). Laboratory scale model experiments have also been performed by *Rousseau and Rosakis* (2003). Here we make simple modifications to TPV3 to demonstrate the effects of fault curvature and sharp fault kinks.

Our test problems modify TPV3 by varying the strike direction, keeping the fault vertical, and keeping the total fault length the same at 30 km (Fig. 3.7). The first test problem has cylindrical fault geometry of radius $90/\pi$ km, with the ends of the fault rotated 30° relative the nucleation point. The second test problem has a kinked geometry consisting of three planar segments with a 30° change in strike 7.5 km from the nucleation point, on either side. The problems are otherwise identical to TPV3. The grids are constructed so that the fault is discretized with square elements having the same 50 km resolution as the rectangular planar model. No elements are sheared

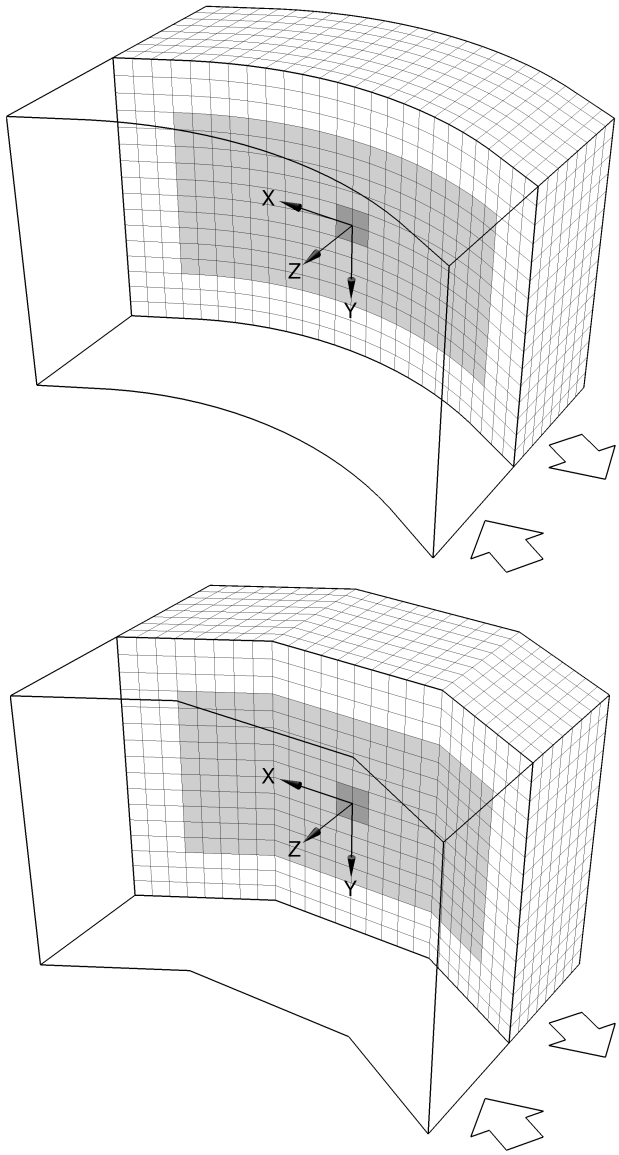

Figure 3.7: TPV3 modified for cylindrical fault geometry (top) and for kinked fault geometry (bottom).

more than 30°, so gauging from the sheared mesh tests, we can expect that RMS errors due to mesh shearing will be less than 0.2% for slip, less than 2% for slip rate, and less than 0.05% for rupture time.

Typically, non-planar fault studies have set up a uniform external stress field that is resolved onto the fault, resulting in variable traction conditions depending on the fault's local orientation. Here, we instead rotate the local initial stress field so that the resolved traction on the fault remains in a fixed orientation relative to the local fault orientation. The magnitudes of initial normal and shear traction are assigned uniform values over the fault surface, regardless of local orientation. The goal is to isolate the effects of non-planar geometry, without introducing heterogeneity in the initial resolved tractions on the fault. This scheme presents a problem for the case of a sharp kink, as it requires a discontinuity of stress at the kink. However, a perfectly sharp discontinuity can not be represented by discrete equations, so the sharp kink effectively becomes a curve of radius comparable to the discretization length in the numerical solution.

Symmetry in the planar TVP3 model ensures that normal traction of the fault remains constant at all times. A fundamental difference of the non-planar models is that fault slip induces dynamic changes in normal traction (and frictional strength) at other locations on the fault. In the cylindrical and kinked geometries, right-lateral slip results in decompression (lower strength) in the negative x direction, and compression (higher strength) in the positive x direction relative to the axis of the curve or kink. For the cylindrical model the normal traction change is a gradual, nearly linear function of distance along the fault (Fig. 3.8). The kinked model develops large stress concentrations at the kinks that rapidly decay with distance from the kink. The stress concentrations have a sign change at the axis of the kink that divides the decompressed side from the compressed side. In both models, the decompressed side

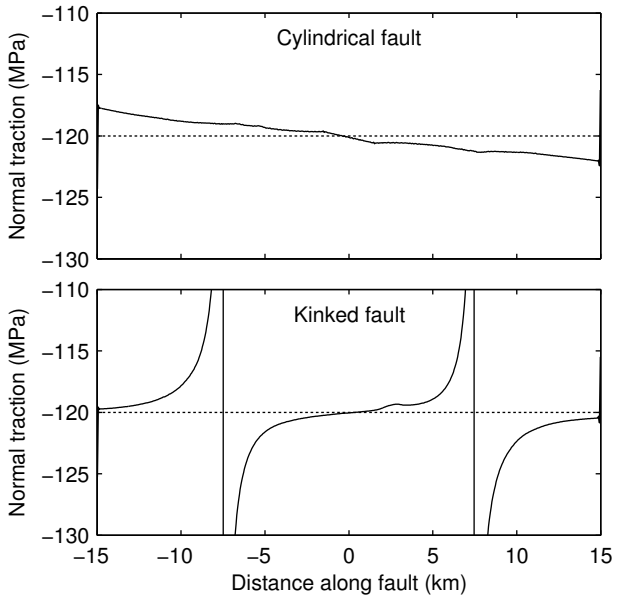

Figure 3.8: Profile of normal traction along the in-plane (horizontal) axis at time $t = 12\,\mathrm{s}$ for cylindrical and kinked fault models. For both models the negative x end of the fault is decompressed, and the positive x end is compressed relative to the initial value of $-120\,\mathrm{MPa}$ (dotted line). High stress concentrations develop at the kinks.

has higher rupture velocity (Fig. 3.9) and higher total slip (Fig. 3.10).

The total moment release for the cylindrical model (34.0×10^{18} N-m) is greater than the planar model (33.2×10^{18} N-m), and the moment release for the kinked model (27.9×10^{18} N-m) is lower than the planar model. The lower moment for the kinked model is due to the partial barriers to slip formed by the kinks, as seen in slip profiles along the in-plane axis (Fig. 3.11). The kink barrier in the positive x side causes rupture to pause for about two seconds before continuing to the next fault segment. The two second pause is clearly visible in a space-times plot of slip acceleration (Fig. 3.12).

Another effect seen in the space-time plot is the radiation of P and S waves from the fault kicks at the time of their initial rupture. The kinked model in general has a more complicated rupture history compared to the planar and cylindrical models.

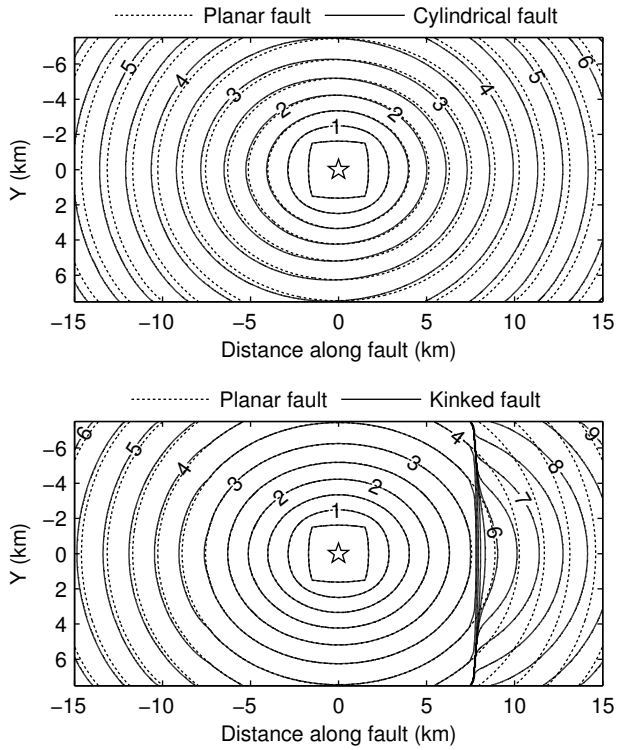

Figure 3.9: Rupture arrival time (s) for planar, cylindrical and kinked fault models.

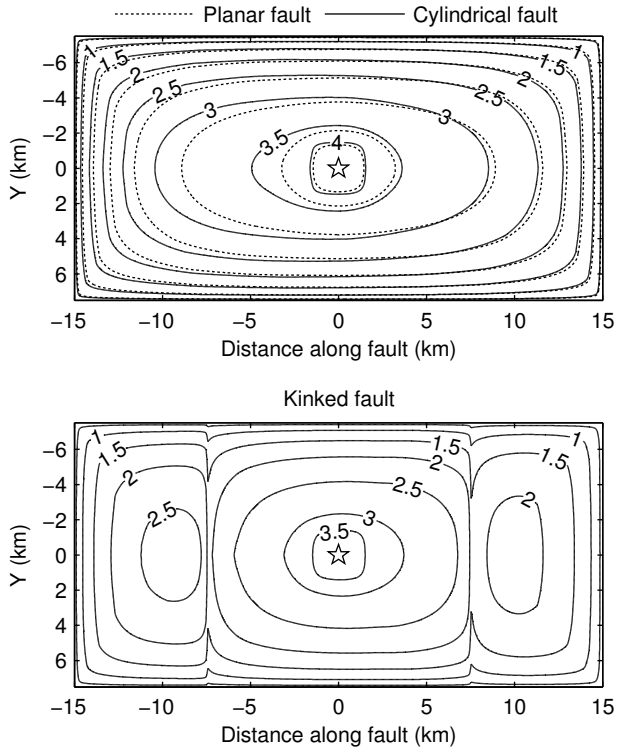

Figure 3.10: Final slip magnitude (m) for planar, cylindrical and kinked fault models.

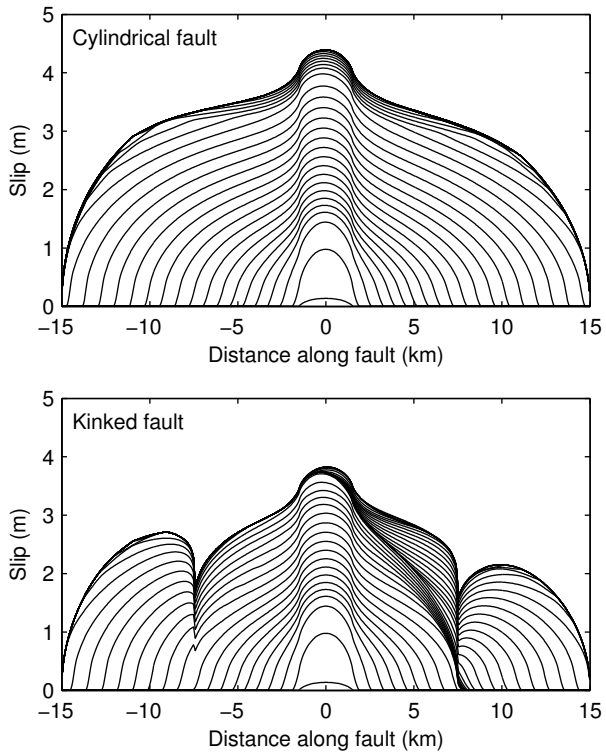

Figure 3.11: Profile of slip magnitude along the in-plane (horizontal) axis at 0.3 s intervals.

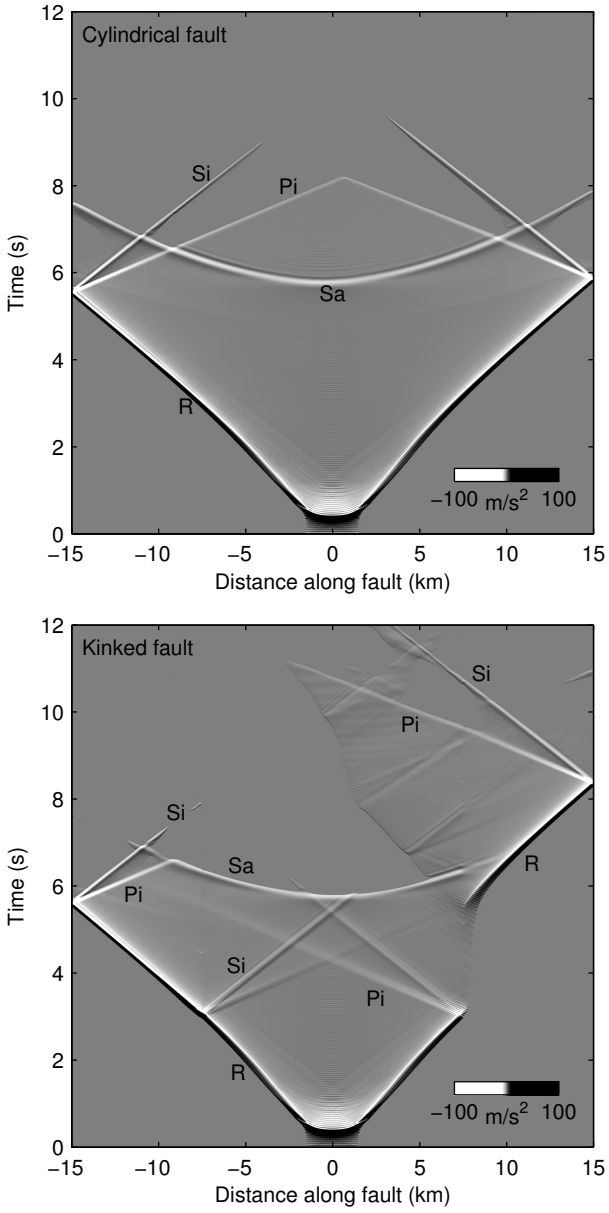

Figure 3.12: Space-time plots of slip acceleration magnitude along the in-plane (horizontal) axis. R inicates initial rupture. Pi and Si indicate horizontally traveling P and S waves, reflected by kinks and lateral fault boundaries. Sa indicates vertically traveling S waves reflected by the top and bottom fault boundaries.

For the cylindrical model, the space-time plot shows that rupture along the antiplane axis is primarily halted by the P-wave reflected from the lateral fault boundaries (marked Pi). Towards the edges, rupture is briefly reactivated by laterally reflected S-waves (Si) or vertically reflected S-waves (Sa). By contrast much of the kinked model rupture is halted by the Sa wave. Rupture is reactivated on most of the central segment after rupture begins on the compressed segment following the two second pause. This second rupture stage is halted by a Pi wave and in some places briefly reactivated by an Si wave.

3.6 Conclusion

We have extended the Support Operator numerical scheme for three-dimensional viscoelastic wave propagation, previously developed by *Ely et al.* (2008), to model non-planar spontaneous rupture. We implement a slip weakening friction model, and the method is readily adaptable to other types of friction laws. The method is verified against a boundary integral solution for planar rupture problems using both rectangular meshes and meshes distorted by shearing. The accuracy of the sheared mesh tests indicates that the method is suitable for modeling low-angle surface rupturing thrust faults. Non-planar rupture effects were demonstrated using a cylindrical fault geometry as well as a planar segmented, or kinked, geometry. The kinked geometry introduces significant rupture complexity relative to planar and cylindrical cases, with the kinks acting as partial barriers to slip that lead to high stress concentrations.

Acknowledgments

We are thankful to Nadia Lapusta and Yi Liu for providing Boundary Integral solutions for the verification test problem, and to Luis Dalguer for assistance with

the solution comparisons. This work was supported by the National Science Foundation under grants ATM-0325033 and EAR-0122464, and by the Southern California Earthquake Center. SCEC is funded by NSF Cooperative Agreement EAR-0106924 and USGS Cooperative Agreement 02HQAG0008. The SCEC contribution number for this paper is 1163 This chapter, in full, is under review by Geophysical Journal International. The dissertation author is the primary investigator and author of this paper, with Steven Day and Jean-Bernard Minster as co-authors.

References

Aagaard, B. T. (1999), Finite-element simulations of earthquakes, *Technical Report EERL-99-03*, California Institute of Technology, Earthquake Engineering Research Laboratory, Pasadena, CA.

Adda-Bedia, M., and R. Madariaga (2008), Radiaton from a kink on an antiplane fault, *Bull. Seism. Soc. Am.*, in press.

Andrews, D. J. (1989), Mechanics of fault junctions, *J. Geophys. Res.*, *94*(B7), 9389–9397, doi:10.1029/89JB00774.

Andrews, D. J. (1999), Test of two methods for faulting in finite-difference calculations, *Bull. Seism. Soc. Am.*, *89*(4), 931–937.

Aochi, H., E. Fukuyama, and M. Matsuâura (2000), Spontaneous rupture propagation on a non-planar fault in 3-D elastic medium, *Pageoph*, *157*(11), 2003–2027, doi:10.1007/PL00001072.

Benjemaa, M., N. Glinsky-Olivier, V. M. Cruz-Atienza, J. Virieux, and S. Piperno (2007), Dynamic non-planar crack rupture by a finite volume method, *Geophys. J. Int.*, *171*(1), 271—285, doi:10.1111/j.1365-246X.2006.03500.x.

Berenger, J.-P. (1994), A perfectly matched layer for the absorption of electromagnetic waves, *J. Comput. Phys.*, *114*(2), 185–200, doi:10.1006/jcph.1994.1159.

Berenger, J.-P. (1996), Three-dimensional perfectly matched layer for the absorption of electromagnetic waves, *J. Comput. Phys.*, *127*(2), 363–379, doi:doi:10.1006/jcph.1996.0181.

Cruz-Atienza, V. M., J. Virieux, and H. Aochi (2007), 3D finite-difference dynamic-rupture modelling along non-planar faults, *Geophysics*, *72*(5), SM123–SM137, doi:10.1190/1.2766756.

Day, S. M., L. A. Dalguer, N. Lapusta, and Y. Liu (2005), Comparison of finite difference and boundary integral solutions to three-dimensional spontaneous rupture, *J. Geophys. Res.*, *110*(B12307), doi:10.1029/2005JB003813.

Ely, G. P., S. M. Day, and J.-B. Minster (2008), A support-operator method for visco-elastic wave modeling in 3d heterogeneous media, *Geophys. J. Int.*, *172*(1), 331–344, doi:10.1111/j.1365-246X.2007.03633.x.

Festa, G. (2004), Fault dynamics with spectral elements and slip imaging by isochone back-projection, Ph.D. thesis, Alma Mater Studiorum - Università di Bologna.

Harris, R. A., and R. J. Archuleta (2004), Earthquake rupture dynamics: Comparing the numerical simulation methods, *Eos Trans. AGU*, *85*(34), 321, doi:10.1029/2004EO340003.

Harris, R. A., et al. (2008), The SCEC/USGS dynamic earthquake rupture code validation exercise, *Seism. Res. Lett.*, in review.

Kase, Y., and S. M. Day (2006), Spontaneous rupture processes on a bending fault, *Geophys. Res. Lett.*, *33*(L10302), doi:10.1029/2006GL025870.

Oglesby, D. D., R. J. Archuleta, and S. B. Nielsen (2000), The three-dimensional dynamics of dipping faults, *Bull. Seism. Soc. Am.*, *90*(3), 616–628, doi:10.1785/0119990113.

Poliakov, A. N. B., R. Dmowska, and J. R. Rice (2002), Dynamic shear rupture interactions with fault bends and off-axis secondary faulting, *J. Geophys. Res.*, *107*(B11), 2295, doi:10.1029/2001JB000572.

Rousseau, C.-E., and A. J. Rosakis (2003), On the influence of fault bends on the growth of sub-Rayleigh and intersonic dynamic shear ruptures, *J. Geophys. Res.*, *108*(B9), 2411, doi:10.1029/2002JB002310.

Samarskii, A., V. Tishkin, A. Favorskii, and M. Shashkov (1981), Operational finite-difference schemes, *Diff. Eqns.*, *17*, 854–862.

Samarskii, A., V. Tishkin, A. Favorskii, and M. Shashkov (1982), Employment of the reference-operator method in the construction of finite difference analogs of tensor operations, *Diff. Eqns.*, *18*, 881–885.

Shashkov, M. (1996), *Conservative Finite-Difference Methods on General Grids*, CRC Press, Boca Raton, FL.

Tada, T., and T. Yamashita (1996), The paradox of smooth and abrupt bends in two-dimensional in-plane shear-crack mechanics, *Geophys. J. Int.*, *127*(3), 795–800, doi:10.1111/j.1365-246X.1996.tb04058.x.

Vilotte, J., G. Festa, and R. Madariaga (2005), Spectral element simulations of rupture dynamics along kinked faults, *Eos Trans. AGU*, *86*(52), Fall Meet. Suppl., Abstract S34A–02.

Zhang, W., T. Iwata, and K. Irikura (2006), Dynamic simulation of a dipping fault using a three-dimensional finite difference method with nonuniform grid spacing, *J. Geophys. Res.*, *111*(B05301), doi:10.1029/2005JB003725.

Appendix: Calculation of Surface Normals and Nodal Areas

Surface normals and nodal areas are needed for the fault boundary calculations. On a hexahedral mesh they may be found as follows. Quadratic interpolation of 3×3 patch of boundary surface nodes with coordinates $\mathbf{X}_{jk}$ is given by

$$\mathbf{x}(\boldsymbol{\xi}) = \sum_{j,k=0}^{2} N_{jk}(\boldsymbol{\xi}) X_{jk} \ , \tag{3.41}$$

where the shape functions $N_{jkl}(\boldsymbol{\xi})$ are formed from Lagrange interpolation polynomials

$$N_{jk}(\boldsymbol{\xi}) = \ell_j^2(\xi)\ell_k^2(\eta) \ . \tag{3.42}$$

The Lagrange polynomials of degree 2 are

$$\ell_j^2(\xi) = \prod_{\substack{i=0 \\ i \neq j}}^{2} \frac{\xi - \Xi_i}{\Xi_j - \Xi_i} \ . \tag{3.43}$$

The interpolation maps continuous Cartesian coordinates $\mathbf{x}$ to logical coordinates $\boldsymbol{\xi}$, and discrete nodal coordinates $\mathbf{X}_{jk}$ to logical nodal coordinates $\boldsymbol{\Xi}_{jk}$. Surface area

vectors are given by the Jacobian of the coordinate mapping

$$d\mathbf{S} = \frac{\partial \mathbf{x}}{\partial \xi} \times \frac{\partial \mathbf{x}}{\partial \eta} = \begin{bmatrix} \begin{vmatrix} \frac{\partial y}{\partial \xi} & \frac{\partial z}{\partial \xi} \\ \frac{\partial y}{\partial \eta} & \frac{\partial z}{\partial \eta} \end{vmatrix} \\ \begin{vmatrix} \frac{\partial z}{\partial \xi} & \frac{\partial x}{\partial \xi} \\ \frac{\partial z}{\partial \eta} & \frac{\partial x}{\partial \eta} \end{vmatrix} \\ \begin{vmatrix} \frac{\partial x}{\partial \xi} & \frac{\partial y}{\partial \xi} \\ \frac{\partial x}{\partial \eta} & \frac{\partial y}{\partial \eta} \end{vmatrix} \end{bmatrix} \tag{3.44}$$

The magnitude of the Jocobian $J = |d\mathbf{S}|$ gives the area accociated with each mesh node, and the surface unit normal is $\hat{n} = d\mathbf{S}/J$. Evaluating (3.41) at the central node $d\mathbf{S}(\mathbf{\Xi}_{11})$ gives

$$\begin{aligned} dS^x_{11} = \frac{1}{12} & \\ & \Big[Y_{21}(Z_{12} - Z_{10} + Z_{22} - Z_{20}) \\ & + Y_{12}(Z_{01} - Z_{21} + Z_{02} - Z_{22}) \\ & + Y_{01}(Z_{10} - Z_{12} + Z_{00} - Z_{02}) \\ & + Y_{10}(Z_{21} - Z_{01} + Z_{20} - Z_{00}) \\ & + Y_{22}(Z_{12} - Z_{21}) \\ & + Y_{00}(Z_{10} - Z_{01}) \\ & + Y_{02}(Z_{01} - Z_{12}) \\ & + Y_{20}(Z_{21} - Z_{10}) \Big] \end{aligned} \tag{3.45}$$

$$
\begin{aligned}
dS^y_{11} = \frac{1}{12} & \\
&\Big[Z_{21}(X_{12} - X_{10} + X_{22} - X_{20}) \\
&+Z_{12}(X_{01} - X_{21} + X_{02} - X_{22}) \\
&+Z_{01}(X_{10} - X_{12} + X_{00} - X_{02}) \\
&+Z_{10}(X_{21} - X_{01} + X_{20} - X_{00}) \\
&+Z_{22}(X_{12} - X_{21}) \\
&+Z_{00}(X_{10} - X_{01}) \\
&+Z_{02}(X_{01} - X_{12}) \\
&+Z_{20}(X_{21} - X_{10})\Big]
\end{aligned}
\tag{3.46}
$$

$$
\begin{aligned}
dS^z_{11} = \frac{1}{12} & \\
&\Big[X_{21}(Y_{12} - Y_{10} + Y_{22} - Y_{20}) \\
&+X_{12}(Y_{01} - Y_{21} + Y_{02} - Y_{22}) \\
&+X_{01}(Y_{10} - Y_{12} + Y_{00} - Y_{02}) \\
&+X_{10}(Y_{21} - Y_{01} + Y_{20} - Y_{00}) \\
&+X_{22}(Y_{12} - Y_{21}) \\
&+X_{00}(Y_{10} - Y_{01}) \\
&+X_{02}(Y_{01} - Y_{12}) \\
&+X_{20}(Y_{21} - Y_{10})\Big]
\end{aligned}
\tag{3.47}
$$

Quadratic interpolation cannot be used at the edge and corners nodes of the surface where the 3×3 stencil would otherwise extend outside of the mesh. In this case we may instead use linear interpolation in the direction normal to the edge. Fortunately, this does not require constructing separate operators for each special case. It is handled more simply by extending the mesh with ghost nodes, and duplicating the edge node

coordinates into the ghost nodes. It can be shown that when the interior operators (3.45)-(3.47) are applied at edges with such ghost nodes, the equations automatically reduce to the proper linear interpolation equations.

Chapter 4

Dynamic Rupture Models for the Southern San Andreas Fault

Abstract

Dynamic rupture, and resultant ground motions up to 0.25 Hz, are simulated for a M_w7.6 earthquake on the southern San Andreas Fault. Spontaneous rupture is modeled with slip-weakening friction, and viscoelastic wave solutions are computed with an explicit support-operator method. Piecewise planar geometry is used for the fault surface. Initial traction conditions are derived from inversions of the M_w7.3 1992 Landers strong ground motion records. The fault geometry and traction distribution borrow heavily from the TeraShake2 simulations by *Olsen et al.* (2008). Heterogeneity in the traction model leads to focusing of the rupture front, in some cases producing super-shear rupture velocity in areas of high initial traction (asperities). Rupture focusing sometimes occurs between the asperities, with the notable result that the highest peak slip rates occur in areas of low initial traction. Low frequency ground motion agrees with TeraShake2, though amplitudes are smaller due to the lower overall event size (TeraShake2 simulated a M_w7.7 event). Separate solutions are

computed for version 3.0 and 4.0, respectively, of the Southern California Earthquake Center Community Velocity Model (SCEC-CVM). We also compare the case of a flat ground surface (a common simplification made for finite difference calculations such as TeraShake) to the case of the ground surface conformed to regional topography. We find that the differences in the velocity models and the ground surface representations have minimal effect on the early stages of rupture (before the event has reached its full size) but the effects become substantial in the later stages of rupture. As first seen in the TeraShake1 simulations (*Olsen et al.*, 2006), stronger than expected ground motions occur at the site of Montebello, due to a basin wave guide, though the effect is not as strong in version 4.0 of the SCEC-CVM relative to version 3.0. The overall distribution of simulated peak ground velocities is consistent with those derived from the empirical model of *Campbell and Bozorgnia* (2007) for M_w7.6, in the sense that the bulk of simulated PGVs are within the 16–84% probability of exceedance (POE) range. Those simulated PGVs that would correspond to lower POE in the Campbell/Bozorgnia empirical model are principally associated with basin wave-guide and directivity effects.

4.1 Introduction

The southern San Andreas fault (SAF) is one of the most likely sources for the next large earthquake in Southern California. The *Working Group on California Earthquake Probabilities* (1995) estimates the The San Bernardino Mountain segment has a 28% probability of rupturing within 30 years, and the Coachella Valley segment has a 22% probability. A combined rupture of both segments, that study estimates, would produce a M_w7.6 earthquake in close proximity to the greater Los Angeles area. The San Bernardino and Coachella segments last ruptured in 1812 and 1690 ± 20, respectively (*Weldon et al.*, 2004), events that occurred well before the deployment of

seismic networks in southern California. So, in the absence of ground motion records from a large SAF event in this region, we are faced with large uncertainty in the expected ground motion from a future event.

Large scale numerical simulations have been used to help address some of this uncertainty. The TeraShake1 simulations by *Olsen et al.* (2006) modeled 0–0.5 Hz motion from a M_w7.7 event on the southern SAF, using kinematic source models. The kinematic sources were derived from slip models of the 2002 M_w7.9 Denali earthquake by *Oglesby et al.* (2004). Wave fields were propagated through the Southern California Earthquake Center Community Velocity Model (SCEC-CVM) version 3.0 (*Magistrale et al.*, 2000; *Kohler et al.*, 2003) with a staggered grid finite difference method. For a NW propagating rupture, they found unexpectedly large ground motion in Los Angeles basin that they attribute to a wave guide effect. The wave guide is formed by the continuous chain of basins, connecting the fault zone to the Los Angeles basin, lying at the southern foot of the San Gabriel and San Bernardino mountains. The assumption of constant rupture velocity in their kinematic model, however, may have over-estimated rupture directivity effects. TeraShake1 was followed by the TeraShake2 simulations by *Olsen et al.* (2008) that investigated similar scenarios, replacing the kinematic models with spontaneous rupture models. They found that the reduced coherency of the wave field due to source complexities in the dynamic model, that were not present in the kinematic TeraShake1 simulations, significantly reduced the predicted ground motion in Los Angeles. They considered multiple scenarios with different initial stress models, including both NW and SE propagating unilateral rupture. A two step procedure was used in which the fault and velocity model were first conformed to rectangular mesh (as required by the staggered finite difference method) for computation of the spontaneous rupture solution on a planar fault. The resultant slip motions were then mapped back to their proper spatial positions (on the

original non-planar fault model of the SAF) and used as kinematic source functions for the wave propagation simulation.

This study reexamines one of the NW propagating TeraShake2 scenarios, with updated version 4.0 of the SCEC-CVM (*Magistrale*, 2005). Simulations are performed with the Support Operator Rupture Dynamics (SORD) code developed by *Ely et al.* (2008). SORD is based on a numerical scheme able to handle non-planar boundaries, allowing rupture dynamics (on the non-planar SAF model) and wave propagation to be computed simultaneously, and allowing true topography to be included in the simulations (as was not the case in the TeraShake models). We present a set of spontaneous rupture models that compare rupture behavior and ground motion using the two versions of the SCEC-CVM and also compare results from a flattened topography model with those from a model incorporating true southern California topography and bathymetry at the free surface.

4.2 Wave Propagation Model

The modeling region is a $600 \times 300 \times 80$ km volume that includes southern California, northern Baja California, southwestern-most Arizona, the western Mojave Desert, the southern San Joaquin valley, and the Channel Islands. The elastic properties of the volume are obtained from the SCEC-CVM, a three-dimensional model of the upper mantle, crust, and sedimentary basins, compiled from a broad range of sources, including surface geology, geotechnical borings, gravity, seismic refraction, regional and teleseismic tomography, and teleseismic receiver functions. Version 4.0 of the SCEC-CVM (*Magistrale*, 2005) updates version 3.0 with a more complete description of the Salton Trough (Fig. 4.1) and shallower depth to basement rock in the Chino basin based on gravity and seismic reflection data (Fig. 4.2 and 4.3).

Wave solutions in the volume are computed with an explicit support operator

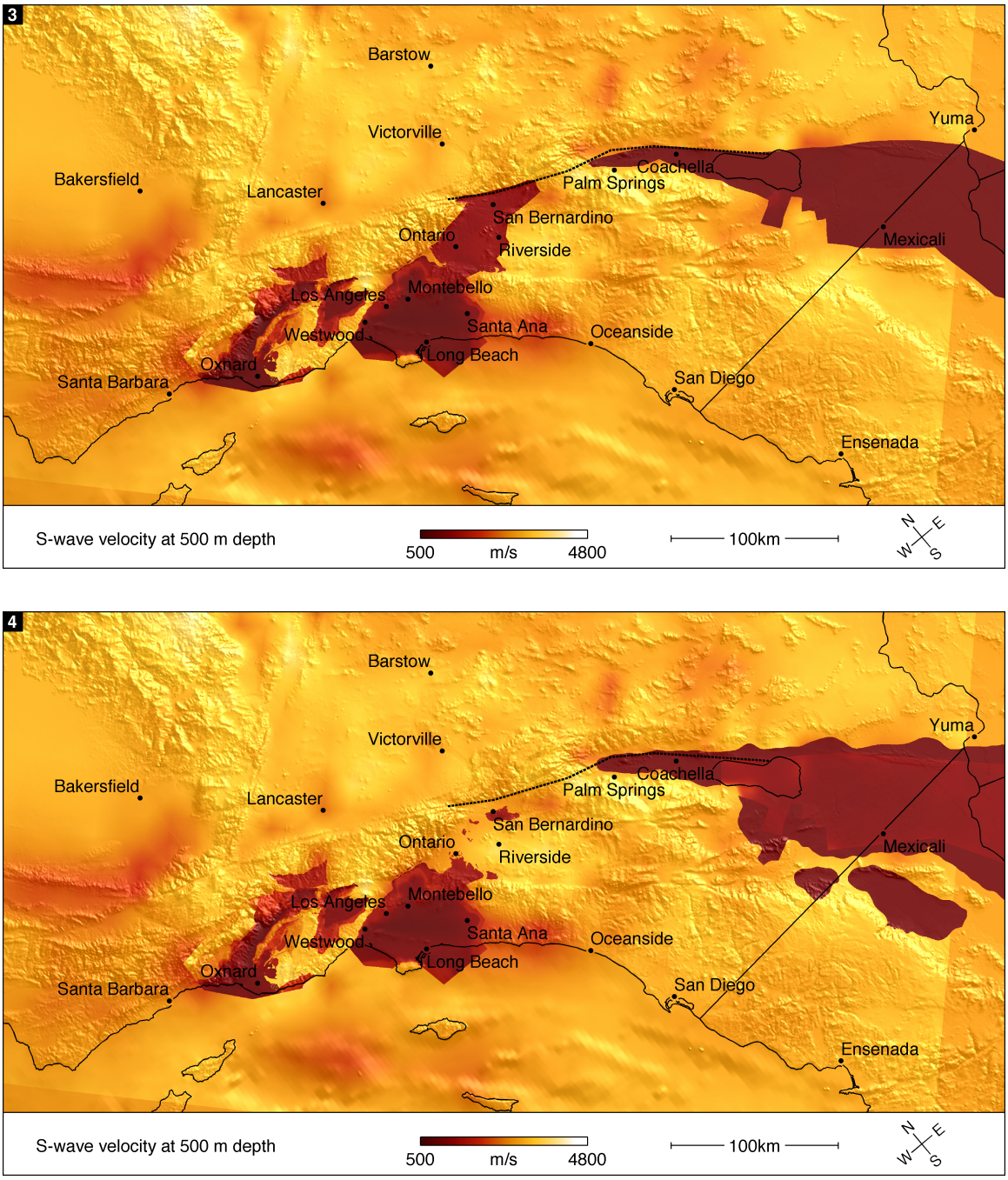

Figure 4.1: S-wave velocity at 500 m depth for the SCEC-CVM version 3.0 (top) and version 4.0 (bottom). The dashed line marks the location of the vertical strike-slip rupture. The Salton Trough, underlying Coachella and Mexicali, and incomplete in version 3.0, is updated in version 4.0.

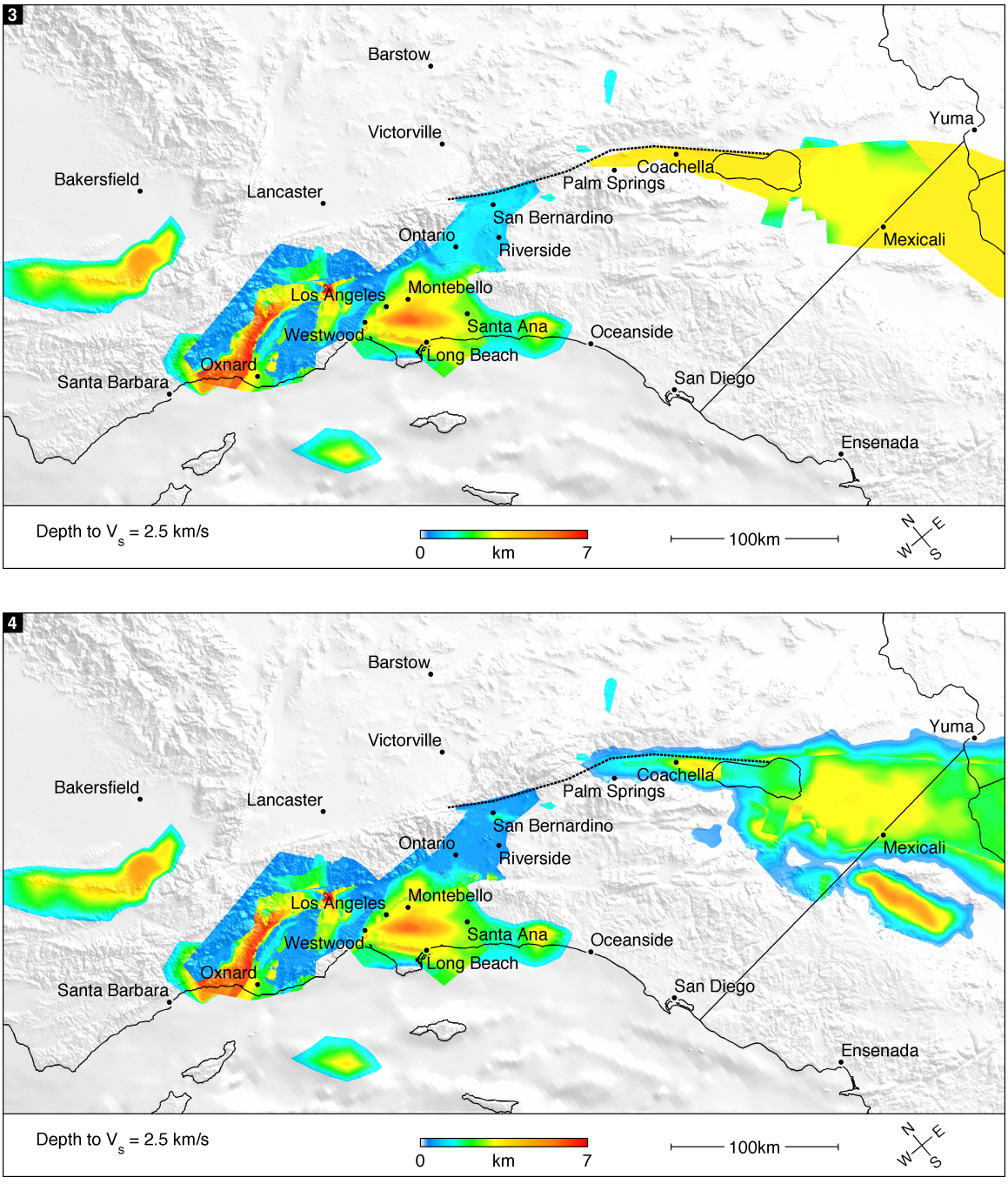

Figure 4.2: Sedimentary basin depth for the SCEC-CVM version 3.0 (top) and version 4.0 (bottom), as defined by the depth to the shallowest occurrence of S-wave velocities greater than or equal to 2.5 km/s.

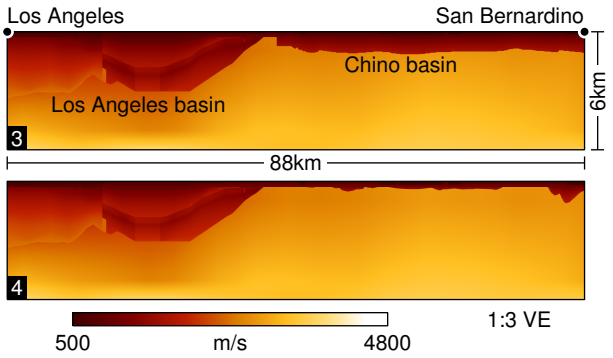

Figure 4.3: Cross-section of S-wave velocity from Los Angeles to San Bernardino, comparing SCEC-CVM version 3.0 (top) and version 4.0 (bottom). The Chino basin at this location is 1 km deep in version 3.0, and 400 m deep in version 4.0.

method (*Ely et al.*, 2008). The method uses non-rectangular hexahedral meshes, and is second-order accurate in space and time. The Kelvin-Voigt model of viscoelasticity is used, for which the anelastic quality factor Q is inversely proportional to wave frequency. Besides the anelastic energy losses (attenuation) provided by this model during wave propagation, the viscosity helps to prevent numerical noise from affecting the (nonlinear) rupture calculations. Numerical dispersion extends to lower frequencies in low-velocity material, so we set viscosity inversely proportional to the S-wave velocity, by the ratio $\gamma = 400/V_s$. In order to increase the resolvable bandwidth of the simulations, we set artificial lower limits of 500 m/s for S-wave velocity, and 1500 m/s for P-wave velocity. For second-order methods, such as this one, numerical dispersion results in phase velocity errors of about 1% at a resolution of 10 grid points per wavelength (*Virieux*, 1986). Using this as a minimum resolution, and given the node spacing of 200 m used, we should be able to resolve frequencies up to 0.25 Hz with reasonable accuracy. For comparison, the forth-order finite difference method of the TeraShake simulations, needing approximately 5 grid points per wavelength, is able to resolve up to 0.5 Hz, for the same grid spacing. Additionally, TeraShake incorporates a more realistic attenuation model using the course-grained memory vari-

Table 4.1: Comparative summary of the numerical wave simulation methods used for TeraShake simulations by *Olsen et al.* (2008) and for the Support Operator Rupture Dynamics (SORD) code.

	TeraShake	SORD
Numerical scheme	Finite difference	Support operator
Operator accuracy	$O(\Delta x^4, \Delta t^2)$	$O(\Delta x^2, \Delta t^2)$
Points-per-wavelength requirement	$\approx$5	$\approx$10
Mesh	Uniform rectangular, staggered grid	Hexahedral, partially staggered grid
Attenuation model	Course grain memory $Q \sim V_s$	Kelvin-Voight viscosity $Q \sim V_s\omega^{-1}$
Absorbing boundary	PML	PML

able technique (*Day*, 1998; *Day and Bradley*, 2001). The memory variable technique can model attenuation that is nearly constant with respect to frequency, which is a good representation of crustal material within the simulation bandwidth. The higher order accuracy and more realistic attenuation model make the TeraShake method superior for modeling waves in rectangular geometries. The advantage of SORD, and similar methods, is in modeling non-planar topography and fault surfaces. Both TeraShake and SORD suppress artificial boundary reflections with perfectly matched layers (PML), introduced by *Berenger* (1994, 1996), and adapted to their respective numerical schemes by *Marcinkovich and Olsen* (2003) and *Ely et al.* (2008). A summary of the relative merits of TeraShake and SORD is given in Table 4.1.

4.3 Source Model

The fault geometry is modeled by five planar segments vertically extrapolated from the SAF trace in the 2002 USGS National Hazard Maps by *Frankel et al.* (2002). The total length is 200 km, and the depth is 16 km. This simplified geometry facilitated the procedure used in TeraShake2 to map the fault and surrounding velocity model to a rectangular grid. Though our numerical scheme does not have the same geometrical restrictions, we use identical fault geometry for consistency in comparing results. The largest misrepresentation of the simplified geometry lies in the constricting bend east of San Gregornio Pass (at about the midpoint of the rupture trace), where the true fault dip is much less than 90° (*Seeber and Armbruster*, 1995) and, by geometrical considerations, the slip must have a thrust component.

Spontaneous rupture is modeled with a frictional boundary condition across the fault surface at which the frictional strength is determined by the negative product of the normal traction τ_n (negative in compression) and the coefficient of friction μ_f. The fault slips accordingly so that shear traction never exceeds the frictional strength

$$|\boldsymbol{\tau}_s| \leq -\mu_f \tau_n \ . \tag{4.1}$$

The model of friction is a slip-weakening law, with the coefficient of friction given by

$$\mu_f(\ell) = \begin{cases} \mu_s - (\mu_s - \mu_d)\ell/d_0 & \ell \leq d_0 \\ \mu_d & \ell > d_0 \ , \end{cases} \tag{4.2}$$

where μ_s and μ_d are the coefficients of static and dynamic friction, ℓ is the slip path length, and d_0 is the slip-weakening distance. A more complete discussion of the fault boundary condition is give by *Day et al.* (2005).

To obtain a plausible set of dynamic parameters for the TeraShake2 scenarios,

Olsen et al. (2008) used the results of a dynamic inversion of the M_w7.3 1992 Landers earthquake by *Peyrat et al.* (2001) that achieved good fit to Landers near-field strong motion records in the 0-0.5 Hz band. For TeraShake2, the Landers inversion was scaled up to a M_w7.7 event by replicating the rupture three times laterally to extend it to the total length to 200 km. Strong ground motion provides fairly good constraint on the stress drop $\Delta\tau = |\boldsymbol{\tau}_s^0| + \mu_d\tau_n$. It does not by itself, however, provide good constraint on the absolute magnitudes of τ_n, $\boldsymbol{\tau}_s^0$, μ_s, and μ_d. *Peyrat et al.* found that Landers ground motion can be equally well fit by either an asperity model, with heterogeneous initial stress, or a barrier model, with heterogeneous friction. So, for the purposes of dynamic rupture simulation, there is leeway in how the dynamics can be configured. TeraShake2 used an asperity model with the dominant heterogeneity in the initial shear traction. Coefficients of friction were constant at $\mu_s = 1$ and $\mu_d = 0$. The slip-weakening distance was constant at $d_0 = 1$ m, aside from a near-surface modification, discussed below. In selecting parameters, the authors noted a delicate balance between cases where rupture did not proceed at all, and cases where the rupture proceeded at super-shear velocity. In order to create a model with sustained sub-shear rupture velocity, they found it necessary to introduce small along-strike variation of the normal stress (and therefore the friction), in the form of an along-strike increase of normal stress in the direction of rupture.

For this study, we use a modified version of one of the NW propagating TeraShake2 scenarios with the specific version number TeraShake2.2. Our model uses coefficients of friction $\mu_s = 1.1$ and $\mu_d = 0.5$, initial normal traction $\tau_n^0 = -20MPa$, and slip-weakening distance $d_0 = 0.5$. Unlike TeraShake2.2, these parameters specify a non-zero dynamic friction level. This prevents reverse and oscillatory slip, and in that sense may be a better approximation of real fault behavior, though both models neglect the strong velocity dependence that is indicated by experimental evidence

(e.g., *Tsutsumi and Shimamoto*, 1997; *Beeler et al.*, 2007) and thermal constraints on friction (*Rice*, 2006). For the initial shear traction model (Fig. 4.4), we take the TeraShake2.2 distribution, τ_s', and apply a scale factor, an offset, and a 10% linear taper,

$$\tau_s = (0.6455\tau_s' + 10)(1.05 - 0.0005r) \ , \tag{4.3}$$

where r is the horizontal distance (in km) along the fault from the SE end. Configured as such, our models produce sustained sub-shear rupture, similar to TeraShake2.2, but with a reduced magnitude of $M_w = 7.6$.

A problem with transplanting the Landers inversion onto the SAF for rupture dynamic simulations is the discrepancy in velocity models at the near surface. The 1D velocity model used by *Peyrat et al.* for the inversion has a minimum S-wave velocity of 1.98 km/s at the surface, while the minimum velocity for the rupture models is 500 m/s. To avoid unrealistically large slip and rupture velocities near the surface, *Olsen et al.* made a number of adjustments to the dynamics parameters. The initial shear traction was tapered to zero between 2 km and 1 km depth, and set to zero over the 0–1 km depth range. Additionally, in the San Bernardino valley only, initial normal traction was reduced, and dynamic slip-weakening friction was replaced with constant friction by setting d_0 to a very large number. This results in the fault being highly dissipative near the surface. In this study, we have used the same reduction of near surface shear traction, although after the rescaling, it is no longer zero at the surface, but about 10 MPa. We have not retained the normal traction and slip-weakening modifications. We instead opt for a simplified model, with constant values over the fault. This may result in unrealistic rupture near the surface at some locations. However, it involves a relatively small percentage of the fault surface, and the effect on far-field ground motions is presumably minor.

The hypocenter is located at 5 km depth, 9 km from the SE end of the fault. Rup-

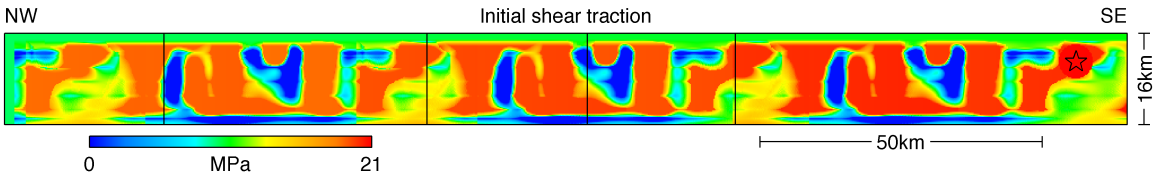

Figure 4.4: Initial shear traction on the fault surface based on dynamic inversion of strong motion records from the M_w7.3 1992 Landers earthquake. To scale the Landers event up to the required fault length, the distribution is repeated multiple times laterally. Initial normal traction is constant over the fault at -20 MPa.

ture is nucleated by lowering the coefficient of friction to it's dynamic level (μ_d) over an expanding circular patch. The radius of the patch expands at 2300 m/s (roughly the Rayleigh wave speed) until spontaneous rupture is able proceed unassisted, which occurs within about 3 km of the hypocenter. Table 4.2 provides a summary of wave propagation and source model parameters.

4.4 Grid Generation

The average resolution for the hexahedral mesh is 200 m requiring 1.8×10^9 grid points to mesh the entire volume. The coordinate system is the UTM zone 11 projection, with the origin translated to 120°W 34°30′N, and the x and y axes rotated 40° clockwise from UTM easting and northing. The mesh has a logically rectangular structure in which nodes and cells are referenced by their logical indices j, k, and l. Grid lines of varying l (i.e., constant j, k lines) are exactly vertical, so that lateral element faces are planar and vertical. We create two versions of the mesh that differ only in their z coordinate: one with a flat ground surface, and one conformed to a digital elevation model. The two meshes have the same horizontal coordinates x and y, so that they appear identical in map view (Fig. 4.5). Terrestrial elevations are resampled from the Global Land One-km Base Elevation data set assembled by the

Table 4.2: Model parameters.

	Model size	$600 \times 300 \times 80\,\mathrm{km}$
	Simulation time	$180\,\mathrm{s}$
	Elements	$3000 \times 1500 \times 400$
	Time steps	15000
Δx	Node spacing	$\approx 200\,\mathrm{m}$
Δt	Time step	$0.012\,\mathrm{s}$
V_p	P-wave velocity	min: $1500\,\mathrm{m/s}$ max: $8298\,\mathrm{m/s}$
V_s	S-wave velocity	min: $500\,\mathrm{m/s}$ max: $4849\,\mathrm{m/s}$
γ	Viscosity	$400/V_s$
τ_s^0	Initial shear traction	mean: $13.4\,\mathrm{MPa}$ max: $20.9\,\mathrm{MPa}$
τ_n^0	Initial normal traction	-20 MPa
μ_s	Coefficient of static friction	1.1
μ_d	Coefficient of dynamic friction	0.5
d_0	Slip weakening displacement	$0.5\,\mathrm{m}$

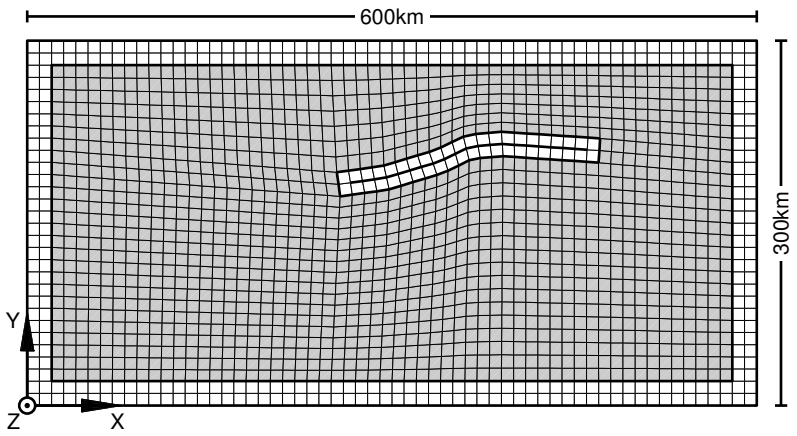

Figure 4.5: Map view, low resolution representation of the hexahedral mesh. Along the boundaries, within the PML zones, grid lines are orthogonal to the boundary. In elements surrounding the fault, grid lines are orthogonal to the fault surface. Elsewhere, within the elements shaded gray, grid line are linearly interpolated.

GLOBE Task Team (1999), and sea floor elevations are resampled from the ETOPO2 data set. Both GLOBE and ETOPO2 are provided by the US Department of Commerce, National Geophysical Data Center. To simplify application of PML absorbing boundaries, the bottom and side boundaries are made planar and orthogonal to the Cartesian directions, and the intersecting grid lines are orthogonal to the boundaries. Special emphasis is given to ensuring the mesh is well behaved in the vicinity of the fault surface. A double layer of elements encasing the $200 \times 16\,\mathrm{km}$ slipping portion of the fault is giving the following properties: element faces intersecting the fault are orthogonal to the fault surface (at fault kinks the element faces bisect the kink angle); the length of all k and l grid line segments, as well as the horizontal width of all fault surface elements is exactly 200 m; and each fault surface element is a parallelogram (square in the absence of topography) of area exactly equal to $40000\,\mathrm{m}^2$. All remaining elements throughout the volume are linearly interpolated between the fault, PML, and ground surface elements.

4.5 Rupture Solutions

Three separate simulation were preformed and given the names 3F, 4F, and 4T. The numeric part of the name indicates the version of the SCEC-CVM used, and the letter indicates whether surface topography was included (T) or not (F). Fig. 4.6 shows the geometry of the fault plane, and the S-wave velocity for the three models. Models 3F and 4T were computed on the DataStar machine at the San Diego Supercomputer Center (SDSC) using 1920 processors. The runs took 13 hours each, with a computation rate of 370 Gflops/s. Model 4F was computed on the SDSC IA-64 Linux cluster, using 480 processors, and ran for 18 hours. It was halted prematurely due to technical problems, completing 150 s of simulation time, out of the planned 180 s.

Due to the identical initial tractions among the models, the rupture solutions are similar at long wavelengths. This is evident in the strong likeness of the final slip distributions (Fig. 4.7). Shorter wavelength differences are more apparent in the peak slip rates (Fig. 4.8), rupture velocities (Fig. 4.9), and initial rupture times (Fig. 4.10). Many of differences can be understood through the following examination of the rupture process.

Fig. 4.11, a space-time image of slip-rate, shows that the rupture is pulse-like, in the sense that slip duration at a point is short compared with overall rupture duration. Pulse-like behavior can result from a friction law in which the fault restrengthens behind the rupture front (e.g., due to strong velocity dependence, as in *Beeler and Tullis*, 1996; *Zheng and Rice*, 1998; *Nielsen and Carlson*, 2000), or when slip duration is controlled by secondary scale lengths such as the seismogenic depth and/or asperity dimensions (e.g., *Day*, 1982; *Beroza and Mikumo*, 1996; *Day et al.*, 1998). Only the latter mechanism operates in our simulations.

The pulse-like rupture takes a circuitous path across the fault surface, following patches of high initial traction (asperities). Patches of low initial shear traction (anti-

asperities) generally lag behind, rupturing after the main front has passed. At some locations, delay of rupture by anti-asperities leads to concavities and focusing of the rupture front into the anti-asperities. V-shaped focusing, visible in the contours of initial rupture time (Fig. 4.10), leads to the interesting result that the highest peak slip velocities at depth (Fig. 4.8) are not located in highly stressed asperities, but in anti-asperities.

In some cases, rupture completely encircles an anti-asperity and converges to a point at its center, as described by *Das and Kostrov* (1983). *Dunham et al.* (2003) recognized this as a mechanism for generating super-shear rupture velocity. We see a prominent example of this at the NW end of the fault, that is present in models 3F and 4T, but absent in model 4F. Rupture time contours in Fig. 4.10 highlight the location of this effect in 4T, and its absence in 4F. The result is a large disparity in the rupture velocities (Fig. 4.9) within a number of the asperities located in the NW half of the fault.

From the space-time slip-rate image (Fig. 4.11) it is clear that the overall rupture velocity is less than the dominant Rayleigh velocity, V_R. A historgram of initial rupture time velocity (Fig. 4.12) shows a maximum value at about $0.85V_R$, a secondary maximum at about $1.2V_S$, and a minimum around V_S. This reflects that the rupture is predominantly mode II. Steady mode II ruptures are capable of propagation at velocities above V_S, but not in the interval between V_R and V_S. The distribution of rupture velocities sharply declines above $\sqrt{2}V_S$, the velocity at which S-wave radiation vanishes for mode II rupture (*Eshelby*, 1949).

4.6 Cohesive Zone Resolution

For numerical solutions of slip-weakening rupture models, it is important to adequately resolve the cohesive zone, that is, the portion of the fault behind the rupture

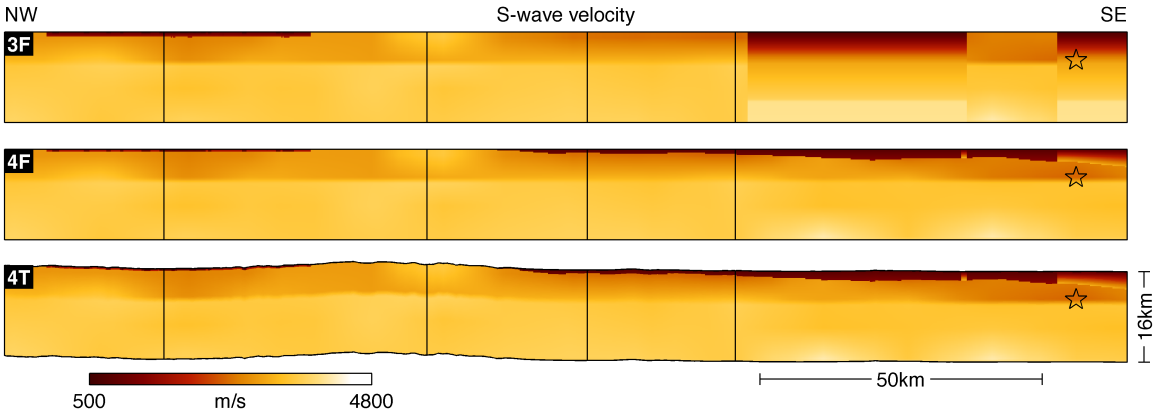

Figure 4.6: Comparison of S-wave velocity on the fault surface for models 3F, 4F and 4T. Vertical lines mark changes in strike between planar segments. The star marks the nucleation point at 5 km depth. SCEC-CVM version 3.0 is used for model 3F, and version 4.0 is used for models 4F and 4T. Topography is flattened in models 3F and 4F, while true topography is used for model 4T.

Table 4.3: Model statistics.

		3F	4F	4T
M_0	Moment (EN-m)	269.5	267.8	266.8
M_w	Moment magnitude	7.587	7.585	7.584
$\langle \Delta\tau_s \rangle$	Mean stress drop (MPa)	3.86	3.74	3.77
$\langle s \rangle$	Mean slip (m)	3.03	2.79	2.78
s_{max}	Maximum slip (m)	15.21	10.60	11.64
$\langle \dot{s}_{peak} \rangle$	Mean peak slip rate (m/s)	3.21	2.86	2.84

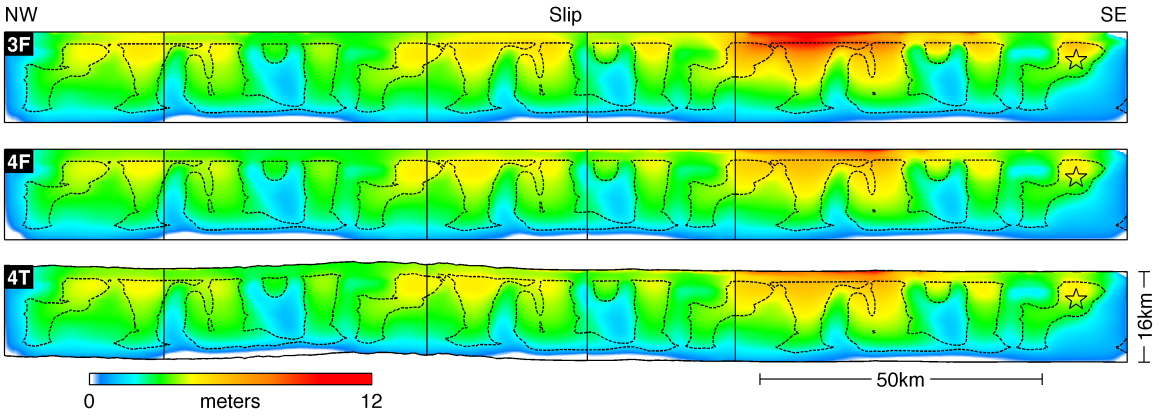

Figure 4.7: Comparison of final slip for models 3F, 4F, and 4T. High slip is smoothly correlated to low density basin material at the surface, and to high initial traction at depth. Areas of high initial traction (asperities) are demarcated by dashed contours at 18 MPa.

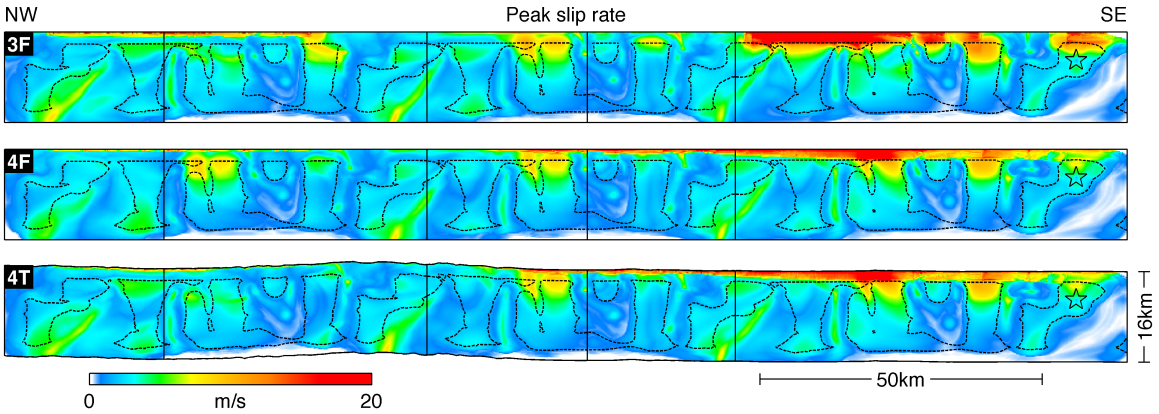

Figure 4.8: Comparison of peak slip rate for models 3F, 4F, and 4T. Highest slip rates at the surface occur in low density basin material. Due to rupture front focusing, highest slip rates at depth occur in narrow bands, located in areas of low initial shear traction (anti-asperities).

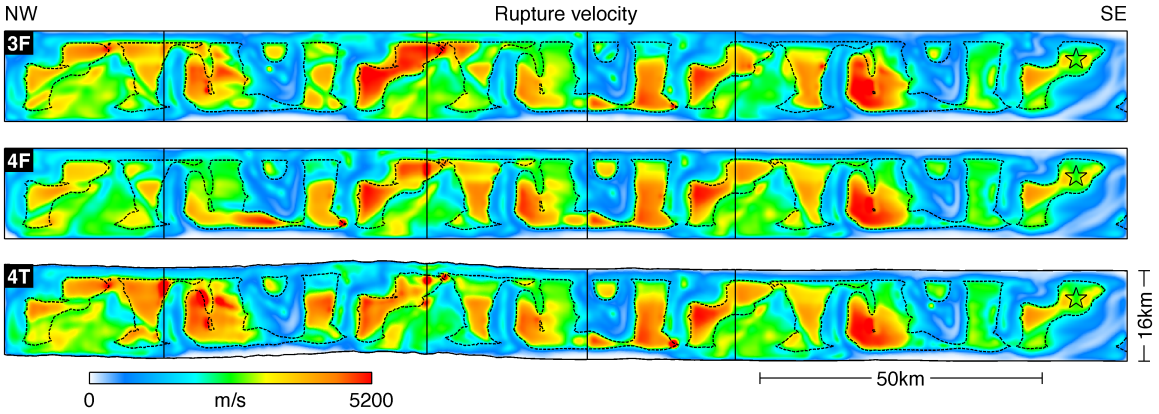

Figure 4.9: Comparison of spatially smoothed initial rupture velocity for models 3F, 4F, and 4T. Largest values are generally confined to asperities, with high variability among the models at the NW end.

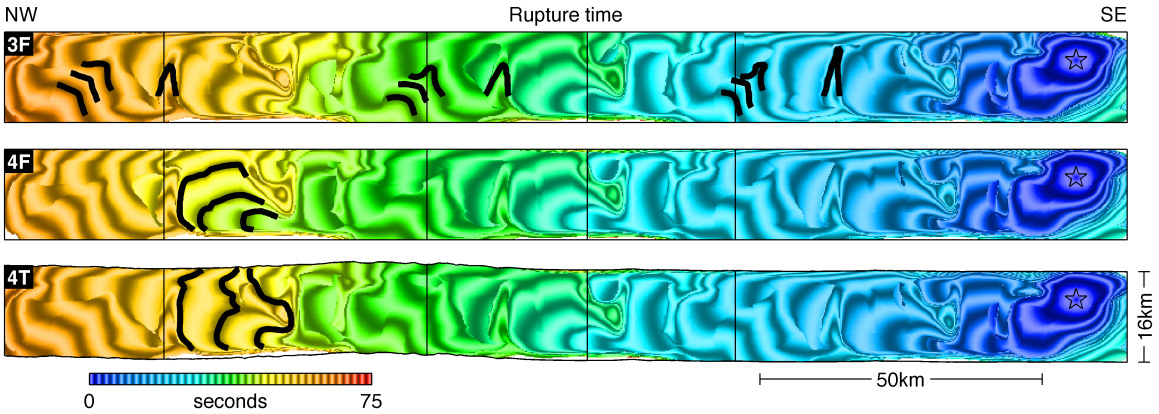

Figure 4.10: Comparison of initial rupture time (defined as the time when slip velocity first exceeds 1 cm/s) for models 3F, 4F, and 4T. Light and dark fringes contour rupture fronts. Heavy contours in 3F highlight V-shaped focusing of rupture that produces high slip-rate bands seen in Fig. 4.8. Heavy contours in 4T highlight rupture focusing around an anti-asperity that leads to super-shear rupture velocity. Similar focusing does not occur at the same location in 4F, where instead rupture takes a single path around the anti-asperity, and propagates upward at sub-shear velocity.

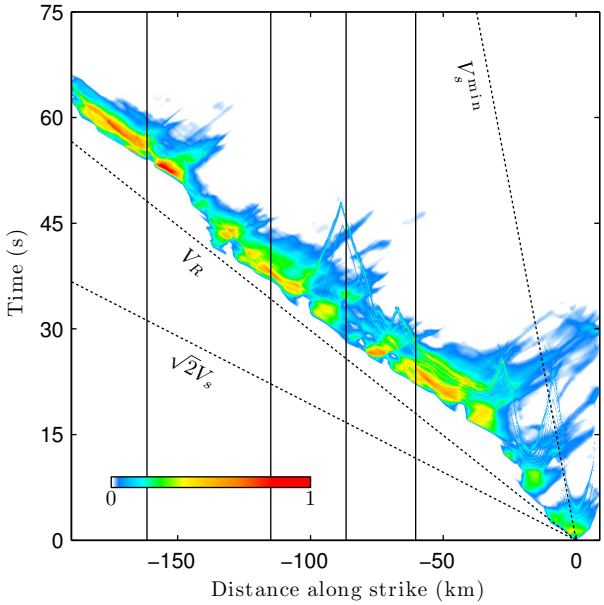

Figure 4.11: Space-time plot of depth averaged slip rate for model 4T, with the peak value normalized to one. In addition to the main NW rupture pulse, secondary back-propagating ruptures, and slow surface ruptures are visible as well. The overall rupture velocity is less than the dominant Rayleigh velocity (V_R), and local rupture velocity is bounded by the minimum S-wave velocity ($V_s^{\min}$) and $\sqrt{2}V_s$.

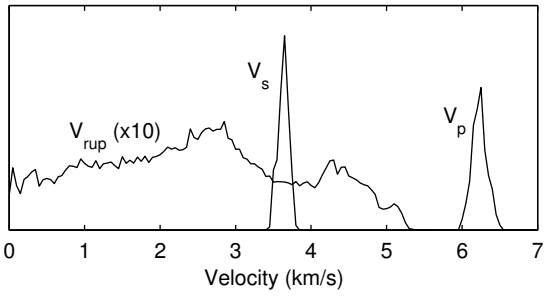

Figure 4.12: Histogram of rupture velocity, S-wave velocity, and P-wave velocity on the fault surface for model 4T. The sample is limited to areas where V_s and V_p are close to their dominant values, thus excluding the near surface. Rupture velocity is spatially smoothed prior to computing the histogram, and the histogram values are magnified by a factor of 10 relative to those for V_s and V_p.

tip that is actively weakening and has not yet reached the dynamic friction level. For a static, initially uniformly stressed, semi-infinite, mode II crack, *Palmer and Rice* (1973) and *Rice* (1980) estimated the cohesive zone width to be

$$\Lambda_{\mathrm{II}}^0 = \frac{9\pi}{32} \frac{d_0 \mu}{(1-\nu)(\mu_d - \mu_s)\tau_n^0} \ , \tag{4.4}$$

and for a mode III crack, they estimated the width to be

$$\Lambda_{\mathrm{III}}^0 = \frac{9\pi}{32} \frac{d_0 \mu}{(\mu_d - \mu_s)\tau_n^0} \ . \tag{4.5}$$

For the SCEC-CVM 4.0 models, the Λ_{II}^0 estimate ranges from 38 m at some surface locations to 2490 m at depth, with a mean of 1600 m. Λ_{III}^0 ranges from 20 to 1915 m, with a mean of 1200 m. With a spatial resolution of 200 m, the cohesive zone is likely to be poorly resolved within the low velocity basins. This has the effect of artificially increasing d_0, and increasing the fracture energy dissipated at the fault. Fortunately, higher d_0 may be physically appropriate for the near surface. As discussed previously, TeraShake2.2 specified an essentially infinite slip-weakening distance for the San Bernardino valley.

Equations (4.4) and (4.5) apply to a static crack, and provide an upper bound for a crack tip propagating with non-zero rupture velocity. For a propagating rupture, *Andrews* (1976, 2004) estimates the cohesive zone width to be approximately

$$\Lambda = \frac{1}{2} \left(\frac{d_0 \mu}{\Delta\tau} \right)^2 \frac{1}{L} \ , \tag{4.6}$$

where L is the propagation distance. It is based on a number of simplifying assumptions, such as a semi-infinite, 2D crack geometry. We wish to test whether the Λ estimate is useful for the complicated, heterogeneous models of the study. If we treat

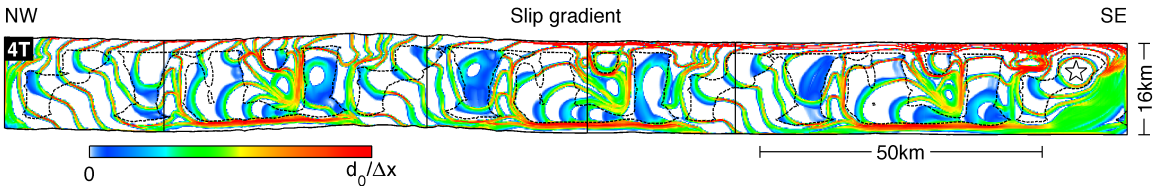

Figure 4.13: Magnitude of slip gradient inside the breakdown zone at 1.2 s intervals for model 4T. Plotted is the peak gradient over the time intervals, normalized by $d_0/\Delta x$ (the slip-weakening distance divided by the cell size). The cohesive zone is well resolved except in the basins, where breakdown widths approach Δx, and slip gradients approach $d_0/\Delta x$.

asperities as sub-faults of approximate with 8 km and stress drop of 9 MPa, from (4.6) we get an estimate of about 260 m for Λ. That would mean the cohesive zone is resolved by only 2 or 3 points if the estimate is accurate. However, this estimate based on local asperity dimension and stress drop appears to be conservative, and direct measurement of the cohesive zone from the slip (Fig. 4.13), finds it is generally around 2 km and sometimes wider in the asperities. We can also see that the cohesive zone shrinks to as little as 800 km or so at locations of rupture front focusing in anti-asperities. These widths are wide enough to be adequately resolve by several grid points. But, as expected, the cohesive zone is poorly resolve in low velocity sediments, usually spanning only a single 200 m element.

4.7 Ground Motion

We now consider velocity time histories for selected sites at the free surface. From here onward, where comparisons are made to TeraShake2.2 results, the latter are scaled by a factor of 0.674, the ratio of moment release between model 3F and TeraShake2.2. This is equivalent to scaling the TerShake2.2 shear and normal prestress values and D_c parameter by the same factor of 0.674. We will use the abbreviation TS as shorthand for the scaled TeraShake2.2 model. At low frequency (below

0.1 Hz), the strongest velocities are generally confined to a pulse containing between one and three cycles of oscillation, and lasting 30 to 60 seconds. Model 3F agrees well with TS (Fig. 4.14). Differences due to the velocity model are minor between models 3F and 4F (Fig. 4.15), and the effects of topography in model 4T compared to model 4F are even smaller (Fig. 4.16).

At higher frequency ($0.1 < f \leq 0.25$ Hz), basin reverberations last much longer than 60 s at some sites, and there are greater differences in ground motion among the models (Figs 4.17, 4.18, and 4.19). Variability in the source ruptures hinders our ability to distinguish between source and path effects as the cause of the differences. The ambiguity can be illustrated by the Lancaster site located 75 km from the end of the rupture in the forward directivity direction. Peak peak ground velocity at Lancaster is 50% greater in model 4F than in model 4T. A possible source based explanation is that the deamplification in model 4T is caused by decrease forward directivity due to the prevalence of super-shear rupture velocities at the NW end of the fault. A path based explanation may be that surface waves are disrupted by the topography of the San Bernardino Mountains, an effect described by *Ma et al.* (2007).

In the case of the wave-guide amplification at the LA basin site of Montebello, a strong dependence on the velocity model can be seen. For sites lying on the shallow basin between the SAF and the LA basin (San Bernardino, Riverside, and Ontario), ground velocity time histories are similar for models 3F and 4F, suggesting that wave motion entering the LA basin is comparable for the two models. By the time waves reach Montebello, though, they have 50% greater peak amplitude in 3F, due to strong energy arriving later in the record. The LA basin sites of Santa Ana and Long Beach show similar amplification of model 3F relative to model 4F.

For hypothetical earthquake scenarios such as these, one of the few comparisons to real data that we can make is with empirically determined attenuation relations.

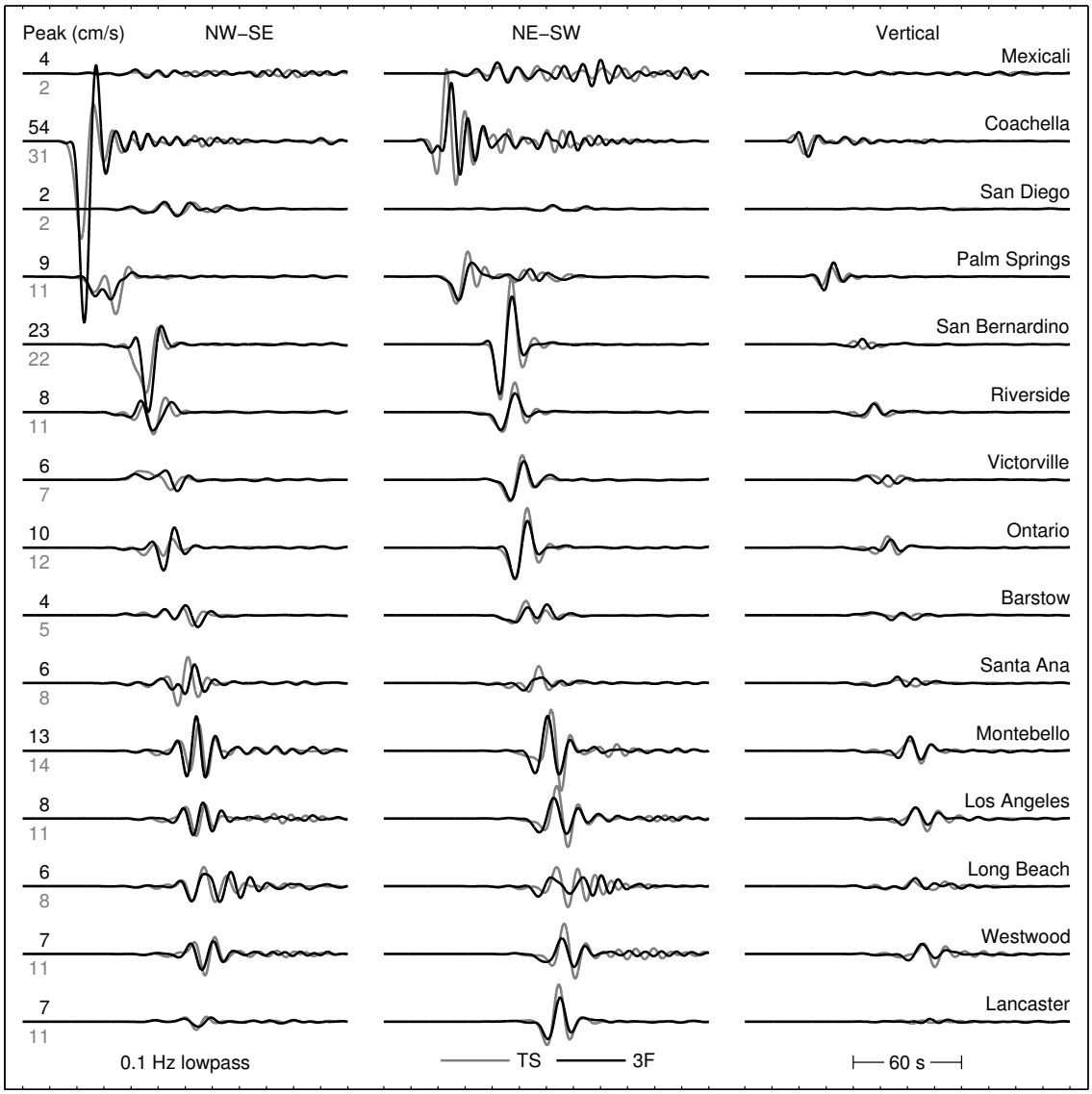

Figure 4.14: Zero to 0.1 Hz ground velocity for TeraShake2.2 (TS) and model 3F. The TS curves are scaled down to match the moment release of model 3F. Receiver locations are shown in Figures 4.1 and4.2.

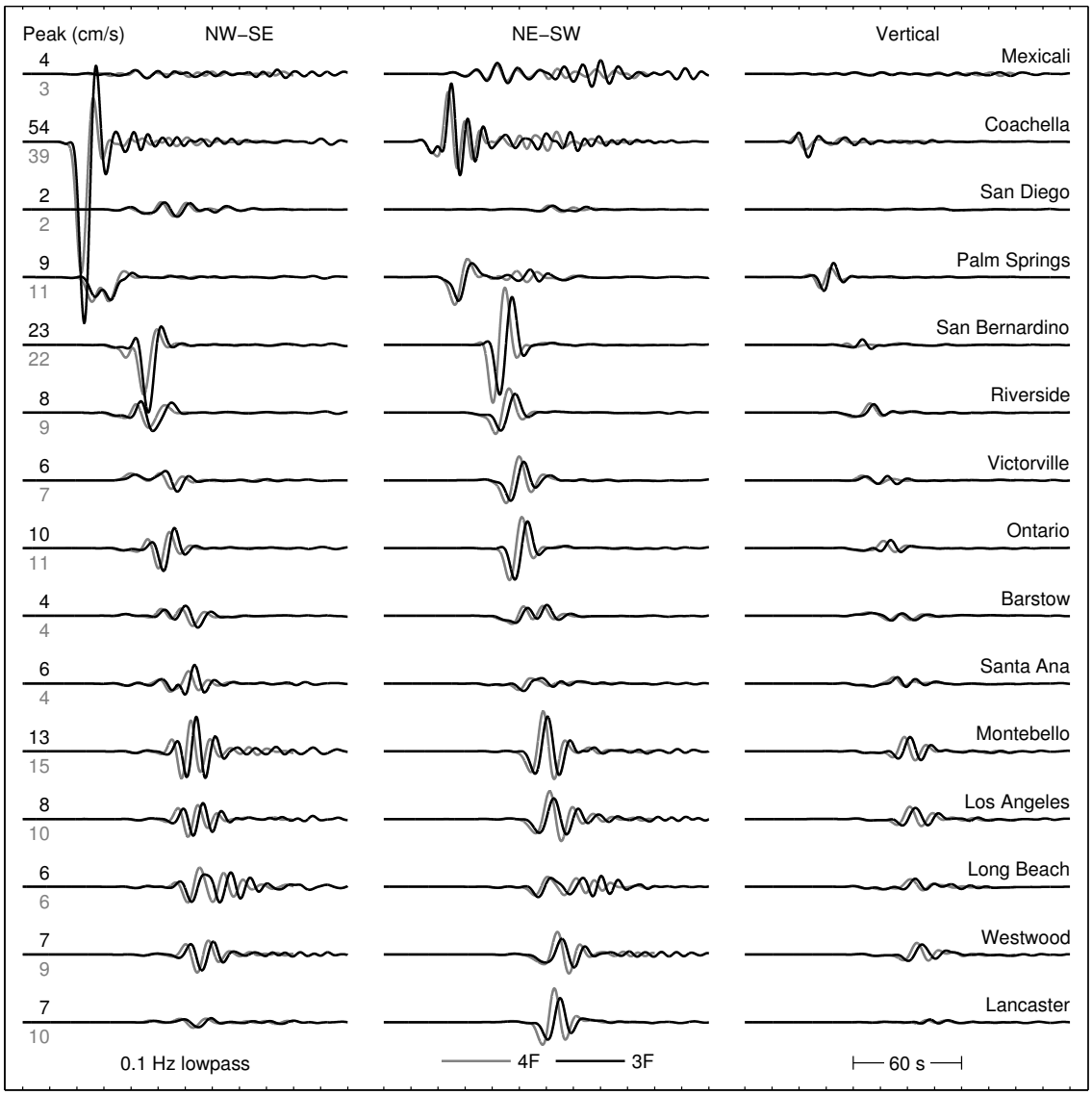

Figure 4.15: Zero to 0.1 Hz ground velocity for models 4F and 3F.

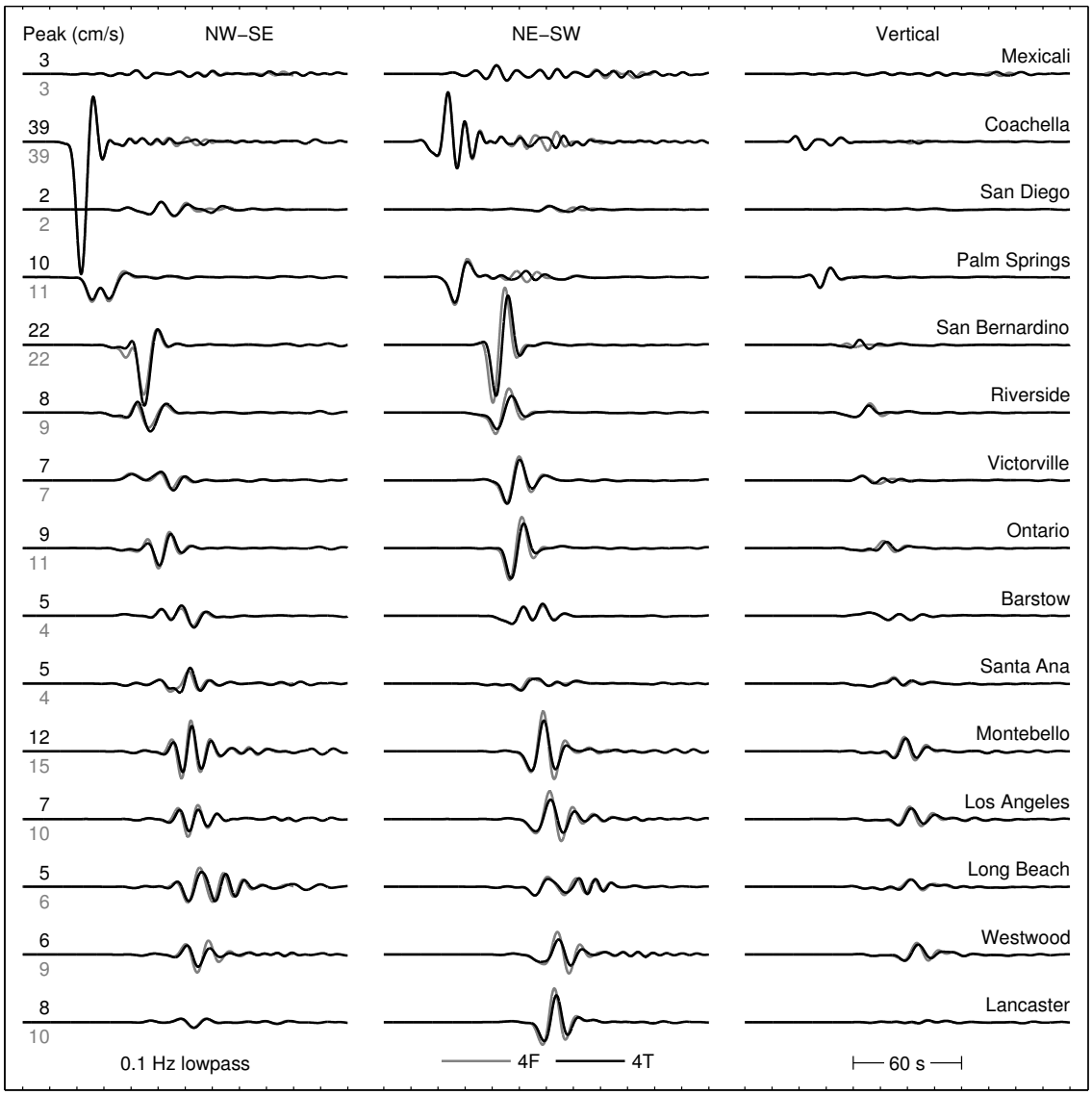

Figure 4.16: Zero to 0.1 Hz ground velocity for models 4F and 4T.

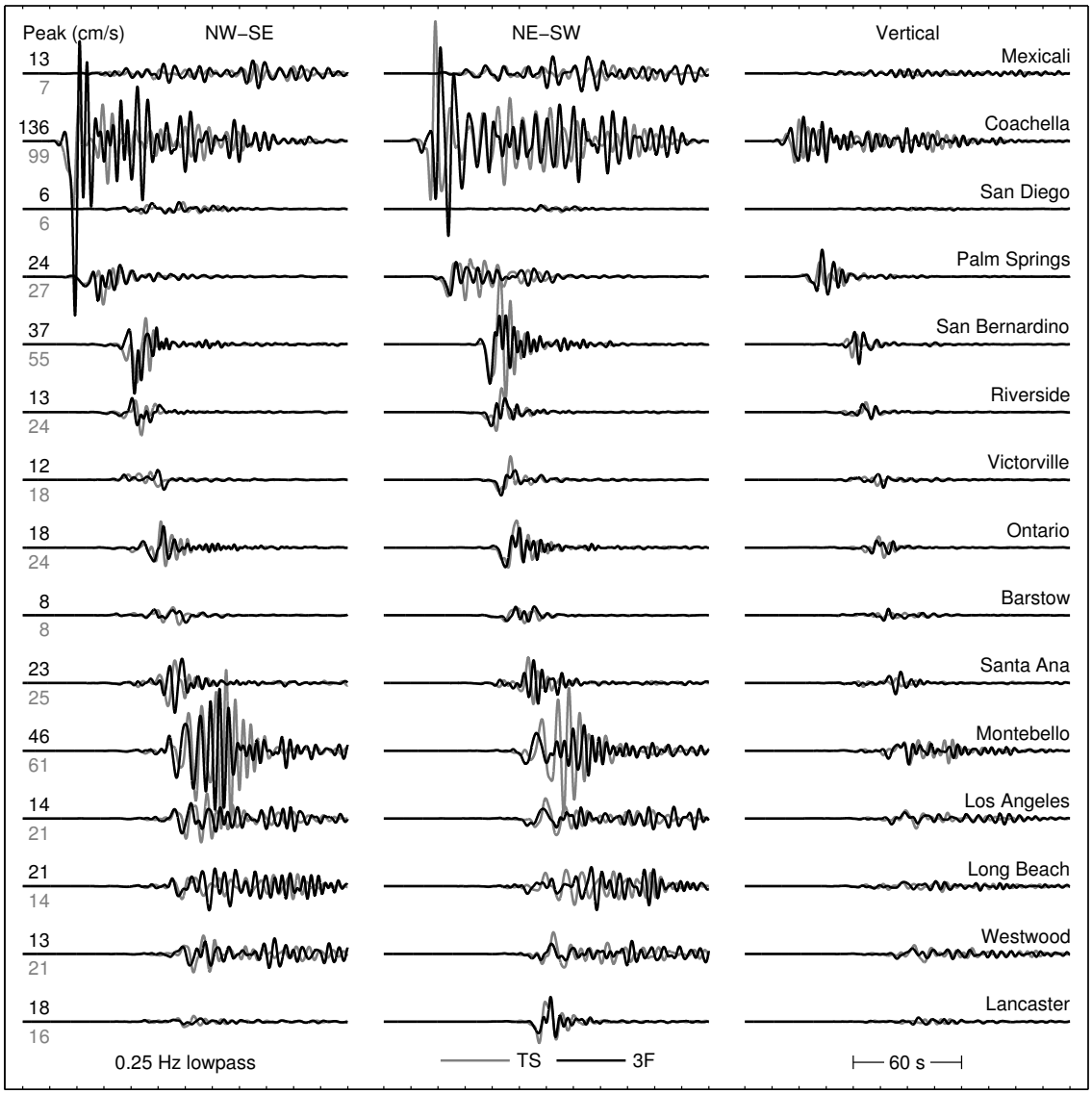

Figure 4.17: Zero to 0.25 Hz ground velocity for TeraShake2.2 (TS) and model 3F. The TS curves are scaled down to match the moment release of model 3F.

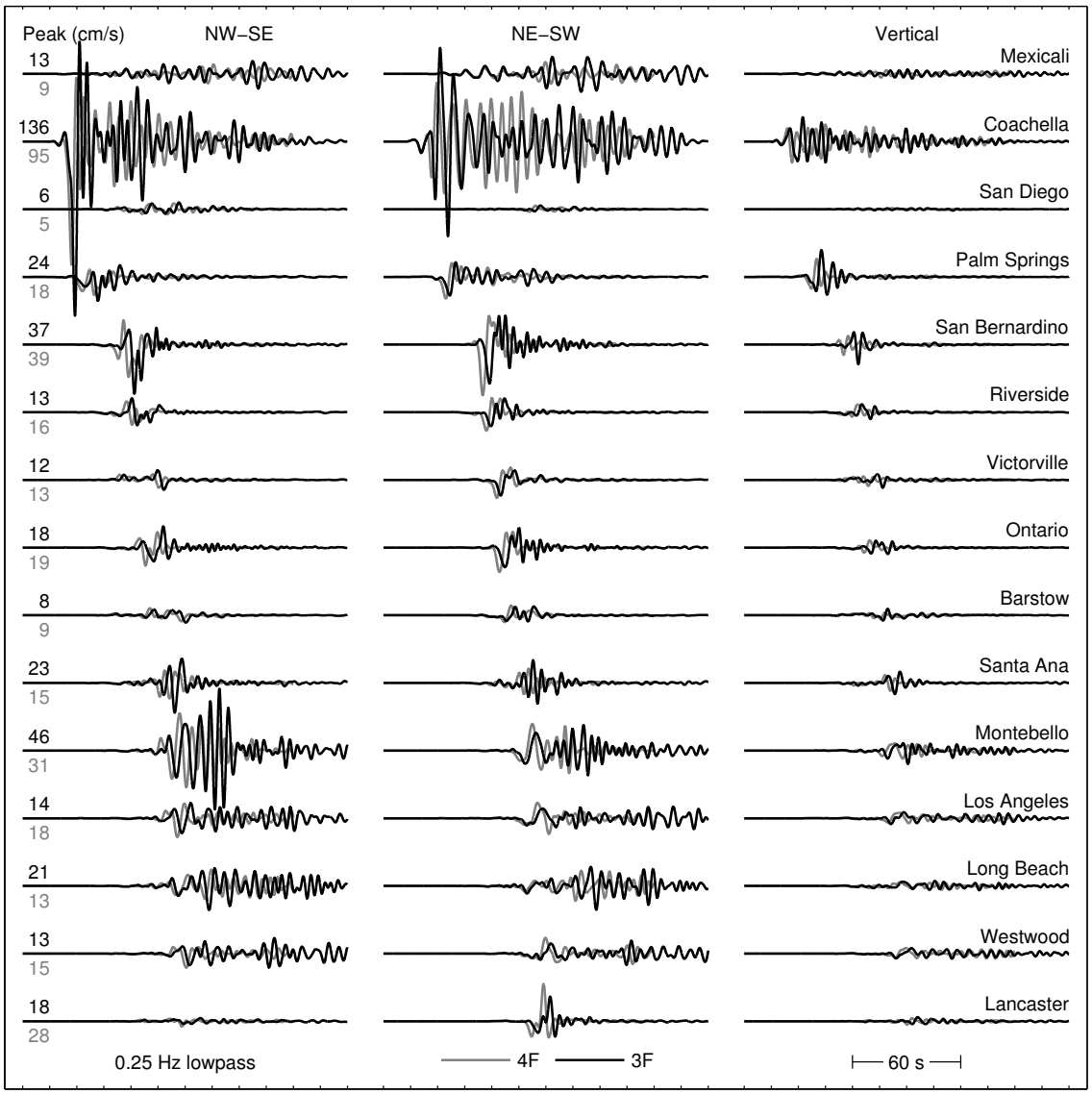

Figure 4.18: Zero to 0.25 Hz ground velocity for models 4F and 3F.

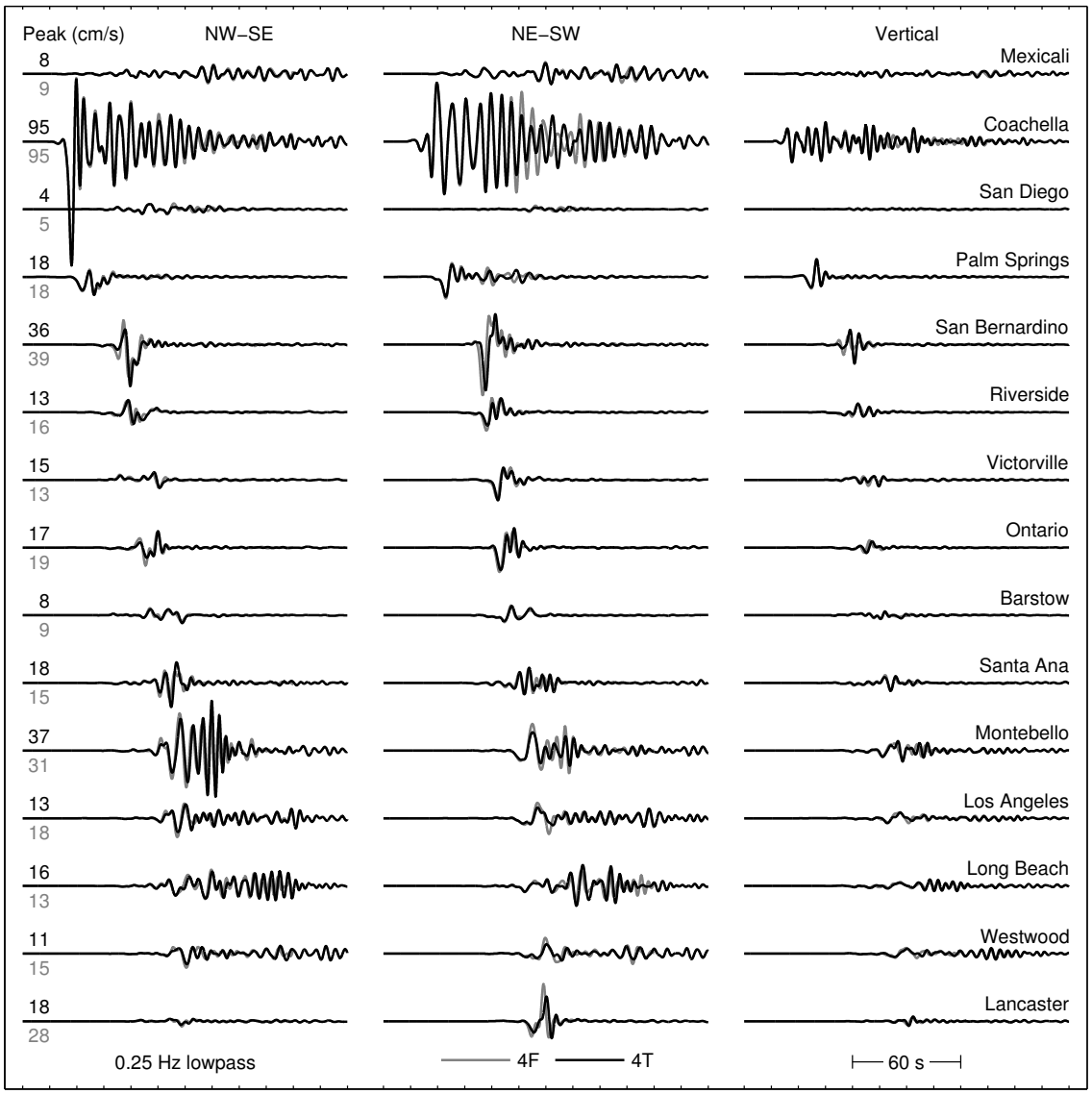

Figure 4.19: Zero to 0.25 Hz ground velocity for models 4F and 4T.

Based on statistical analysis of earthquake catalogs, attenuation relations predict ground motion for generic earthquakes based on parameters such as moment magnitude, fault/receiver distance, basin depth, and style of faulting. For the following comparison, we use the 'next generation' attenuation relation of *Campbell and Bozorgnia* (2007), abbreviated as CB-NGA.

Tables 4.4 and 4.5 list 21 sites, the locations of which are shown on Fig. 4.2. The site specific CB-NGA parameters for this study are: R_{RUP}, the closest distance to the coseismic rupture surface; $Z_{2.5}$, the basin depth defined by the shallowest depth to S-wave velocity greater than 2.5 km/s; and V_{S30}, the average S-wave velocity of the upper 30 m. The CB-NGA does not include a parameter for directivity or three-dimensional path effects. For each site we give the median peak ground velocity (PGV) predicted by the CB-NGA, and the simulated PGV from models 4F and 4T. The simulated PGV is computed by the geometric mean of the maxima of the two horizontal velocity components. The simulated PGV are also given as a probability of exceedance (POE) determined by CB-NGA median and standard deviation. Additionally, PGV values are presented graphically in Figs 4.20 and 4.21.

We group the sites into rock sites, shallow basin sites, and deep basin sites. The near surface S-wave velocity (V_{S30}) is extracted from the SCEC-CVM (and is often less than the minimum S-wave velocity used in the computations, 500 m/s). Outside of the basins, surface layers are not well resolved by the SCEC-CVM, resulting in unrealistically high velocities at the rock sites. So we impose an upper limit of 760 m/s for V_{S30}. The rocks sites are useful to illustrate directivity, unobscured by basin effects. They are listed roughly in SE to NW order, beginning with Yuma, where PGV is much below the CB-NGA prediction at close to 100% POE, and ending with Santa Barbara, where PGV is much greater than the CB-NGA prediction, ranging from 7% to 32% POE. In between POE decreases towards the NW, in the forward

directivity direction. The absence of this clear rupture directivity effect in the CB-NGA ground motion predictions is because the CB-NGA does not consider directivity in its site parameterization.

Shallow basin sites generally fall at or below the expected PGV from CB-NGA (greater than 50% POE). We speculate that the simulation bandwidth is not able to entirely capture the dominant shallow basin reverberation frequencies, so the PGV are under-estimated. This is not a problem for deep basin sites where dominant wavelengths are longer and frequencies lower. Deep basin PGV is most of the time at or above the CB-NGA expected values, and more so for the SCEC-CVM version 3.0 models (TS and 3F). The simulated PGV is exceptionally high at Montebello, though not as high in our models as in TS: the PGV for TS is a factor of four greater than the median CB-NGA at that site, whereas for our models PGV is only a factor of two above median CB-NGA.

4.8 Conclusion

We have simulated a M_w7.6, NW propagating dynamic rupture on the southern San Andreas fault with non-planar fault geometry and surface topography. Numerous cases of rupture front focusing (due to heterogeneous initial stress conditions and complex rupture propagation) lead to high peak slip velocities in relatively weakly stressed anti-asperities. Peak slip displacements, on the other hand, are confined to the highly stressed asperities. This suggests a mechanism by which high-frequency components of the slip function are at least partially disjointed from low-frequency components. A further effect of the rupture heterogeneity is that, for our simulations, the cohesive zone is generally narrower in the anti-asperities than in asperities, contrary to the rough a priori estimates derived from steady state, semi-infinite rupture.

We compared simulations with different versions of the SCEC-CVM, and simula-

Table 4.4: Peak ground velocity (geometric mean horizontal component) for TeraShake2.2 (TS) and model 3F compared to the *Campbell and Bozorgnia* (2007) NGA ground motion relation (CB). The TS values are scaled down to M_w7.6 for the comparison.

	R_{RUP}	$Z_{2.5}$	V_{S30}	PGV (cm/s)			POE	
Rock sites	(km)	(km)	(m/s)	CB	TS	3F	TS	3F
Yuma	123.0	0.0	760	4.9	0.9	1.0	>99%	>99%
Ensenada	184.2	0.0	760	3.6	2.1	2.2	85%	84%
San Diego	144.6	0.0	760	4.4	3.5	3.7	66%	62%
Oceanside	102.9	0.0	760	5.6	3.4	4.2	82%	70%
Palm Springs	11.7	0.0	760	26.0	18.9	15.6	73%	83%
Victorville	33.3	0.0	760	12.6	10.0	9.2	67%	72%
Barstow	80.4	0.0	760	6.7	6.4	6.0	53%	58%
Lancaster	74.0	0.0	760	7.1	8.2	6.6	39%	55%
Bakersfield	183.7	0.0	760	3.7	3.8	4.5	47%	34%
Santa Barbara	202.8	0.0	760	3.4	7.5	4.3	7%	32%
Shallow basin sites								
San Bernardino	6.9	1.0	281	63.0	37.8	32.3	85%	91%
Riverside	26.5	0.8	395	23.7	17.4	10.4	72%	94%
Ontario	28.7	1.2	395	22.9	19.6	15.3	61%	78%
Deep basin sites								
Mexicali	80.4	3.9	739	8.9	6.2	12.0	75%	28%
Coachella	3.8	3.9	739	62.1	66.3	94.9	45%	21%
Montebello	64.0	3.5	409	14.1	52.6	29.4	1%	8%
Santa Ana	69.2	2.6	274	14.7	17.9	19.2	35%	30%
Long Beach	86.0	2.9	364	10.9	11.5	17.7	46%	17%
Los Angeles	73.5	2.8	384	11.8	16.5	9.8	26%	64%
Westwood	88.2	3.3	386	11.0	14.8	10.5	29%	53%
Oxnard	154.9	3.2	302	8.2	13.4	11.0	17%	29%

Notes:
R_{RUP} is the closest distance to the coseismic rupture surface.
$Z_{2.5}$ is the depth to the 2.5 km/s shear velocity horizon (basin depth).
V_{S30} is the average shear velocity for the upper 30 m.
POE is the CB probability of exceedance for the simulated PGV.

Table 4.5: Peak ground velocity (geometric mean horizontal component) for models 4F and 4T compared to the *Campbell and Bozorgnia* (2007) NGA ground motion relation (CB)

	R_{RUP}	$Z_{2.5}$	V_{S30}	PGV (cm/s)			POE	
Rock sites	(km)	(km)	(m/s)	CB	4F	4T	4F	4T
Yuma	123.0	0.0	760	4.9	1.1	1.2	>99%	>99%
Ensenada	184.2	0.0	760	3.6	1.7	1.5	93%	95%
San Diego	144.6	0.0	760	4.4	3.4	2.6	68%	84%
Oceanside	102.9	0.0	760	5.6	4.2	4.0	70%	73%
Victorville	33.3	0.0	760	12.6	8.7	9.5	76%	70%
Barstow	80.4	0.0	760	6.7	6.2	6.3	56%	54%
Lancaster	74.0	0.0	760	7.1	10.2	7.0	24%	51%
Bakersfield	183.7	0.0	760	3.7	4.7	4.7	31%	32%
Santa Barbara	202.8	0.0	760	3.4	6.2	5.3	13%	20%
Shallow basin sites								
Palm Springs	11.7	0.2	760	26.6	14.6	14.0	87%	89%
San Bernardino	6.9	0.5	281	60.6	29.9	32.3	92%	90%
Riverside	26.5	0.4	395	22.9	11.2	9.7	91%	95%
Ontario	28.7	0.5	395	21.8	15.5	14.2	74%	79%
Deep basin sites								
Mexicali	80.4	2.7	760	7.3	7.8	7.0	45%	53%
Coachella	3.8	2.8	760	50.9	62.9	63.1	34%	34%
Montebello	64.0	3.4	409	13.6	23.3	22.3	15%	17%
Santa Ana	69.2	2.4	274	14.7	11.0	14.2	71%	53%
Long Beach	86.0	2.8	364	10.9	11.6	12.9	45%	37%
Los Angeles	73.5	2.7	384	11.8	12.8	9.1	44%	69%
Westwood	88.2	3.1	386	10.6	11.1	7.4	47%	75%
Oxnard	154.9	3.0	302	7.9	13.0	11.2	17%	25%

Notes:
R_{RUP} is the closest distance to the coseismic rupture surface.
$Z_{2.5}$ is the depth to the 2.5 km/s shear velocity horizon (basin depth).
V_{S30} is the average shear velocity for the upper 30 m.
POE is the CB probability of exceedance for the simulated PGV.

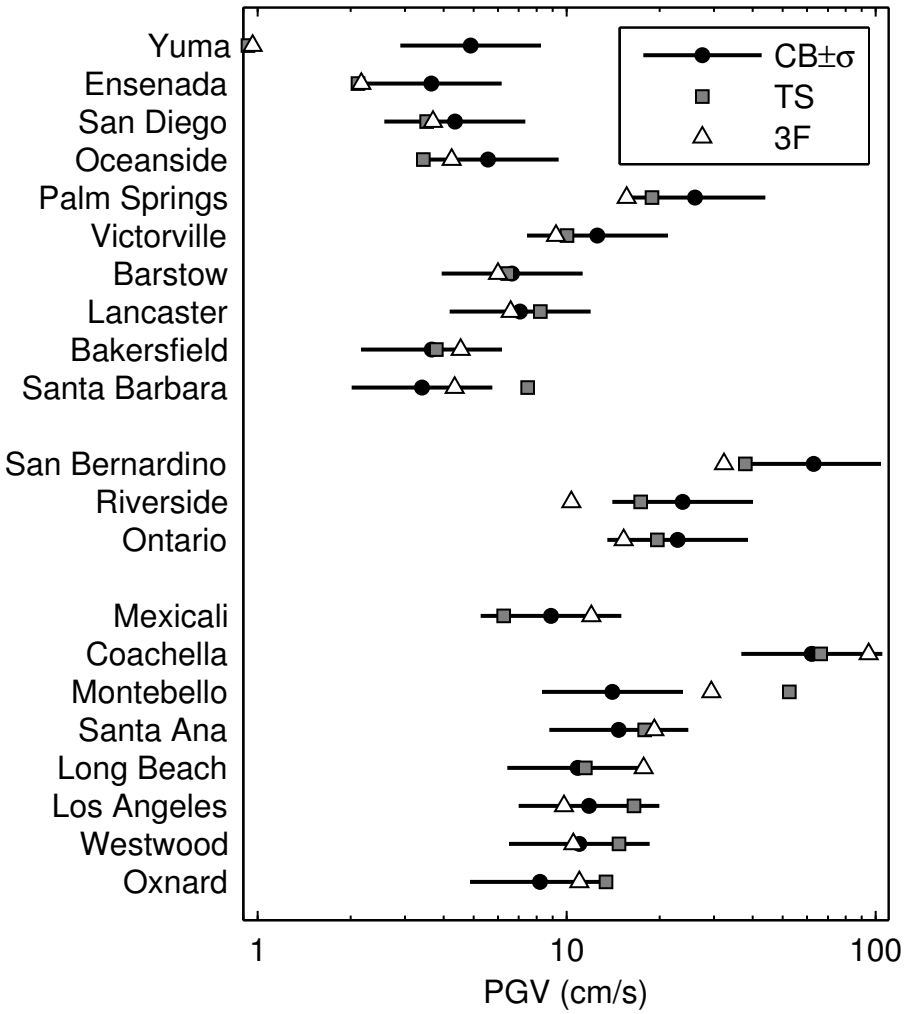

Figure 4.20: Plot of peak ground velocity data from Table 4.4 comparing scaled TeraShake2.2 and model 3F to the *Campbell and Bozorgnia* (2007) NGA ground motion relation. Error bars indicate one standard deviation to either side of the CB-NGA median PGV.

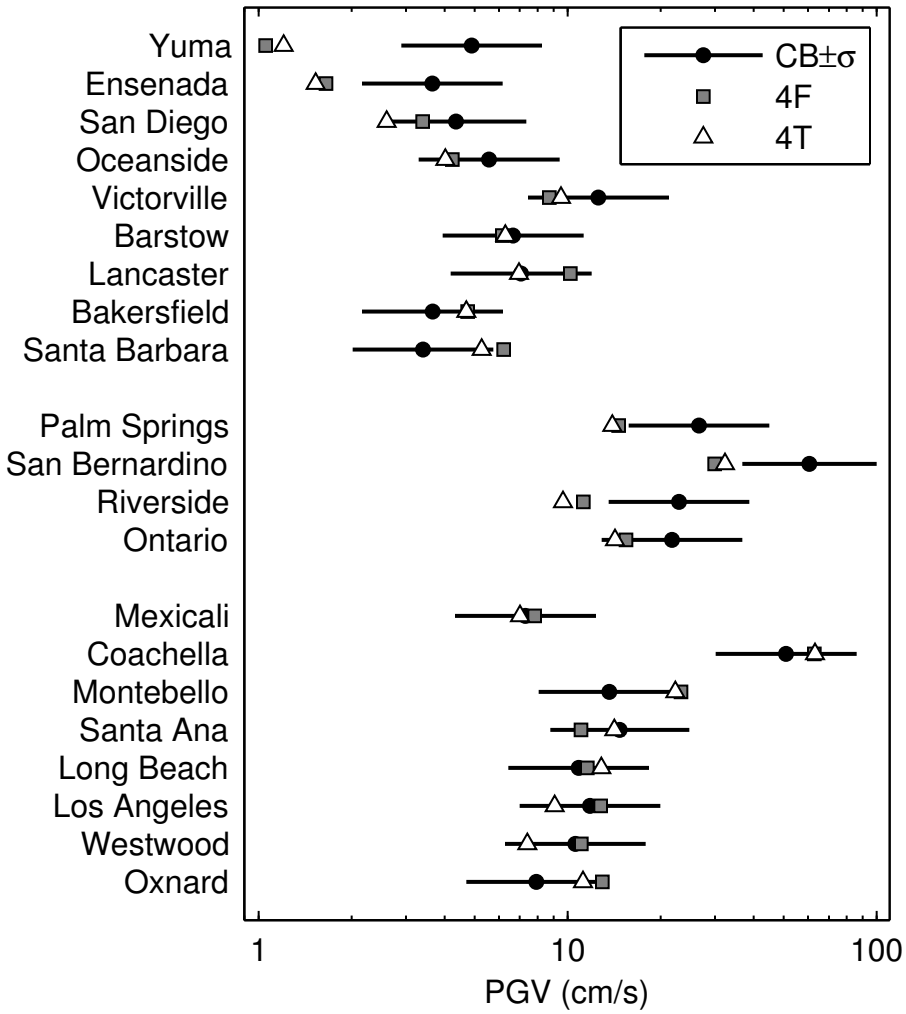

Figure 4.21: Plot of peak ground velocity data from Table 4.5 comparing models 4F and 4T to the *Campbell and Bozorgnia* (2007) NGA ground motion relation. Error bars indicate one standard deviation to either side of the CB-NGA median PGV.

tions with and without topography at the free surface, and find that either change is enough to significantly alter the rupture. At low frequency, the results match the TeraShake2.2 simulation by *Olsen et al.* (2008), though our model predicts less pronounced wave guide amplification in the LA basin. We found that the wave guide effect is smaller still when SCEC-CVM version 4.0 is used, compared to version 3.0. Peak ground velocities for most sites fall within one standard deviation of the *Campbell and Bozorgnia* (2007) empirical attenuation relation. However, rupture directivity and basin wave guide effects cause more significant deviation from the attenuation relation at some sites.

Acknowledgments

Kim Olsen provide much assistance to the project and provided his TeraShake stress model and results for comparison. This work was supported by the National Science Foundation under grants ATM-0325033 and EAR-0122464, by the San Diego Supercomputer Center, and by the Southern California Earthquake Center. SCEC is funded by NSF Cooperative Agreement EAR-0106924 and USGS Cooperative Agreement 02HQAG0008. The SCEC contribution number for this paper is 1147. This chapter, in full, is under review by the Bulletin of the Seismological Society of America. The dissertation author is the primary investigator and author of this paper, with Steven Day and Jean-Bernard Minster as co-authors.

References

Andrews, D. J. (1976), Rupture propagation with finite stress in antiplane strain, *J. Geophys. Res.*, *81*(B20), 3575–3582.

Andrews, D. J. (2004), Rupture models with dynamically determined breakdown displacement, *Bull. Seism. Soc. Am.*, *94*(3), 769–775, doi:10.1785/0120030142.

Beeler, N. M., and T. E. Tullis (1996), Self-healing slip pulses in dynamic rupture models due to velocity-dependent strength, *Bull. Seism. Soc. Am.*, *86*(4), 1130–1148.

Beeler, N. M., T. E. Tullis, and D. Goldsby (2007), Constitutive relationships and physical basis of fault strength due to flash-heating, *J. Geophys. Res.*, *113*(B01401), doi:10.1029/2007JB004988.

Berenger, J.-P. (1994), A perfectly matched layer for the absorption of electromagnetic waves, *J. Comput. Phys.*, *114*(2), 185–200, doi:10.1006/jcph.1994.1159.

Berenger, J.-P. (1996), Three-dimensional perfectly matched layer for the absorption of electromagnetic waves, *J. Comput. Phys.*, *127*(2), 363–379, doi:doi:10.1006/jcph.1996.0181.

Beroza, G. C., and T. Mikumo (1996), Short slip duration in dynamic rupture in the presence of heterogeneous fault properties, *J. Geophys. Res.*, *101*(B10), 22,449–22,460, doi:10.1029/96JB02291.

Campbell, K. W., and Y. Bozorgnia (2007), Campbell-Bozorgnia NGA ground motion relations for the geometric mean horizontal component of peak and spectral ground motion parameters, *Tech. Rep. PEER 2007/02*, Pacific Earthquake Engineering Research Center.

Das, S., and B. V. Kostrov (1983), Breaking of a single asperity: rupture process and seismic radiation, *J. Geophys. Res.*, *88*(B5), 4277–4288.

Day, S. M. (1982), Three-dimensional finite difference simulation of fault dynamics: Rectangular faults with fixed rupture velocity, *Bull. Seism. Soc. Am.*, *72*(3), 705–727.

Day, S. M. (1998), Efficient simulation of constant Q using coarse-grained memory variables, *Bull. Seism. Soc. Am.*, *88*(4), 1051–1062.

Day, S. M., and C. R. Bradley (2001), Memory-efficient simulation of anelastic wave propagation, *Bull. Seism. Soc. Am.*, *91*(3), 520–531, doi:10.1785/0120000103.

Day, S. M., G. Yu, and D. J. Wald (1998), Dynamic stress changes during earthquake rupture, *Bull. Seism. Soc. Am.*, *88*(2), 512–522.

Day, S. M., L. A. Dalguer, N. Lapusta, and Y. Liu (2005), Comparison of finite difference and boundary integral solutions to three-dimensional spontaneous rupture, *J. Geophys. Res.*, *110*(B12307), doi:10.1029/2005JB003813.

Dunham, E. M., P. Favreau, and J. M. Carlson (2003), A supershear transition mechanism for cracks, *Science*, *299*(5612), 1557–1559, doi:10.1126/science.1080650.

Ely, G. P., S. M. Day, and J.-B. Minster (2008), A support-operator method for visco-elastic wave modeling in 3d heterogeneous media, *Geophys. J. Int.*, *172*(1), 331–344, doi:10.1111/j.1365-246X.2007.03633.x.

Eshelby, J. D. (1949), Uniformly moving dislocations, *Proc. Phys. Soc. A*, *62*(5), 307–314, doi:10.1088/0370-1298/62/5/307.

Frankel, A. D., et al. (2002), Documentation for the 2002 update of the national seismic hazard maps, *Open-File Report 2002-420*, USGS, Denver, CO.

GLOBE Task Team (1999), The global one-kilometer base elevation (GLOBE) elevation model, version 1.0, *Tech. rep.*, Boulder, Colorado.

Kohler, M. D., H. Magistrale, and R. W. Clayton (2003), Mantle heterogeneities and the SCEC reference three-dimensional seismic velocity model version 3, *Bull. Seism. Soc. Am.*, *93*(2), 757–774, doi:10.1785/0120020017.

Ma, S., R. J. Archuleta, and M. T. Page (2007), Effects of large-scale surface topography on ground motions, as demonstrated by a study of the San Gabriel mountains, Los Angeles, California, *Bull. Seism. Soc. Am.*, *97*(6), 2066–2079, doi: 10.1785/0120070040.

Magistrale, H. (2005), Version 4 of the CVM, 2005 SCEC Annual Meeting, Palm Springs, CA.

Magistrale, H., S. M. Day, R. W. Clayton, and R. W. Graves (2000), The SCEC southern California reference three-dimensional seismic velocity model version 2, *Bull. Seism. Soc. Am.*, *90*(6B), S65–76, doi:10.1785/0120000510.

Marcinkovich, C., and K. Olsen (2003), On the implementation of perfectly matched layers in a three-dimensional fourth-order velocity-stress finite difference scheme, *J. Geophys. Res.*, *108*(B5), 2276, doi:10.1029/2002JB002235.

Nielsen, S. B., and J. M. Carlson (2000), Rupture pulse characterization: Self-healing, self-similar, expanding solutions in a continuum model of fault dynamics, *Bull. Seism. Soc. Am.*, *90*(6), 1480–1497, doi:10.1785/0120000021.

Oglesby, D. D., D. S. Dreger, R. A. Harris, N. Ratchkovski, and R. Hansen (2004), Inverse kinematic and forward dynamic models of the 2002 Denali fault earthquake, Alaska, *Bull. Seism. Soc. Am.*, *94*(6B), S214–233, doi:10.1785/0120040620.

Olsen, K. B., S. M. Day, J.-B. Minster, Y. Cui, A. Chourasia, M. Faerman, R. Moore, P. Maechling, and T. Jordan (2006), Strong shaking in Los Angeles expected from southern San Andreas earthquake, *Geophys. Res. Lett.*, *33*(L07305), doi:10.1029/2005GL025472.

Olsen, K. B., S. M. Day, J.-B. Minster, Y. Cui, A. Chourasia, D. Okaya, P. Maechling, and T. Jordan (2008), TeraShake2: spontaneous rupture simulations of M_w7.7 earthquakes on the southern San Andreas fault, *Bull. Seism. Soc. Am.*, in press.

Palmer, A. C., and J. R. Rice (1973), The growth of slip surfaces in the progressive failure of over-consolidated clay, *Proc. R. Soc. A*, *332*(1591), 527–548, doi:10.1098/rspa.1973.0041.

Peyrat, S., K. B. Olsen, and R. Madariaga (2001), Dynamic modeling of the 1992 Landers earthquake, *J. Geophys. Res.*, *106*(B11), 26,467, doi:10.1029/2001JB000205.

Rice, J. R. (1980), The mechanics of earthquake rupture, in *Physics of the Earth's Interior*, *Proceedings of the Enrico Fermi International School of Physics*, vol. Course 78, edited by A. M. Dziewonski and E. Boschi, pp. 555–649, North-Holland.

Rice, J. R. (2006), Heating and weakening of faults during earthquake slip, *J. Geophys. Res.*, *111*(B05311), doi:10.1029/2005JB004006.

Seeber, L., and J. G. Armbruster (1995), The San Andreas fault system through the Transverse Ranges as illuminated by earthquakes, *J. Geophys. Res.*, *100*(B5), 8285–8310, doi:10.1029/94JB02939.

Tsutsumi, A., and T. Shimamoto (1997), High-velocity frictional properties of gabbro, *Geophys. Res. Lett.*, *24*(6), 699–702.

Virieux, J. (1986), P-SV wave propagation in heterogeneous media: Velocity-stress finite-difference method, *Geophysics*, *51*(4), 889–901, doi:10.1190/1.1442147.

Weldon, R., K. Scharer, T. Fumal, and G. Biasi (2004), Wrightwood and the earthquake cycle: What a long recurrence record tells us about how faults work, *GSA Today*, *14*(9), 4–10, doi:10.1130/1052-5173(2004)014<4:WATECW>2.0.CO;2.

Working Group on California Earthquake Probabilities (1995), Seismic hazards in southern California: Probable earthquakes, 1994 to 2024, *Bull. Seism. Soc. Am.*, *85*(2), 379–439.

Zheng, G., and J. R. Rice (1998), Conditions under which velocity-weakening friction allows a self-healing versus a cracklike mode of rupture, *Bull. Seism. Soc. Am.*, *88*(6), 1466–1483.

Chapter 5

Conclusions

5.1 Summary

For this thesis I have developed a new method for modeling earthquakes using spontaneous shear crack propagation within a heterogeneous, three-dimensional, viscoelastic solid. A few of the important capabilities of the method are: (1) Surfaces and ruptures may be non-planar, removing the commonly used restriction of rectangular geometry; (2) The accuracy of the method may be acceptable even for highly deformed elements, such as those needed for low-angle thrust faults intersecting the free surface; and (3) The numerical algorithm is highly scalable on parallel architectures. The Support Operator Rupture Dynamics code (SORD) provides a tool that is well poised to help address some of the current challenging problems in seismology.

5.2 Verification

The method was verified using a set of test problems focusing on various various aspects of wave propagation and rupture dynamics. The test problems are each established benchmark exercises for which multiple published solutions are available

that used alternative numerical or semi-analytical methods. The layer over half-space problem (LOH.1), with a double-couple point source (*Day and Bradley*, 2001), tested three-dimensional wave propagation in a heterogeneous medium with a planar free-surface boundary condition. The solutions were found to agree with frequency-wavenumber integration for wavelengths of at least 10 times the discretization length. A cylindrical canyon problem tested the case of a non-planar free-surface and non-rectangular elements, using a vertically incident P-wave. Surface amplification agreed closely with boundary integral solutions at wavelengths of at least 20 times the discretization length. Spontaneous rupture propagation was tested using SCEC rupture validation problem number 3 (TPV3), which consists of a rectangular planar fault within a homogeneous medium (*Harris and Archuleta*, 2004; *Harris et al.*, 2008). The results were compared to and agreed closely with boundary integral solutions. The LOH.1 and TPV3 problems were both computed on rectangular meshes as well as meshes deformed by simple shearing. The sheared mesh tests were used to look for any anisotropy in wave or rupture propagation due to non-rectangular elements. For TPV3 the shear angle was varied over a series of models. Grid-induced errors were found to increase with mesh shear angle, with the logarithm of error approximately proportional to angle over the range tested, and accuracy is sufficient for most practical applications even for mesh shear angles appropriate to low-angle thrust faults (i.e., mesh shears up to 70 degrees).

5.3 Applications

Non-planar rupture effects were studied by comparing a model with gradual changes in strike and a model with abrupt changes in strike. TPV3 was modified for two geometries: one with cylindrical curvature, and one with sharp 30° kinks between planar segments. The kinked model developed stress singularities due to the

partial rupture barriers formed by the kinks. The kinks are also a source of wave radiation.

The second, and more prominent application of SORD was a set of M_w7.6 earthquake simulations on the southern San Andreas fault. Low frequency (greater than 10 s period) ground velocity agreed well with the TeraShake2.2 model by *Olsen et al.* (2008). Shorter than 10 s period showed significant differences. We found that rupture solutions are nearly identical, at early times, for different versions of the SCEC Community Velocity Model (*Magistrale et al.*, 2000; *Kohler et al.*, 2003; *Magistrale*, 2005), as well as for models with and without topography included at the free surface. However, the effects are strong enough to cause solutions to diverge significantly at later times. Episodes of rupture focusing (due to heterogeneous initial traction) were identified that led to both super-shear rupture velocity within asperities, as well as zones of high slip velocity between asperities. The second phenomenon is a means by which the locations of peak motions can be frequency dependent, as peak displacements are generally confined within asperities. We also identified a local minimum near the S-wave velocity in the rupture velocity statistics, associated with the forbidden rupture velocity range of mode II rupture lying between the Rayleigh velocity and the S-wave velocity. Modeled peak ground velocities were consistent with those predicted by the empirical attenuation relation of *Campbell and Bozorgnia* (2007), though there was systematic deviations associated with rupture directivity and the specifics of the southern California velocity model (sedimentary basins and wave guides). These type of three-dimensional effects are not accounted for by the empirical model.

5.4 Future Work

Ground motion predictions from simulations will become more useful for engineering practice when estimates of their epistemic uncertainty can be made. One way to

begin to assess that uncertainty is with comparisons using alternative seismic velocity models. This can be done for southern California because of the availability velocity model by *Süss and Shaw* (2003), an alternative to the SCEC-CVM used here. Differences may arise in the basin response of the two velocity models, for example, because the *Süss and Shaw* model more completely represents the off-shore continuation of the Los Angeles basin.

Further investigation is also needed to determine if the basin wave guides effects observed in the SAF models are a common characteristic of potential scenarios on other faults in southern California. The region is dissected by a complex network of many potentially hazardous faults. With comprehensive digital representations of the faults available from the SCEC Community Fault Model (*Plesch et al.*, 2007), work can begin promptly on performing alternate scenario simulations. One difficulty that must first be addressed is the creation of appropriate discretizations of the problem domain. Mesh generation is straightforward for vertical faults like the SAF modeled here. For more complex non-planar and dipping faults, more sophisticated methods are required. Available mesh generation techniques and software will need to be evaluated. One promising method is direct optimization (*Castillo and McGuinness*, 2002), whereby certain measurements of the mesh fitness are constructed, such as grid orthogonality and cell volume uniformity, and then global optimization is performed on a weighted sum of the various fitness measures. Optimization could allow for material velocity to be factored into the fitness measures, and so allowing the optimization to naturally densify the mesh were it is needed, such as in low velocity surface sediments. Mesh densification along the fault surface, for better resolution of the rupture process, could be accomplished in a similar fashion.

The SAF earthquake models focused on relatively low frequencies (up to about 0.25 Hz). Since small to medium sized buildings are most sensitive to frequencies

greater the 0.25 Hz, these models are not yet fully adequate for seismic hazard assessment. They need to be extended to finer discretizations, and this presents a formidable computational challenge. The SORD code has demonstrated very good scalability, and during the time of this study, the largest parallel computers available for general research have progressed from thousands of processors to tens of thousands of processors. The increased parallelism may well necessitate further code improvements and tuning. If this effort is successful, and combined with adaptive mesh refinement, the method can be extended to frequencies approaching 1 Hz for large events such as the SAF models. With the option of incorporating a high frequency stochastic component to the ground motions, we can accomplish truly high bandwidth simulations.

As we move into modeling higher frequencies, accurate treatment of attenuation becomes more important. The Kelvin-Voigt model used here results in a quality factor Q that is inversely proportional to frequency, whereas for earth materials, Q is approximately constant with respect to frequency. Frequency-independent Q can be modeled numerically by incorporating relaxation memory variables (*Day and Minster*, 1984), a technique made more efficient by sparsely sampling the memory variables (*Day*, 1998; *Day and Bradley*, 2001; *Graves and Day*, 2003). This method can be readily incorporated into the support operator scheme.

Another potential contribution to be made with this method is the study of rupture process itself. Because the method works explicitly with stress components (rather than a stiffness matrix, for example), it is easily generalized to calculate stresses from inelastic constitutive models (e.g. Coulomb plasticity, damage rheology, etc.), at the cost of saving the stress tensor components globally. This capability would be important in the study earthquake rupture dynamics, for example, as rupture-induced off-fault nonlinear deformation may be a significant contributor to the energy budget

of earthquakes, and may also influence strong motion amplitudes. It is believed by some that fault stress heterogeneity may be primarily due to non-planarity of fault surfaces. We saw in the kinked fault model of Chapter 3 and in the SAF model that changes in fault direction, as expected, cause stress concentrations. Systematic analysis of fault topography effects to test this hypothesis is an application well suited to our method. We have used a slip-weakening friction law, where the frictional coefficient depends only on the slip path length. However, recent work suggests that strong velocity weakening induced by thermal and other effects occurs during earthquakes. Rice (*Rice*, 2006) reviews the key models, including melting of microscopic frictional contacts, and effective normal stress reduction from thermal pressurization of pore fluids. Incorporating models for these types of processes will be needed if we are to bring earthquake simulation practices into agreement with latest understanding of rupture physics, and our method is readily adaptable to more exotic friction laws.

References

Campbell, K. W., and Y. Bozorgnia (2007), Campbell-Bozorgnia NGA ground motion relations for the geometric mean horizontal component of peak and spectral ground motion parameters, *Tech. Rep. PEER 2007/02*, Pacific Earthquake Engineering Research Center.

Castillo, J. E., and T. McGuinness (2002), Steady state diffusion problems on non-trivial domains: Support operator method integrated with direct optimized grid generation, *Applied Numerical Mathematics*, *40*(1-2), 207–218, doi:10.1016/S0168-9274(01)00069-1.

Day, S. M. (1998), Efficient simulation of constant Q using coarse-grained memory variables, *Bull. Seism. Soc. Am.*, *88*(4), 1051–1062.

Day, S. M., and C. R. Bradley (2001), Memory-efficient simulation of anelastic wave propagation, *Bull. Seism. Soc. Am.*, *91*(3), 520–531, doi:10.1785/0120000103.

Day, S. M., and J.-B. Minster (1984), Numerical simulation of attenuated wavefields

using a Padé approximant method, *Geophys. J. Int.*, *78*(1), 105–118, doi:10.1111/j.1365-246X.1984.tb06474.x.

Graves, R. W., and S. M. Day (2003), Stability and accuracy analysis of coarse-grain viscoelastic simulations, *Bull. Seism. Soc. Am.*, *93*(1), 283–300, doi:10.1785/0120020094.

Harris, R. A., and R. J. Archuleta (2004), Earthquake rupture dynamics: Comparing the numerical simulation methods, *Eos Trans. AGU*, *85*(34), 321, doi:10.1029/2004EO340003.

Harris, R. A., et al. (2008), The SCEC/USGS dynamic earthquake rupture code validation exercise, *Seism. Res. Lett.*, in review.

Kohler, M. D., H. Magistrale, and R. W. Clayton (2003), Mantle heterogeneities and the SCEC reference three-dimensional seismic velocity model version 3, *Bull. Seism. Soc. Am.*, *93*(2), 757–774, doi:10.1785/0120020017.

Magistrale, H. (2005), Version 4 of the CVM, 2005 SCEC Annual Meeting, Palm Springs, CA.

Magistrale, H., S. M. Day, R. W. Clayton, and R. W. Graves (2000), The SCEC southern California reference three-dimensional seismic velocity model version 2, *Bull. Seism. Soc. Am.*, *90*(6B), S65–76, doi:10.1785/0120000510.

Olsen, K. B., S. M. Day, J.-B. Minster, Y. Cui, A. Chourasia, D. Okaya, P. Maechling, and T. Jordan (2008), TeraShake2: spontaneous rupture simulations of M_w7.7 earthquakes on the southern San Andreas fault, *Bull. Seism. Soc. Am.*, in press.

Plesch, A., et al. (2007), Community fault model (CFM) for southern California, *Bull. Seism. Soc. Am.*, *97*(6), 1793–1802, doi:10.1785/0120050211.

Rice, J. R. (2006), Heating and weakening of faults during earthquake slip, *J. Geophys. Res.*, *111*(B05311), doi:10.1029/2005JB004006.

Süss, M. P., and J. H. Shaw (2003), P wave seismic velocity structure derived from sonic logs and industry reflection data in the Los Angeles basin, California, *J. Geophys. Res.*, *108*(B3), 2170, doi:10.1029/2001JB001628.

Chapter 6

SORD code documentation

The Support Operator Rupture Dynamics (SORD) code simulates spontaneous rupture within a 3D isotropic viscoelastic solid. Wave motions are computed on a logically rectangular hexahedral mesh, using the generalized finite difference method of support operators. Stiffness and viscous hourglass corrections are employed to suppress suppress zero-energy grid oscillation modes. The fault surface is modeled by coupled double nodes, where the strength of the coupling is determined by a linear slip-weakening friction law. Model external boundaries may be reflective or absorbing, where absorbing boundaries are handled using the method of perfectly matched layers (PML). SORD is written in Fortran 95 and parallelized for multi-processor execution using Message Passing Interface (MPI).

6.1 Usage

SORD is distributed as a `tar` archive. Installation consists simply of unpacking the archive and entering the `sord/` directory. Configuration, compilation and execution are all handled by the main wrapper script called '`sord`'. The `sord` script takes an input file as its argument. Each time `sord` is executed, a new directory is set up

for that particular run, starting with `run/01`. The default action is to compile and configure the job only. Job launching is deferred. In the directory will be a script called '`run`' to start the job interactively and a script '`que`' for submitting the job to the batch system. The `sord` script accepts the following command line options:

`-i`	start job interactively with the `run` script
`-q`	submit job to batch system with the `que` script
`-n`	check input only and exit
`-g`	compile with debugging and syntax checking flags
`-G`	start job in debugger
`-d`	delete output from previous runs before starting
`-f`	force recompile
`-s`	serial mode, no MPI (default if `np` $== 1$)
`-p`	parallel mode, requires MPI (default if `np` > 1)
`-m opt`	emulate alternative machine configuration, e.g. '`datastar`'
`-v opt`	generate SAF mesh and SCEC-CVM, opt indicates version 3 or 4

6.2 Input and Output

Input is specified in a restricted form of the MATLAB programming language. Large data sets such as the material model are stored separately in floating-point binary files. Annotated example input files are located in the `in/` directory. The input file `defaults.m`, read before any other input, contains a short description of each SORD parameter.

Output is saved in binary format. An associated metadata file `meta.m`, contains a summary of parameters for the run, and a structured description of the binary output. The M-file format facilitates post-processing and visualization with MATLAB. MATLAB utilities for manipulating and visualizing SORD output are included in the

`m/` directory. Using the `read4d` function for accessing SORD binary output correctly accounts for byte order when moving data between big-endian and little-endian architectures. Separate Fortran utilities are also included in the `util/` directory for converting the byte order of binary files, and for converting to and from ASCII text format.

Statistic, such as peak acceleration and peak velocity, are computed periodically during each run and saved in the directory `stats/`. Additionally, internal code timings, for benchmarking performance, are collected and saved to the `prof/` directory. Inspecting these files during a run is a good way to check that it is proceeding correctly. The raw binary files can be examined with the standard UNIX command '`od -f`' or with the included Fortran utilities. The `stats` utility computes the minimum, maximum, and mean values for binary files.

6.3 Code Portability

SORD has been tested the following system configurations:

Operating systems: Linux, IBM AIX, Apple OSX, Sun Solaris

Fortran 95 compilers: GNU, IBM, Intel, Sun, Portland Group

MPI implementations: ANL MPICH, IBM, Myricom MPICH-GM

Porting to a new system may require adjusting the compiler flags that are set in script `sh/config`. Machines with specialized parallel environments may need a custom run script and modification of the main `sord` script under the 'Run scripts' section. See `sh/datastar` and `sh/teragrid` for example custom run scripts.

6.4 LOH.1 Parameters

The following SORD input file was used for the rectangular mesh version of the LOH.1 model presented in Section 2.6.

```
% PEER LOH.1 - Layer over a halfspace, buried double couple source

  np = [ 1 16 1 ];              % number of processors in each dimension
  nn = [ 261 301 161 ];         % number of mesh nodes, nx ny nz
  nt = 2250;                    % number of time steps
  dx = 50.;                     % spatial step size
  dt = 0.004;                   % time step size

% Material properties of the halfspace
  rho = 2700.;                  % density
  vp  = 6000.;                  % P-wave speed
  vs  = 3464.;                  % S-wave speed
  gam = 0.;                     % viscosity
  hourglass = [ 1. 2. ];        % hourglass stiffness and viscosity

% Material properties of the layer
  vp  = { 4000. 'zone'   1 1 1   -1 -1 21 };
  vs  = { 2000. 'zone'   1 1 1   -1 -1 21 };
  rho = { 2600. 'zone'   1 1 1   -1 -1 21 };

% Near side boundary conditions:
% Anti-mirror symmetry at the near x and y boundaries
% Free surface at the near z boundary
  bc1 = [ -2 -2  0 ];

% Far side boundary conditions:
% PML absorbing boundaries at x, y and z boundaries
  bc2 = [ 10 10 10 ];

% Source parameters
  faultnormal = 0;              % disable rupture dynamics
  ihypo = [ 1 1 41 ];           % hypocenter indices
  xhypo = [ 0. 0. 2000. ];      % hypocenter coordinates
  fixhypo = -2;                 % cell registered hypocenter
  tfunc = 'brune';              % Brune pulse time function
  tsource = 0.1;                % dominant period
  moment1 = [ 0. 0. 0. ];       % moment tensor M_xx, M_yy, M_zz
  moment2 = [ 0. 0. 1e18 ];     % moment tensor M_yz, M_zx, M_yz

% Velocity time series output for surface station
  timeseries = { 'v' 6000. 80000. 0. };
```

6.5 TPV3 Parameters

The following SORD input file was used for the rectangular mesh version of the TPV3 model presented in Section 3.4.

```
% TPV3 - SCEC validation problem version 3

  np = [ 1 1 32 ];              % number of processors in each dimension
  nn = [ 351 201 128 ];         % number of mesh nodes, nx ny nz
  nt = 3000;                    % number of time steps
  dx = 50.;                     % spatial step size
  dt = 0.004;                   % time step size

% Near side boundary conditions:
% PML absorbing boundaries for the x, y and z boundaries
  bc1 = [ 10 10 10 ];

% Far side boundary conditions:
% Anti-mirror symmetry for the x and z boundaries
% Mirror symmetry for the y boundary
  bc2 = [ -2  2 -2 ];

% Material properties
  rho = 2670.;                  % density
  vp  = 6000.;                  % P-wave speed
  vs  = 3464.;                  % S-wave speed
  gam = 0.2;                    % viscosity
  gam = { 0.02 'cube' -15001. -7501. -4000.   15001. 7501. 4000. };
  hourglass = [ 1. 2. ];

% Fault parameters
  faultnormal = 3;              % fault plane of constant z
  ihypo = [ -2 -2 -2 ];         % hypocenter indices
  fixhypo = -2;                 % hypocenter is cell centered
  vrup = -1.;                   % disable circular nucleation
  dc  = 0.4;                    % slip weakening distance
  mud = 0.525;                  % coefficient of dynamic friction
  mus = 10000.;                 % coefficient of static friction
  mus = { 0.677  'cube' -15001. -7501. -1.  15001. 7501. 1. };
  tn  = -120e6;                 % normal traction
  ts1 = 70e6;                   % shear traction
  ts1 = { 81.6e6 'cube'  -1501. -1501. -1.   1501. 1501. 1. };

% Fault plane output
  out = { 'x'    1   1 1 -2  0   -1 -1 -2  0 }; % mesh coordinates
  out = { 'su'   1   1 1  0 -1   -1 -1  0 -1 }; % final slip
  out = { 'psv'  1   1 1  0 -1   -1 -1  0 -1 }; % peak slip velocity
```

```
  out = { 'trup' 1   1 1  0 -1   -1 -1  0 -1 }; % rupture time

% Time series output, mode II point
  timeseries = { 'su' -7499. -1. 0. }; % slip
  timeseries = { 'sv' -7499. -1. 0. }; % slip velocity
  timeseries = { 'ts' -7499. -1. 0. }; % shear traction

% Time series output, mode III point
  timeseries = { 'su' -1. -5999. 0. }; % slip
  timeseries = { 'sv' -1. -5999. 0. }; % slip velocity
  timeseries = { 'ts' -1. -5999. 0. }; % shear traction
```

6.6 San Andreas Fault Parameters

The following SORD input file was used for the San Andreas Fault model 4T presented in Chaper 4.

```
% San Andreas Fault, northward dynamic rupture, topography, SCEC-CVM4

  np = [ 1 80 24 ] % 1920 total processors on DataStar
  nn = [ 3001 1502 401 ];       % number of mesh nodes nx ny nz
  nt = 15000;                   % number of time steps
  dt = 0.012;                   % time step length

% Read mesh coordinates from disk.  Horizontal components x1
% and x2 are depth independent, so are stored as 2D planes.
% Vertical coordinate x3 is stored as a full 3D volume.
  datadir = 'saf/scecvm4/0200';
  x1 = { 'read' 'zone' 1 1 1 -1 -1 1 };
  x2 = { 'read' 'zone' 1 1 1 -1 -1 1 };
  x3 = 'read';

% Boundary conditions, PML on all side except for free surface
  bc1 = [ 10 10 10 ];
  bc2 = [ 10 10  0 ];

% Material model
  rho = 'read';                 % read 3D density file
  vp  = 'read';                 % read 3D V_p file
  vs  = 'read';                 % read 3D V_s file
  vdamp = 400.;                 % set viscosity = vdamp / vs
  vp1  = 1500.;                 % set minimum V_p
  vs1  = 500.;                  % set minimum V_s
  gam2 = 0.8;                   % set maximum viscosity
  hourglass = [ 1. 1. ];        % hourglass stiffness and viscosity
```

```
% Fault parameters
  ihypo = [ 2266 997 -26 ];     % hypocenter indices
  faultnormal = 2;              % fault plane at k = ihypo(2) = 997
  slipvector = [ 1. 0. 0. ];    % vector for resolving pre-traction
  tn  = -20e6;                  % initial normal traction
  ts1 = 'read';                 % read initial shear traction file
  dc  = 0.5;                    % slip weakening distance
  mud = 0.5;                    % coefficient of dynamic friction
  mus = 1000.;                  % coefficient of static friction
  mus = [ 1.10 'zone'   1317 0 -81   2311 0 -1 ];

% Nucleation
  fixhypo = 1;                  % node registered hypocenter
  vrup = 2300.;                 % nucleation rupture velocity
  trelax = 0.12;                % time
  rcrit = 3000.;                % radius of nucleation patch

% Fault plane output
  out = { 'su'   1   1317 0 -81 -1   2311 0 -1 -1 }; % final slip
  out = { 'psv'  1   1317 0 -81 -1   2311 0 -1 -1 }; % peak slip velocity
  out = { 'trup' 1   1317 0 -81 -1   2311 0 -1 -1 }; % rupture time

% Velocity time series output
  out = { 'v' 1   2642  813  -1  0   2642  813 -1 -1 }; % Mexicali
  out = { 'v' 1   2028  979  -1  0   2028  979 -1 -1 }; % Coachella
  out = { 'v' 1   2015  324  -1  0   2015  324 -1 -1 }; % San Diego
  out = { 'v' 1   1842  940  -1  0   1842  940 -1 -1 }; % Palm Springs
  out = { 'v' 1   1457  960  -1  0   1457  960 -1 -1 }; % San Bernardino
  out = { 'v' 1   1476  852  -1  0   1476  852 -1 -1 }; % Riverside
  out = { 'v' 1   1307 1141  -1  0   1307 1141 -1 -1 }; % Victorville
  out = { 'v' 1   1345  840  -1  0   1345  840 -1 -1 }; % Ontario
  out = { 'v' 1   1278 1341  -1  0   1278 1341 -1 -1 }; % Barstow
  out = { 'v' 1   1384  620  -1  0   1384  620 -1 -1 }; % Santa Ana
  out = { 'v' 1   1205  668  -1  0   1205  668 -1 -1 }; % Montebello
  out = { 'v' 1   1142  642  -1  0   1142  642 -1 -1 }; % Los Angeles
  out = { 'v' 1   1262  532  -1  0   1262  532 -1 -1 }; % Long Beach
  out = { 'v' 1   1079  589  -1  0   1079  589 -1 -1 }; % Westwood
  out = { 'v' 1    951  961  -1  0    951  961 -1 -1 }; % Lancaster
```